Spectral CT Thermometry for Thermal Liver Ablation

Applicability and Needle Artifact Reduction

Lennart Koetzier

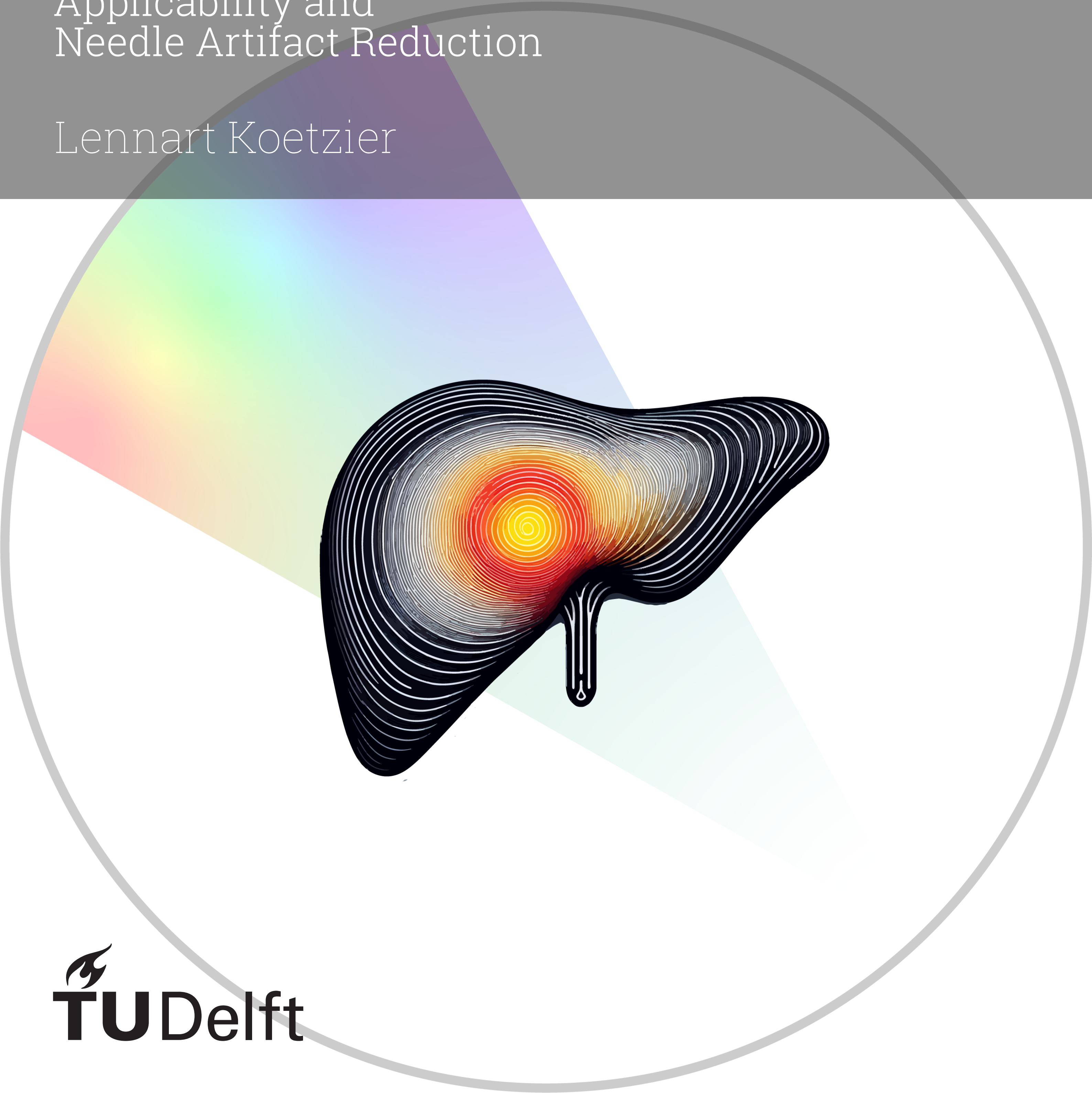

Spectral CT Thermometry for Thermal Liver Ablation

Applicability and Needle Artifact Reduction

by

Lennart Koetzier

to obtain the degree of Master of Science
at the Delft University of Technology,
to be defended on Thursday May 16, 2024 at 15:00.

Student number:	4660641	
Project duration:	September, 2023 – May, 2024	
Thesis committee:	Dr. M. Goorden,	TU Delft, supervisor
	Dr. J. Plomp,	TU Delft
	Dr. J. Heemskerk,	LUMC, daily supervisor
	P. Hendriks, MSc.,	LUMC, daily supervisor
Other supervision:	Dr. M. Burgmans,	LUMC, daily supervisor

Voorwoord

Voor u ligt de thesis met de titel 'Spectrale CT thermometrie voor thermale lever ablatie'. Dit onderzoek heb ik uitgevoerd bij het Leids Universitair Medisch Centrum in samenwerking met Philips en is onderdeel van mijn masteropleiding Biomedical Engineering, track Medical Physics, aan de Technische Universiteit Delft.

Graag wil ik eerst mijn begeleiding vanuit de TU Delft bedanken. Marlies Goorden wil ik graag bedanken voor de fijne samenwerking en het vertrouwen dat ze uitstraalde gedurende mijn project. Ook alvast mijn dank aan Jeroen Plomp, die dit project zal beoordelen en plaatsneemt in de afstudeercommissie.

Verder bestaat de afstudeercommissie uit mijn dagelijkse begeleiders, Pim Hendriks en Jan Heemskerk. De begeleiding van Pim heeft veel bijgedragen aan de goede uitkomst van dit project. Van varkenslevers snijden tot feedback geven op mijn werk, Pim was altijd beschikbaar voor hulp of gewoon een gezellig koffietje. Daarnaast wil ik Jan ook bedanken voor de hulpvolle begeleiding. Naast dat je technische input mij veel heeft bijgebracht over CT, heb ik ook genoten van de gezamelijke scansessies.
Niels van der Werf, bedankt voor je hulp bij het initiëren en in de lucht houden van dit project. Na onze eerdere samenwerking, voelde dit weer goed en vertrouwd, en ben ik blij dat er misschien meer in het vat zit. Ook Aart van der Molen wil ik bedanken voor het opzetten van en de betrokkenheid bij dit project. Mark Burgmans, bedankt voor jouw interesse en vertrouwen in dit project. Het zou fantastisch zijn als spectrale CT thermometrie jou binnenkort kan assisteren in de kliniek.

Ook ben ik de onderzoeksgroep voor nucleaire geneeskunde en interventieradiologie van het LUMC dankbaar voor de leuke tijd en de vele leerzame momenten. De activiteiten, zoals de bowlingavond en het nieuwjaarsfeest, waren momenten waarvan ik zeer heb genoten.

En last but not least, wil ik graag alle niet-academisch steun en gezelligheid bedanken gedurende mijn hele studietijd. Hiermee doel ik natuurlijk op al mijn vrienden, familie en Lara, waar ik altijd op heb kunnen bouwen en onmisbaar waren voor deze geslaagde tijd in Delft!

Lennart Koetzier
Delft, mei 2024

Samenvatting

Motivatie: Bij de behandeling van levertumoren wordt een techniek gebruikt genaamd thermale ablatie, waarbij tumoren worden verwarmd tot een temperatuur hoog genoeg om kankercellen te doden. Voor een effectieve behandeling is het essentieel om deze temperatuur nauwkeurig te monitoren. Een mogelijke methode om de temperatuur tijdens de behandeling te controleren is door middel van computertomografie (CT), maar dit kan soms onnauwkeurig zijn door beeldverstoringen van de ablatienaald die gebruikt wordt tijdens de procedure.

Onderzoeksdoelen: Dit onderzoek verkende een gespecialiseerde soort CT-beeldvorming genaamd spectrale CT thermometrie, die mogelijk een betere manier biedt om de temperatuur te monitoren zonder daarvoor temperatuursensoren in te brengen. De studie vergeleek verschillende methoden van CT thermometrie om te zien welke de meest reproduceerbare en nauwkeurige temperatuurmetingen geeft. Er werd ook gekeken naar verschillende manieren om beeldverstoringen te verminderen die veroorzaakt worden door de ablatienaald (naaldartefacten).

Methode: In het onderzoek werden kunstmatige levermodellen gebruikt die uitgerust waren met temperatuursensoren en onderworpen werden aan een ablatiebehandeling. Tijdens deze 10 minuten durende behandeling werden meerdere CT-scans uitgevoerd om dichtheidsveranderingen rondom de ablatienaald te meten. Deze scans werden verwerkt om zowel standaard CT-beelden als dichtheidsbeelden te produceren, waaruit vervolgens de temperatuur werd herleidt. Er werden verschillende scans gemaakt om de verandering in temperatuur over tijd vast te leggen en om verschillende technieken voor het verminderen van metaalartefacten te testen.

Bevindingen: De studie toonde aan dat er een zeer lineair verband bestaat tussen de gemeten CT-waarden en de gemeten temperaturen. De studie vond dat het gebruik van een combinatie van spectrale CT en metaalartefactreductie technieken de verstoringen door de ablatienaald kan verminderen en nauwkeurigere temperatuurmetingen kan bieden.

Conclusie: Deze studie illustreert dat spectrale CT een waardevolle methode kan zijn voor het verbeteren van de nauwkeurigheid bij het monitoren van thermale ablatiebehandelingen. De combinatie van spectrale CT met metaalartefactreductie kan de kans op een succesvolle behandeling verhogen door betere temperatuurcontrole. Verdere ontwikkelingen in CT-technologieën beloven nog nauwkeurigere methodes om de behandeling van levertumoren te monitoren.

Abstract

Motivation: Effective management of liver tumors through thermal ablation requires precise monitoring of the ablation zone to ensure successful treatment outcomes. Computed tomography (CT) thermometry offers a promising non-invasive solution to monitor if tumor cells have been heated to the lethal temperature threshold. However, achieving reproducible, precise, and accurate temperature measurements remains a challenge, particularly due to metal artifacts introduced by the ablation equipment.

Purpose: This study investigates the applicability of spectral CT thermometry in monitoring liver microwave ablation. It compares the reproducibility, precision and accuracy of CT thermometry on attenuation value images, with CT thermometry on physical density maps using spectral CT. Furthermore, it identifies the optimal metal artifact reduction (MAR) method — among O-MAR, deep learning-MAR, spectral CT, or a combination — to reduce needle artifacts and improve CT thermometry precision.

Materials and Methods: Four liver-mimicking gel phantoms embedded with temperature sensors underwent a 10-minute, 60W microwave ablation imaged by dual-layer spectral CT using a Philips CT7500 scanner. Each scan was processed to reconstruct standard 120 kVp images alongside physical density maps, which were derived from virtual monochromatic imaging (70 - 150 keV) and effective atomic number maps. During each procedure, 23 CT scans were acquired to monitor attenuation and physical density values in proximity of the ablation antenna over time. Attenuation-based and physical density-based thermometry models were tested for reproducibility (coefficient of variation) over three repetitions; a fourth repetition focused on accuracy (Bland-Altman analysis). MAR techniques were applied to a single repetition to evaluate temperature precision in artifact-corrupted slices.

Results: The correlation between CT value and temperature was highly linear with an R-squared value exceeding 96% for both attenuation and physical density-based thermometry. Model parameters for attenuation-based and physical density-based thermometry were -0.38 HU/ºC and 0.00039 ºC^{-1}, with coefficients of variation of 0.023 and 0.067, respectively, indicating a high reproducibility. CT thermometry precision increased with distance from the ablation antenna, the use of attenuation maps and deep learning-MAR. Physical density maps generated at 150 keV alone and in combination with O-MAR and deep learning-MAR reduced needle artifacts by 73% on average (p=0.003) compared to attenuation images. Bland-Altman analysis reveals limits-of-agreement of -7.7°C to 5.3°C and -9.5°C to 8.1°C for attenuation and physical density-based thermometry, respectively.

Conclusion: Spectral CT has the potential to make CT thermometry more universally applicable. This study demonstrates the effectiveness of spectral CT thermometry for non-invasive temperature monitoring during liver microwave ablation. It shows that using spectral physical density maps at 150 keV, alongside deep learning-MAR and O-MAR, enhances temperature accuracy and minimizes metal artifacts. However, standardizing thermometry parameters across different patient conditions remains a challenge. Future enhancements in photon counting CT and deep learning technologies could further refine this method, ultimately reducing the risk of local tumor recurrence.

Contents

Nomenclature

Abbreviations

Abbreviation	Definition
AM-PD	Alvarez & Macovski physical density
CT	Computed tomography
DL	Deep learning
HCC	Hepatocellular carcinoma
HU	Hounsfield unit
MAR	Metal artefact reduction
MRI	Magnetic resonance imaging
MWA	Microwave ablation
VMI	Virtual monochromatic image

Symbols

Symbol	Definition	Unit
A	Atomic mass	[-]
a	CT thermal sensitivity	[HU °C^{-1}]
E	Energy	[keV]
T	Temperature	[°C]
V	Velocity	[m s^{-1}]
Z	Atomic number	[-]
Z_{eff}	Effective atomic number	[-]
α	Thermal expansion coefficient	[°C^{-1}]
Φ	Photon fluence	[photons m^{-2}]
Ψ	Energy fluence	[keV m^{-2}]
μ	Linear attenuation coefficient	[cm^{-1}]
ρ	Physical density	[g cm^{-3}]

1

Introduction

Thermal ablation is a minimally invasive technique that employs thermal energy and can be used to treat hepatic lesions. In individual cases, thermal ablation may be preferred over other therapies, such as surgery or chemotherapy, depending on factors such as the tumor size and location, and liver function [1]. A typical ablation system consists of an energy generator and a needle-like electrode that delivers thermal energy percutaneously to the target tumor, causing coagulative tissue necrosis. For instance, radiofrequency ablation and microwave ablation (MWA) aim to heat the tissue to the cytotoxic threshold of at least 60°C. Alternatively, cryoablation cools the tissue to -40°C or lower to cause necrosis [2].

The interventional radiologist usually relies on image guidance, such as ultrasound, computed tomography (CT), or magnetic resonance imaging (MRI) to accurately position the electrode in the target tumor [3]–[5]. To evaluate the success of tumor ablation in the liver, it is essential to monitor the ablation zone, which is the region that reaches the cytotoxic temperature threshold. Besides electrode positioning, imaging assists the physician during and after the procedure to detect any residual tumor or collateral damage to healthy tissue [6], [7]. The ablation zone is commonly monitored based on differences in tissue perfusion that are caused by coagulative necrosis. First, a multi-phase pre-ablation scan with a contrast agent is made with CT or MRI to visualize the tumor. After ablation, another multi-phase contrast enhanced scan is made to verify non-enhancement of the ablated tissue, suggesting a successful ablation. However, interpreting these scans can be challenging. Tissue perfusion changes may occur not only in the areas subjected to high temperatures that are not lethal, but also as a result of vascular occlusion. Moreover, the ablated area and the surrounding tissue are prone to shrinkage and perfusional changes, making it insufficient to rely solely on post-ablation scans for identifying residual tumor tissue. Difficulties in detecting local residual tumor cells and determining technical success based on tissue perfusion imaging can contribute to high rates of local recurrence [8].

As an alternative to tissue perfusion imaging, tissue temperature can be directly monitored non-invasively. MRI-based thermometry, for example, is currently most trusted method and golden standard for this purpose [9]. While effective, interventional MRI is rarely applied due to high costs and the necessity for metal-free instruments. CT presents a cost-effective alternative that is already widely used for planning, probe positioning, and treatment confirmation. CT thermometry utilizes the inverse relationship between CT attenuation coefficient and tissue temperature. In this method, heating or cooling causes a change in tissue density, measurable through changes in Hounsfield Unit (HU), thus providing thermal feedback to the physician [10]. Furthermore, in-room CT imaging is especially suitable for thermal ablation due to its speed, high spatial resolution, and the capacity to depict tumors using contrast enhancement.

1.1. Background

1.1.1. Liver tumor

Hepatocellular carcinoma (HCC) is the most common type of liver tumor and is the fourth leading cause of cancer-related deaths worldwide. The incidence rate of HCC in Southern Europe, Western Europe, and North America lies between 10 to 15 per 100,000 population [11]. Key risk factors for developing HCC include chronic infections with hepatitis B or C viruses, excessive alcohol consumption, and metabolic liver disorders [12]. These risk factors can lead to liver cirrhosis, which may result in DNA damage within liver cells. This damage can trigger uncontrolled cell growth and the invasion of surrounding tissues. Unfortunately, a significant number of HCC patients are diagnosed at an advanced stage, which correlates with a poor prognosis and a five-year survival rate of only 18 percent [13]. Fortunately, screening programs targeting cirrhotic patients are being implemented to detect these tumors at an earlier stage.

Treatment strategies for HCC vary, depending on factors such as the cancer's stage, tumor size and location, and overall liver function. Historically, surgical resection or liver transplantation was considered the gold standard for HCC treatment. However, the feasibility of resection is often compromised due to underlying liver disease, the tumor's location, and the presence of multiple tumors within the liver. Moreover, both resection and transplantation are associated with significant morbidity and mortality risks due to their invasive nature [13]. In recent decades, there has been a shift towards local thermal ablation, which is gaining recognition as an effective, safe, and minimally invasive alternative. According to the Barcelona Criteria for Liver Cancer [14], for tumors smaller than 2 cm, ablation is the first-line treatment. In the case of tumors of 2 to 5 cm, surgical resection is recommended, although most patients are deemed unsuitable for this procedure. For the third category, which is bridging to transplantation, it is preferred to avoid surgery and ablation is favored to manage the condition until transplantation is possible. Compared to other treatment methods, ablation techniques are more cost-effective, better at preserving healthy liver tissue, and lead to reduced hospitalization durations [15].

1.1.2. Ablation techniques

Ablation techniques employ various energy sources to destroy tumors through either thermal heating or cooling. The specific technique used influences the energy transfer at the needle-tissue interface. Exposure to temperatures of 40–45°C can cause irreversible cellular damage if sustained for 30 to 60 minutes. However, at temperatures above 60°C, irreversible damage occurs much more rapidly due to swift protein denaturation and subsequent coagulative necrosis [2], [16].

Thermal ablation is recognized as a potentially curative treatment for hepatic tumors ineligible for surgical resection. It adheres to the oncological principles of resection regarding treatment margins [17]. The procedure targets not just the tumor itself, but also a safety margin of 0.5 to 1 cm of the adjacent liver tissue, to ensure complete eradication [18]. The success of the treatment hinges on heating the entire tumor and margin to temperatures that cause thermal coagulation necrosis. The goal of thermal ablation is to create large, predictable areas of necrosis to prevent any residual tumor and subsequent recurrence. However, the efficacy of thermal ablation decreases with distance from the ablation focus, limiting the size of the treatable tumor to typically 3 to 4 cm in diameter. To increase the size of the ablation zones, multi-needle ablations can be employed, allowing for the creation of larger necrotic areas. Despite this advantage and the guidelines provided in user manuals, the shape and size of the ablation zones tend to vary with each treatment, making the outcomes less predictable. This variability underscores the importance of imaging in assessing the success of the ablation.

In this study, MWA was utilized as heat energy sources to ablate liver tissue or phantom material. MWA uses electromagnetic waves within the range of 900–2500 MHz to heat the tissue. By inserting an antenna directly into the tumor, the electromagnetic field forces dipole molecules, mainly water, present in the tissue to align repeatedly with the rapidly changing electric field. Rotating these molecules increases their kinetic energy, thereby heating the tissue. Unlike radiofrequency ablation, MWA is not dependent on electrical currents passing through tissue, allowing it to reach temperatures above 100°C without the risk of vaporization of tissue interfering with thermal delivery [19]. MWA outperforms radiofrequency ablation by efficiently heating larger tumor volumes and reducing the heat-sink effect. It can directly warm tissues up to 2 cm from the antenna, a range not achievable with radiofrequency ablation. Additionally, MWA's use of multiple antennas can synergistically enlarge the ablation zone [20].

Parameter	**Requirement**
Temperature precision	<1–2°C
Spatial resolution	<1–2 mm
Acquisition time	<10–30 seconds
Three-dimensional temperature mapping.	
Measurements presented in real time.	
Insensitive to motion artifacts.	
Compatible with medical equipment.	
Radiation exposure from repeated CT measurement needs to meet safety standards.	

Table 1.1: Essential criteria for effective CT thermometry in ablation procedures [6].

1.2. Related work

The concept of CT thermometry is not new; its potential for non-invasive temperature monitoring was already explored in the seventies and early eighties [21], [22]. These studies demonstrated a temperature resolution of a fraction of degree Celsius with a spatial resolution of 1 cm. But, at that time, CT measurements were not reproducible due to unstable CT values and this application was not further developed until 1997 [23]. In that year, Jenne and colleagues proposed CT thermometry as a method for monitoring tumor ablation [24]. However, the reproducibility of CT values was still insufficient and thermal ablation was not widespread. It was only until the introduction of large multi-row detectors that CT thermometry began to gain renewed attention [25]. Meanwhile, Frich *et al*. outlined essential criteria for making non-invasive thermometry for thermal heating clinically viable, as summarized in Table 1.1.

In 2011, Pandeya *et al*. studied radiofrequency ablation on ex vivo bovine livers using a 128-slice scanner. They found a clear inverse relationship between CT value and temperature with a spatial resolution of 1.2 mm [26]. More recently, Pohlan's team examined CT thermometry's diagnostic accuracy in MWA and cryoablation procedures on ex vivo porcine livers. Their objective was to determine if CT thermometry could accurately predict whether tissue temperatures had surpassed a specific clinically relevant threshold. They reported an 89.2% predictive temperature accuracy for MWA, which dropped to 65.3% for cryoablation [27].

A recent development in CT thermometry is the use of spectral CT, showing potential to monitor temperature non-invasively with higher precision [28]–[30]. Liu *et al*. investigated the potential application of using physical density maps, produced with spectral CT, for conducting CT thermometry. The authors heated ex vivo bovine muscle tissue and found a linear correlation between temperature and physical density of 0.42% decrease in physical density with every 10°C increase in temperature [31]. In subsequent research, the team assessed the reproducibility, temperature precision, and radiation dose requirements of physical density-based thermometry in tissue mimicking phantoms. They concluded that physical density maps exhibited a strong and reproducible correlation with temperature in liver-mimicking phantoms. A clinically required temperature precision of <2°C could be obtained with a radiation dose of 2 mGy with additional denoising [32]. These findings increasingly enhance the feasibility of adopting non-invasive temperature monitoring during thermal ablation procedures.

However, the use of this physical density model remains untested for heating procedures with an ablation needle. This leaves open questions regarding the potential impact of gas bubbles or metal artifacts on physical density measurements. Specifically, there has been no investigation into the effectiveness of metal artifact reduction (MAR) techniques in mitigating artifacts induced by the ablation antenna.

1.3. Objectives and clinical relevance

This study investigates the applicability of spectral CT thermometry in monitoring liver MWA procedures. It compares the reproducibility, precision and accuracy of CT thermometry on attenuation value images from conventional CT, with CT thermometry on physical density maps using spectral CT. Furthermore, it identifies the optimal MAR method to reduce needle artifacts and improve CT thermometry precision.

- **Reproducibility assessment:** Evaluate the consistency of thermal sensitivity across different scanning repetitions using liver and liver-mimicking phantoms.
- **Temperature precision:** Investigate how temperature precision is affected by attenuation or density maps, radiation dose and slice thickness in the absence of metal artifacts.
- **The effect of metal artifacts and MAR:** Investigate the influence of metal artifacts on temperature precision and the effectiveness of MAR algorithms in mitigating this impact.
- **Temperature accuracy**: Investigate whether CT thermometry accurately represents tissue temperatures during thermal ablation.

The outcomes of this study hold significant clinical relevance as they promise to enhance the precision of CT-guided MWA procedures in liver treatments. By optimizing CT parameters and understanding the role of metal artifacts, this research aims to improve treatment safety and efficacy, ultimately benefiting patient care in interventional radiology.

2

CT physics

This section introduces the fundamental principles of CT, emphasizing topics relevant to this research. It begins with a broad explanation of photon physics, then narrows to explore the physics of photon attenuation and its significance in spectral CT. The chapter then discusses CT artifacts resulting from metallic objects, discussing three methods to reduce artifacts caused by ablation needles. Finally, it explains the principles of CT thermometry, the main focus of this research.

2.1. Photons and CT

CT uses the transmission of photons, exploiting the principle of differential attenuation across various tissues, to create detailed internal images of the human body. As a beam of photons traverses different materials, its intensity attenuates, which is dependent on the characteristics of the materials in the body. This attenuation of the photon beam encodes valuable information about the body's internal tissues. By acquiring these photon attenuation projections from multiple angles, it is possible to reconstruct cross-sectional images of the human body using dedicated software (Figure 2.1).

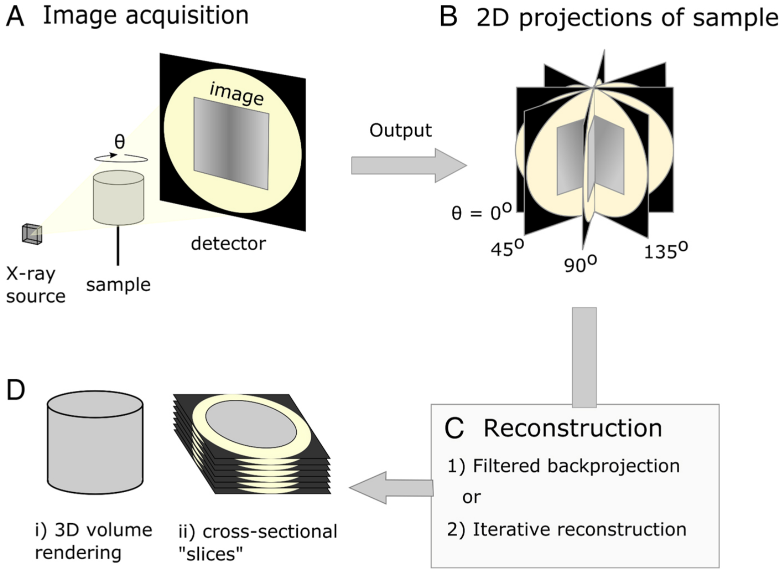

Figure 2.1: Schematic overview of computed tomography. **(A)** Depicts a simplified setup of the tomographic system, highlighting the x-ray source, the detector, and the object. The x-ray source and detector rotate around the object (Θ) to facilitate projection imaging. **(B)** Illustrates the raw data output as a collection of projection images captured from various angles. **(C)** Demonstrates the digital reconstruction phase, where projection images undergo processing through techniques like filtered backprojection and iterative reconstruction. **(D)** Shows the visualization of the sample in a image domain; this includes the 3D volume rendering **(Di)** as well as the option to examine 2D cross-sectional views or 'slices' **(Dii)** of the object. Figure adapted from [33].

Understanding photon physics is crucial in understanding the nuances in CT artifacts and spectral CT thermometry. High-energy photons or x-rays, characterized by frequencies much higher than visible light, belong to the spectrum of ionizing radiation. This form of radiation carries sufficient energy to eject electrons from atoms, resulting in the formation of ions and free electrons. It is important to note that these particles can break molecular bonds in the DNA, potentially resulting in cell mutations or cell death. This is the main reason why imaging with ionizing radiation such as high-energy photons should always be performed with great caution.

2.1.1. Generating the photon beam

In CT imaging, the production of photons within an x-ray tube primarily occurs through **bremsstrahlung** radiation. When electrons, emitted from a electrically-heated cathode, are accelerated towards a tungsten anode under high voltage (kV), they undergo rapid deceleration upon interaction with positive nuclei in the anode. The lost kinetic energy of electrons during deceleration is converted into the emission of a polychromatic spectrum of photon energies, characteristic of bremsstrahlung radiation. The highest possible energy of a photon is limited by the tube voltage, which, for instance, can be set to 100 kV and will result in photons of maximum 100 keV. Although a monochromatic photon beam would be ideal for CT to reduce artifacts such as beam hardening (Box *beam hardening*) and improve image clarity, achieving this is not feasible with current CT technology.

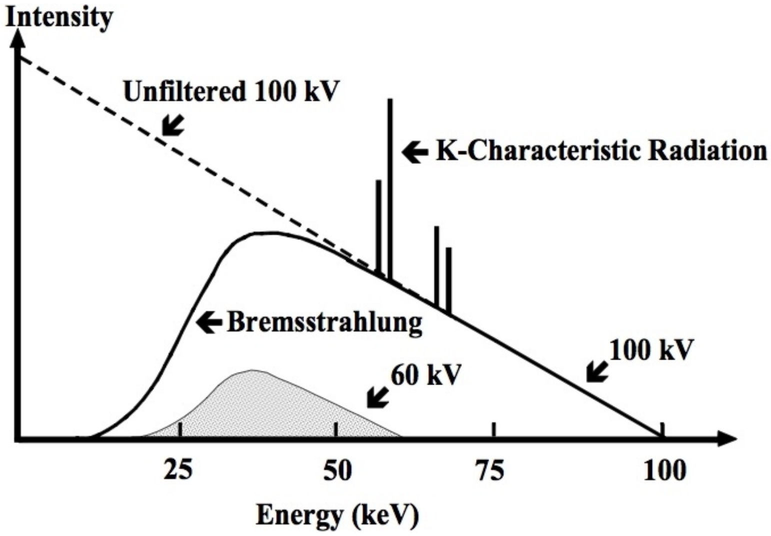

Figure 2.2: The graph illustrates the polychromatic energy spectrum of a photon beam at two distinct tube voltages, displaying the intensity distribution across energies. The spectrum is predominantly composed of bremsstrahlung, with characteristic x-rays manifesting as discrete peaks. Variations in tube voltage or the application of beam filtration are shown to cause a shift in the mean energy of the photon spectrum. Figure adapted from [34].

Beam hardening

Beam hardening is observable with polychromatic x-ray sources. As x-rays traverse the body, photons of lower energy are more easily absorbed, transmitting photons of higher energy that are less attenuated. Consequently, the transmission of the beam does not exhibit the simple exponential decay characteristic of a monochromatic x-ray source, resulting in a shift to a higher effective energy of the attenuated beam. This effect is especially seen in materials with high atomic numbers like bone, iodine, or metal, which show significantly higher attenuation at lower energies compared to materials with low atomic numbers such as water. Beam hardening artifacts typically manifest as dark streaks along the paths of highest attenuation and as bright streaks in other areas. These artifacts can be mitigated by using higher a tube voltage settings, employing modern scanners with beam hardening correction algorithms, or by using spectral CT to generate virtual monochromatic images (VMI) that are less susceptible to such effects [35].

The contribution of **characteristic x-rays** to the overall energy spectrum is relatively minor. Characteristic x-rays occur when these high-energy electrons eject inner-shell electrons from the tungsten atoms. This ejection leads to electron transitions from higher energy shells to fill the vacancies, creating a net energy loss, corresponding to the difference in energy levels. This process gives rise to the term 'characteristic radiation', as the magnitude of this energy difference is unique to specific atoms. Characteristic x-rays present as spike at certain energies in the polychromatic energy spectrum (Figure 2.2). When examining the properties of a photon beam that does not vary with time, it is crucial to consider the spectral quantities. These are represented as:

- The spectrally resolved **photon fluence**, denoted as Φ_E, which is the number of photons per unit area per unit energy interval, and
- The spectrally resolved **energy fluence**, denoted as Ψ_E, which is the energy deposited per unit area per unit energy interval.

To optimize the photon beam to reduce patient dose, a process called beam filtration is employed. The polychromatic nature of the photon beam necessitates filtering to narrow the range of photon energies, particularly by removing less penetrating photons. These low-energy photons contribute to patient dose, but do not enhance image quality because they do not reach the detector. By filtering the beam, the mean energy of the energy spectrum will also shift, which can result in a differences in image contrast.

2.1.2. Photon interactions and attenuation

After exiting the x-ray tube, photons travel through the object, experiencing various interactions influenced by the material they encounter. These interactions attenuate the photon beam by altering the photon's trajectory or completely stopping them, and we measure this attenuation in the projection domain. In CT imaging, which typically uses photon energies between 40 to 140 keV, the primary interactions are the photoelectric effect and Compton scattering. Rayleigh scattering also occurs, but plays a much smaller role:

1. **Photoeletric effect**: A photon interacts with the inner shell electron of an atom and ejects it from its shell. The ejected electron is known as a photoelectron, while the incident photon is completely absorbed in the process (Figure 2.3B). The energy of the ejected photoelectron is equal to the difference between the incident photon energy (E_0) and the electron binding energy (W):

   $$E_{e^-} = E_0 - W \tag{2.1}$$

   The free photoelectron subsequently loses energy by ionizing other atoms in the tissue and therefore contributes to patient dose.

   The probability of the photoelectric effect occurring is dependent on the incident photon energy and **atomic number** (Z) of the material. For the effect to happen with a K-shell electron, the incident photon must have energy exceeding the binding energy (W) of that electron. Notably, when the photon energy surpasses the binding energy of the K-shell electrons (known as the K edge), there's a marked increase in photon absorption. For instance, in iodine the K edge is at 33 keV, leading to a significant rise in photon interactions at this energy level. However, as the photon energy increases beyond the K edge, the probability of photoelectric absorption diminishes rapidly. Above this threshold, the photoelectric effect is proportional to $1/E^3$.

Furthermore, the probability of photoelectric absorption escalates with the atomic number, following a proportionality to Z^3 or Z^4. This effect is especially prominent when the atomic number is high, and the photon energy is just above the K edge. The photoelectric effect is the main source of image contrast in x-ray imaging, as it varies with the atomic number of the material. Different tissues in the body have different atomic numbers, and thus different absorption probabilities for photons. This contrast is more pronounced at lower photon energies.

2. **Compton scattering**: Compton scattering is a phenomenon where incident photons interact with outer shell electrons. During this interaction, the incident photon is scattered, losing a portion of its energy and changing direction (Figure 2.3D). The outer shell electron is ejected as a recoil electron and carries the lost energy of the photon as kinetic energy. This recoil electron contributes to the patient dose by losing its kinetic energy through excitation and ionization of other atoms in the tissue. A distinctive feature of Compton scattering is the remaining positive atomic ion, which has lost an outer shell electron and will eventually catch an electron again. Compton scattering is predominant in diagnostic radiology and can degrade image quality due to the scattered photons potentially reaching the detector. Moreover, scattered photons may undergo more interactions within the tissue.

   The probability of a Compton interaction occurring is determined by the electron density of the material and is inversely proportional to the photon energy, following a $1/E$ relationship. Additionally, the scattered photons can be deflected in any direction, including backscattering at 180 degrees from the incident photon. The Klein-Nishina electronic cross-section is used to model the probability of interaction of an x-ray photon photon with an electron in the tissue [36]. The energy dependence of the total cross-section for Compton scattering is represented by the dimensionless Klein-Nishina function:

$$f_{KN}(\alpha) = \frac{1+\alpha}{\alpha^2}\left[\frac{2(1+\alpha)}{1+2\alpha} - \frac{1}{\alpha}\ln(1+2\alpha)\right] + \frac{1}{2\alpha}\ln(1+2\alpha) - \frac{1+3\alpha}{(1+2\alpha)^2} \tag{2.2}$$

   where $\alpha = E_0/511$ keV [37].

3. **Rayleigh scattering**: When a low-energy photon interacts with an electron, it may be elastically deflected, a phenomenon known as coherent or Rayleigh scattering. This interaction temporarily elevates the electron's energy state without ejecting it from the atom. Subsequently, the electron falls back to its initial energy state, emitting a photon with the same energy but slightly altering the trajectory, as depicted in Figure 2.3C. In this scattering type, there is no net energy absorption, and the photons are deflected at a small angle. The likelihood of Rayleigh scattering is relatively minor in soft tissue, accounting for approximately 5 percent of all scattering. The intensity of Rayleigh scattering is greater in tissues with higher atomic numbers, due to the increased number of electrons available for scattering. Additionally, Rayleigh scattering is more pronounced at lower photon energies, as it is inversely proportional to about $1/E^{1.2}$ [38].

2.1.3. Photon beam attenuation

When a photon beam travels through the human body, it experiences attenuation, which is a decrease in its intensity caused by interactions with body tissues. This attenuation alters the photon beam's intensity profile upon exit, revealing information about the composition of the tissues it has passed through. The degree of attenuation is quantified by the linear attenuation coefficient, denoted as μ. While linear attenuation coefficients are practical for engineering purposes, their values are linked to the density of the

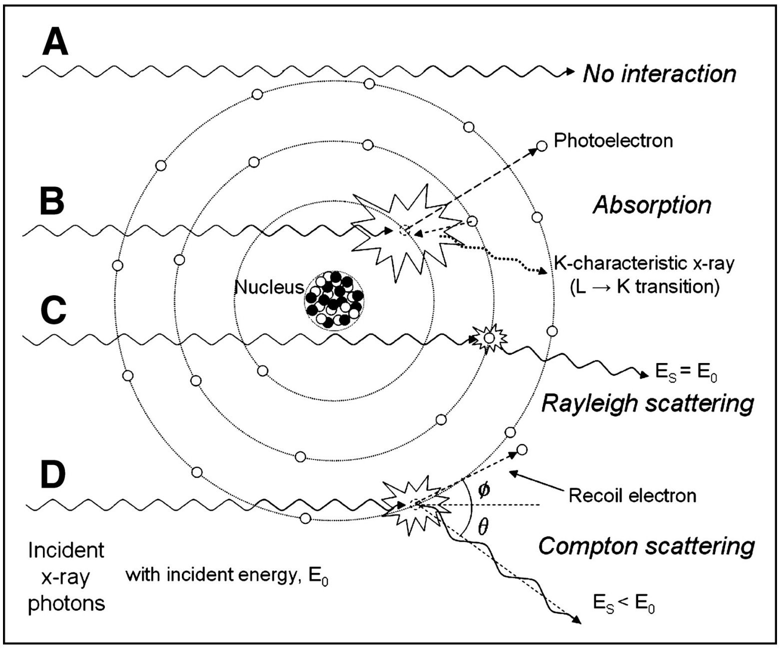

Figure 2.3: Schematic overview of x-ray photon interactions: **(A)** The primary beam traverses the material without attenuation, indicating no interaction. **(B)** Photoelectric effect occurs when an incident x-ray photon with energy surpassing an electron's binding energy is completely absorbed, transferring the excess to the kinetic energy of the photoelectron. **(C)** In Rayleigh scattering, the photon interacts with an electron or the atom as a whole without any energy transfer, thus the energy of the incident and scattered photons remains equal, only altering the photon's trajectory slightly. **(D)** Compton scattering involves interactions with quasi-free electrons, where energy is distributed between the ejected recoil electron and the scattered photon as determined by the Klein–Nishina function. Figure adapted from [38].

attenuating material, denoted as ρ, a property that varies with the material's physical state. Considering that the molecular binding energies are generally insignificant compared to the photon interaction energies within the diagnostic energy spectrum, it is reasonable to assume a direct proportionality between μ and the material's physical density besides its physical dependency on Z and E (section 2.1.2). This assumption is evident in the example of water in its various states: liquid, vapor, and ice. To normalize the linear attenuation coefficient for density variations, the mass attenuation coefficient (μ/ρ) is used. This standardization allows for consistent comparisons of a material's attenuation properties across its different states. Note that CT images display the linear attenuation coefficient as reconstructed from projection data. This coefficient is a product of both the mass attenuation coefficient and the physical density of the scanned tissues. The photon fluence of a monochromatic beam at a certain depth can be calculated by:

$$\Phi(x) = \Phi_0 \cdot e^{-\int \mu(E)dx} = \Phi_0 \cdot e^{-\int \frac{\mu(E)}{\rho}\rho dx} \tag{2.3}$$

where $\Phi(x)$ is the beam's photon fluence at a certain depth x in the body and Φ_0 is the beam's initial photon fluence before entering the object.

Mass attenuation coefficients for multi-element compounds can be *approximately* evaluated from the mass-weighted average fraction of each element's mass attenuation coefficient:

$$\frac{\mu(E)}{\rho} = \sum_{i=1}^{N} w_i \frac{\mu(E)_i}{\rho_i} \tag{2.4}$$

where w_i represents the proportion of the total mass attributed to element i, and $(\mu/\rho)_i$ denotes the mass attenuation coefficient for element i within the compound.

Beam polychromacy

As a polychromatic beam of photons passes through a medium, the beam's intensity diminishes due to attenuation. This phenomenon can be mathematically represented as follows:

$$\Phi_E = \Phi_E^0 \cdot e^{-\mu(E)x} \tag{2.5}$$

and

$$\Psi_E = \Psi_E^0 \cdot e^{-\mu(E)x}, \tag{2.6}$$

where Φ_E^0 and Ψ_E^0 denote the initial spectra of the photon fluence and energy fluence respectively and $\mu(E)$ signifies the total linear attenuation coefficient at a certain energy E. The expressions for the total photon fluence (Φ) and energy fluence (Ψ) at any given position within a single-elemental material are:

$$\Phi = \int \Phi_E^0 \cdot e^{-\mu(E)x} dE, \tag{2.7}$$

$$\Psi = \int \Psi_E^0 \cdot e^{-\mu(E)x} dE. \tag{2.8}$$

Because the photon beam is polychromatic and the human body consists of multi-elemental materials, we need to integrate over all energies and combine equations 2.3, 2.4, and 2.7. Equation 2.9 presents the formula for calculating the total energy fluence, (Ψ), of a polychromatic photon beam. This energy fluence is determined by the integrating the initial spectrally resolved energy fluence at each energy, attenuated by the integral of $\mu(E)$ over the path length x:

$$\Psi(x) = \int_E \Psi_E^0 \cdot e^{-\int_x \mu(E)dx} dE, \tag{2.9}$$

This equation represents the total photon energy measured at the detector as a line integral of the linear attenuation coefficient for the photon beam, a fundamental concept in CT image formation. By combining multiple projections an internal image of the body can be reconstructed. In a reconstructed scan, the resulting volume is composed of voxels, each reflecting the averaged linear attenuation coefficient over energy of the materials inside it. Because a voxel is not infinitely small, the individual elements are weighted and summed to an averaged attenuation coefficient. Subsequently, the linear attenuation coefficients of all voxels are scaled to obtain the CT value in HU:

$$HU = 1000 \cdot \frac{\mu(E) - \mu_{water}}{\mu_{water}} \tag{2.10}$$

where μ_{water} is the linear attenuation coefficient of water at room temperature.

The x-ray tube emits photons with a range of energies and a conventional scintillating detector (Box *scintillating detector*) integrates its measurement over all energies, meaning $\mu(E, Z)$ is averaged over all energies. This can result in different materials presenting the same CT values as the attenuation coefficient is influenced by both the material's Z and density. Spectral CT overcomes this by employing dual-energy measurements, allowing for improved material discrimination and facilitating new clinical applications.

Scintillating detector

A scintillating detector converts x-ray photons into an electrical signal and consist of three parts. In the upper scintillator layer, incoming x-rays are converted into visible light. This conversion occurs when the x-ray photons interact with the scintillator material, triggering the emission of secondary visible light photons. These photons are then captured by a photodiode, a device made from semiconducting materials, which quantifies the light intensity and produces an electrical signal. The signal reflects the cumulative energy deposited during the measurement interval rather than the energy of each individual photon, which is why it is referred to as an energy-integrating detector. Photon detectors are a critical component of CT systems, with extensive research dedicated to enhancing their sensitivity and efficiency.

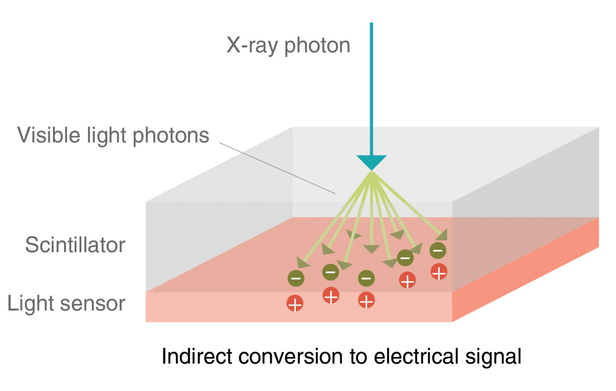

Figure 2.4: In a scintillating detector, an incoming x-ray photon is converted into multiple visible light photons within a scintillator. These photons then strike a light sensor positioned below, where they induce the production of positive and negative electrical charges. Figure adapted from [39].

2.2. Spectral CT

Spectral CT introduces the capability to measure attenuation across multiple energy spectra and use this extra information to analyze the elemental composition of tissues with greater detail. This technique leverages the energy-dependent attenuation characteristics of materials. In this subchapter, the physical principles underlying spectral CT are explored, delving into the computational algorithms enabling material decomposition, and reviewing the various technical methods used to acquire spectral data.

2.2.1. Requirement for multiple unique energy measurements

The general idea of spectral CT was first described by Godfrey Hounsfield and later investigated by Alvarez and Macovski [37]. It leverages the principle that the attenuation of photons varies according to both the energy spectrum and the type of material involved. As discussed in section 2.1, the material-dependent part of photon attenuation is dependent on the material's Z and density. If attenuation did not vary with the material, distinguishing between different materials would be impossible. Conversely, if there were no variation in absorption with different energies, data obtained from various energy spectra would be redundant.

Figure 2.5 plots the contributions of the photoelectric effect, Compton and Rayleigh scattering to the mass attenuation coefficient (μ/ρ) for muscle tissue and cortical bone on a log-log scale. In the analysis of muscle mass attenuation coefficients (Figure 2.5**a**), it is observed that Rayleigh scattering plays a negligible role compared to the photoelectric effect and Compton scattering within this energy range. Therefore, discussions on spectral CT often disregard Rayleigh scatter, focusing instead on the photoelectric effect and Compton scattering for the theoretical derivation of material decomposition. The photoelectric effect, which is highly energy-dependent, dominates at lower energies but diminishes rapidly with increasing photon energy. On the other hand, the energy dependence of Compton scattering is significantly weaker, making it the dominant interaction as photon energy increases. Spectral CT leverages these differential interactions for material differentiation and decomposition [40].

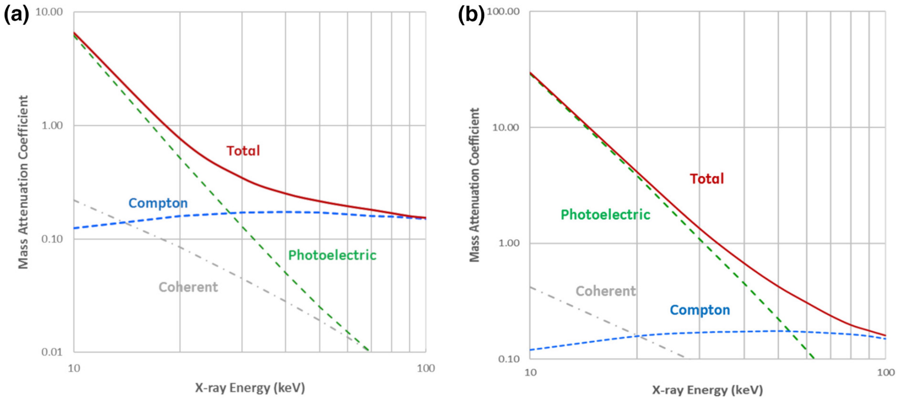

Figure 2.5: In the displayed log-log scale graph, mass attenuation coefficients are shown for muscle **(a)** and cortical bone **(b)**. Note the attenuation value ranges on the y-axis are different for muscle compared to cortical bone. Figure adapted from [40].

The behaviour of the photon interactions within muscle tissue is similar in cortical bone but at different scales, as illustrated in Figure 2.5**(b)**. Moreover, the mass attenuation coefficient significantly depends on the properties of the material, particularly its effective atomic number (Z_{eff}), which represents the weighted-average atomic number of a multi-element material within a confined volume. To demonstrate the requirement for multiple measurements at different energies, the linear attenuation coefficients for bone (ρ = 1 g/cm^3), iodine (ρ = 1 g/cm^3), and iodine with lower density (ρ = 0.1 g/cm^3) as a function of energy are shown in Figure 2.6. For two different materials, like iodine and bone, equivalent linear attenuation coefficients can be observed at a certain energy level, depending on the mass density of each material. At other energy levels, the difference in attenuation coefficient can be more pronounced. Spectral CT introduces an additional layer of differentiation. It measures attenuation at varying photon energy spectra, thereby enabling discrimination of materials based on both their effective atomic number (Z_{eff}) and the energy-dependent attenuation behavior.

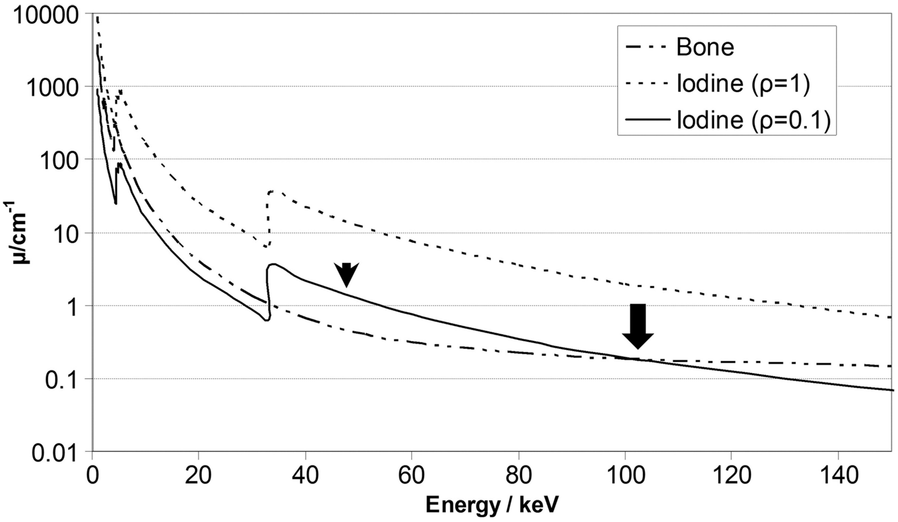

Figure 2.6: This figure plots linear attenuation coefficients for bone (ρ = 1 g/cm^3), iodine (ρ = 1 g/cm^3), and iodine at a lower density (ρ = 0.1 g/cm^3), as functions of energy. The graph shows that identical linear attenuation coefficients (μ(E)) can be found for different materials such as iodine and bone, as shown by the large arrow. By acquiring attenuation measurements at a different energy, indicated by the small arrow, it is possible to differentiate between the materials. Figure adapted from [41].

2.2.2. Material decomposition

The basis of most spectral mappings start with decomposing the materials in the image into two or more basis functions. The initial mathematical model for spectral CT was established in 1976 [37]. In this model, the mass attenuation coefficient for any given material is modeled by summing the contributions from the photoelectric effect and Compton scattering, both of which are functions of photon energy. The mass attenuation contributions from the photoelectric effect and Compton scattering are mathematically represented by $f_{PE}(E)$ and $f_{CS}(E)$, respectively. Therefore, the formula for calculating the total mass attenuation coefficient combines these contributions as follows:

$$(\frac{\mu}{\rho})(E) = \alpha_{PE} f_{PE}(E) + \alpha_{CS} f_{KN}(E), \tag{2.11}$$

where α_{PE} and α_{CS} are material specific coefficients that we would like to determine. If we ignore K-edges, $f_{PE}(E)$ and $f_{CS}(E)$ are monotonic and smoothly varying functions that are known from photon physics. The attenuation coefficients at low energy (E_L) and high energy (E_H) can be expressed as the individual contributions of the photoelectric effect and Compton scatter to the total attenuation:

$$(\frac{\mu}{\rho})(E_L) = \alpha_{PE} f_{PE}(E_L) + \alpha_{CS} f_{KN}(E_L) \tag{2.12}$$

$$(\frac{\mu}{\rho})(E_H) = \alpha_{PE} f_{PE}(E_H) + \alpha_{CS} f_{KN}(E_H) \tag{2.13}$$

Because all photon energy dependent parameters are known, α_{PE} and α_{CS} can be determined. This combination of (α_{PE}, α_{CS}) is unique per material and serves as the basis to characterize a material. However, if the material-of-interest has K-edges in the diagnostic energy range, these effects should be included in the model and additional measurements may be necessary.
Above model, however, has its limitations in accurately describing compound materials as molecular interactions are ignored [42]. As an alternative to basis functions that are used above, known-material attenuation functions can be used as the basis functions for material decomposition. For instance, the attenuation behaviour of water and bone are well known and other materials can be represented as a mixture or linear combination of these basis materials. Instead of Equation 2.11, the basis function are replaced by $(\mu/\rho)_A$ and $(\mu/\rho)_B$, which are the attenuation functions of basis materials A and B:

$$(\frac{\mu}{\rho})(E) = \beta_A(\frac{\mu}{\rho})_A(E) + \beta_B(\frac{\mu}{\rho})_B(E) \tag{2.14}$$

where β_A and β_B are the energy independent coefficients that we would like to determine.

After acquiring the spectral raw datasets, a E_L and E_H image can be reconstructed and equations 2.12 and 2.13 are solved on a voxel-per-voxel basis in the image domain. However, non-idealities in the acquisition process, such as beam hardening, can result in artifacts or inaccurate quantitative spectral reconstructions. Sinogram-domain (Box *Sinogram*) decomposition offers a solution to counteract inaccuracies like beam-hardening by using E_L and E_H sinogram data instead of reconstructed images [37]. This approach demands precise temporal and spatial alignment of high- and low-energy data. Movement of or within the subject during the high- and low-energy data acquisition phase can generate artifacts and quantitative inaccuracies. To address this, various technical implementations of spectral CT exist to ensure the high- and low-energy data remain consistent with each other. Moreover, although this discussion assumes data acquisition at two energy levels, the polychromatic nature of the beam adds complexity to material decomposition. Despite this, Alvarez and Macovski have shown that it is still possible to separate attenuation coefficients into their contributions from photoelectric and Compton effects.

Sinogram

A CT sinogram is a graphical representation of raw x-ray data collected from the CT detector as it rotates around a subject. A sinogram appears as a series of overlapping sinusoidal waves which encode the attenuation of x-rays as they pass through the body from various angles. Each point on the sinogram corresponds to a specific path the x-ray has taken, and the intensity of each point reflects the degree of attenuation along that path. In the sinogram, the x-axis represents the detector positions across the detector array, while the y-axis represents the gantry's rotation angle around the patient. Each full pass along the y-axis amounts to a complete 360-degree rotation, providing all the data required for accurate image reconstruction.

2.2.3. VMI and Z$_{eff}$

After material decomposition, the spectral data includes energy-independent information about the imaged materials. This information can be used to generate VMIs, which simulate the appearance of CT acquisition with an ideal monoenergetic x-ray source. Theoretically, it is possible to generate VMI at any specified energy, but considerations related to image quality and clinical practice often lead spectral CT systems to offer VMI within a 40 to 200 keV range. VMIs can be generated using:

- **Density-Based Approach**: This approach starts with calculating the mass densities of two basis functions using material decomposition. Here, the photoelectic effect and Compton scatter (Equation 2.11) can serve as basis functions or the mass attenuation functions of two basis materials can be used (Equation 2.14). Subsequently, these densities are used to calculate VMIs at a specified energy level using the known mass attenuation coefficients of the basis materials at the specified energy. Density-based VMI can be performed both in the image and sinogram domain.
- **Weighted Summation**: Alternatively, VMIs are derived by linearly combining the information from both low- and high-energy images. The VMI is a weighted sum of $CT(E_L)$ and $CT(E_H)$, and the weights are adjusted according to the desired energy level for the monoenergetic image in the image domain. However, since every material has a different $\mu(E)$ curve, weighted summation can never be fully accurate unless all materials in the object are mapped.

Another spectral mapping that can be generated after material decomposition is the effective atomic number (Z_{eff}), which is defined as:

$$Z_{eff} = (\sum_{i=1}^{N} f_i Z_i^{nz})^{1/nz} \tag{2.15}$$

where n_Z = 2.94 in correspondence with Hua *et al.* [43].

Using the results from material decomposition with Equation 2.11, the effective atomic number can be obtained by solving:

$$\alpha_{PE} = K_1 \, \frac{\rho}{A} \, Z_{eff}^n \tag{2.16}$$

$$\alpha_{CS} = K_2 \, \frac{\rho}{A} \, Z_{eff}, \tag{2.17}$$

where ρ/A and Z_{eff} are unknowns and K_1, K_2 and n are known constants.

Although material decomposition can serve as the basis for various spectral mappings such as iodine and electron density maps, this study will not consider them due to their lack of relevance to this study.

2.2.4. Technical approaches to spectral CT

There are several technical approaches to obtain spectral data, each with its own advantages and challenges (Figure 2.7) [41]:

A. **Dual x-ray sources**: Dual-source CT is a technique that uses two x-ray sources and two detectors mounted on the same gantry, positioned orthogonally to each other. Each x-ray source operates at a different tube potential and each detector collects the corresponding low- or high-energy data sets. The advantage of this method is that it allows independent control of the tube potential, tube current, and spectral filtration for each source-detector pair, which can improve the spectral separation and the noise performance of the spectral images. Moreover, this method also improves the temporal resolution of the conventional CT images, as the spectral data are acquired in a single rotation. However, this method also has some limitations, such as the reduced field of view due to the orthogonal geometry, and the increased cost and complexity of the dual-source CT system.

B. **Rapid kV-switching**: Another approach to spectral CT is to switch the x-ray tube potential between two values during the data acquisition. This can be done either between successive views or between successive rotations, depending on the speed of the tube potential switching. The advantage of this method is that it reduces the temporal misregistration between the low- and high-energy data sets, as the time interval between two projections is less than a millisecond. However, this method also poses some technical challenges, such as the need for fast and stable tube potential switching, the optimization of the tube current and spectral filtration for each tube potential, and the preservation of the spatial resolution and signal-to-noise ratio in the spectral images.

C. **Temporally sequential scans**: One of the simplest ways to perform spectral CT is to acquire two consecutive scans of the same object at different tube potentials, such as 80 kV and 140 kV. The advantage of this method is that it does not require any modification of the conventional CT hardware. However, the main drawback is the increased susceptibility to motion artifacts due to the time interval between the two scans, which can be several seconds. This can degrade the quality of the spectral images and the material decomposition results.

D. **Dual-layer detector**: A dual-layer detector is a type of detector that consists of two layers of scintillating material, each with a different thickness and energy sensitivity. A single x-ray beam with high tube potential is used and the low- and high-energy data is collected from the top and bottom layers of the detector, respectively. The advantage of this detector-based method is that it provides perfectly overlapping raw data, both spatially and temporally. This eliminates system-based motion artifacts and enables increased noise and artifact reduction in VMI [44] and beam hardening correction [45]. However, this method also faces some challenges, such as the optimization of the detector thickness and material, and the correction of the spectral distortion and cross-talk effects between the detector layers.

E. **Split-filter**: The split-filter technology uses a longitudinally arranged split filter, made of gold and tin, to achieve spectral separation of the polychromatic x-ray beam. At a tube voltage of 120 kVp, this configuration produces distinct low- and high-energy spectra. The primary advantage of this method lies in its retrofitting capability, enabling existing clinical CT scanners to adopt dual-energy imaging without extensive hardware modifications. However, it is important to note that the spectral separation offered by the split filter is comparatively low, which may affect the efficacy of material decomposition. Additionally, the finite size of the x-ray tube's focal spot produces a penumbra at the transition between the two filters, which decreases the spectral separation in the center of the beam.

F. **Photon-counting detector**: A photon-counting detector is a type of detector that can count and measure the energy of individual x-ray photons, using a semiconductor material, such as cadmium telluride. The advantage of this method is that it offers the possibility of multi-energy CT, as the detected photons can be binned into several energy windows, depending on the number and placement of the energy thresholds. This can enhance the material discrimination and quantification capabilities of spectral CT, especially for materials with K- or L-edges within the diagnostic energy range, such as iodine or gadolinium. However, this method also has some limitations, such as the high cost and complexity of the photon-counting detector, the low count rate and energy resolution of the current detector technology, and the correction of the non-ideal effects, such as pulse pile-up, charge sharing, and K-escape [39]. Currently, photon-counting spectral CT is limited due to a trade-off between a preferably high spatial resolution and energy separation. Effective energy separation requires a lower photon fluence; higher fluences will result in pulse pile-up, where photon-counting detectors are unable to distinguish between consecutive photons.

For a more in-depth review of approaches to obtain spectral data and clinical applications, we refer to an excellent review by McCollough *et al.* [41].

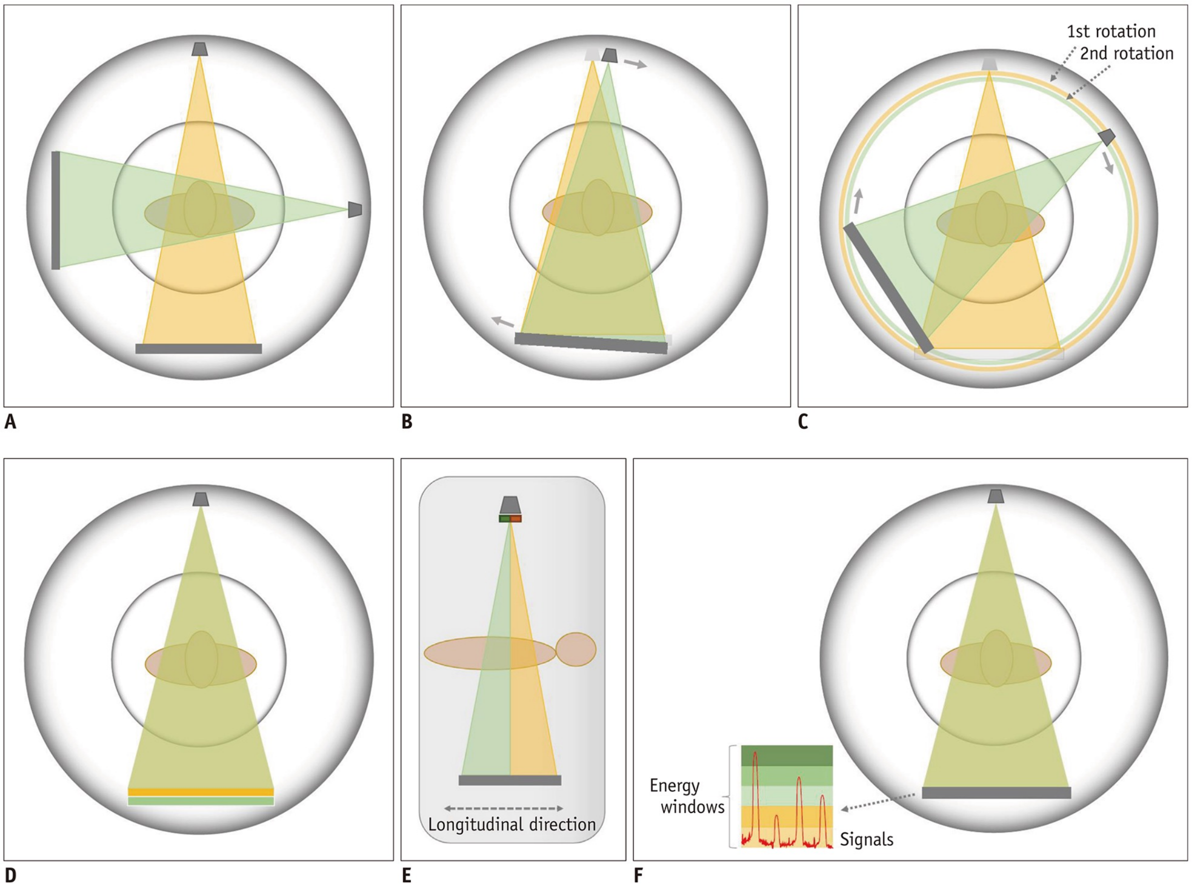

Figure 2.7: Approaches to acquiring spectral data that are currently available. **A.** Dual x-ray sources. **B.** Rapid kV-switching. **C.** Temporally sequential scans **D.** Dual-layer detector. **E.** Split-filter. **F.** Photon-counting detector. Figure adapted from [46].

2.3. Metal Artifacts

In an ideal scenario, by using high radiation doses, a monochromatic photon beam, infinite detector resolution, perfect detectors, absence of motion, and no scatter, CT images would reflect actual anatomical and pathological details without distortion. However, deviations from these optimal conditions can lead to artifacts. This paragraph discusses artifacts that are commonly encountered in CT, focusing on metal-induced artifacts, and how they can be reduced.
Metallic objects, such as dental fillings and orthopedic hardware, cause artifacts that appear as high and low attenuating streaks across reconstructed CT images. These artifacts degrade image quality by obscuring the metallic objects and the surrounding tissue, which may result in inaccurate diagnosis or missed findings [35]. In the context of thermal ablation procedures, needle-induced metal artifacts can hamper the visualization of the ablation zone during the procedure. Additionally, these artifacts may alter CT values, which makes quantitative CT techniques, such as CT thermometry, unreliable.

Metal artifacts are caused by several mechanisms, such as beam hardening, photon starvation, scattering, and edge effects. Beam hardening occurs as lower energy photons are attenuated more easily, while higher energy photons are more likely to penetrate, which is especially a problem with metallic object (see 2.1.2). Traditional image reconstruction techniques, such as filtered backprojection, assume that the spectrum does not vary along the beam direction, leading to a mismatch between the raw data and the algorithm and resulting in image artifacts. While modern algorithms like iterative reconstruction now integrate corrections for beam hardening, they still do not completely eliminate these artifacts [47]. In addition, Compton scatter causes photons to change direction and reach an incorrect detector. This scattering is amplified in the case of highly-attenuating objects, where predominantly scattered photons reach detectors that otherwise would detect very few photons. The reduced photon count at the detector is known as **photon starvation** and comes with a loss of projection data. Consequently, when photon beams are heavily attenuated, both beam hardening and scatter lead to an increased detection of photons than expected, resulting in dark streaks along the paths of highest attenuation. In addition, at the interface between dense objects and tissue, **edge effects** cause discontinuities in detector measurements, appearing as bright streaks along the objects boundary [35].

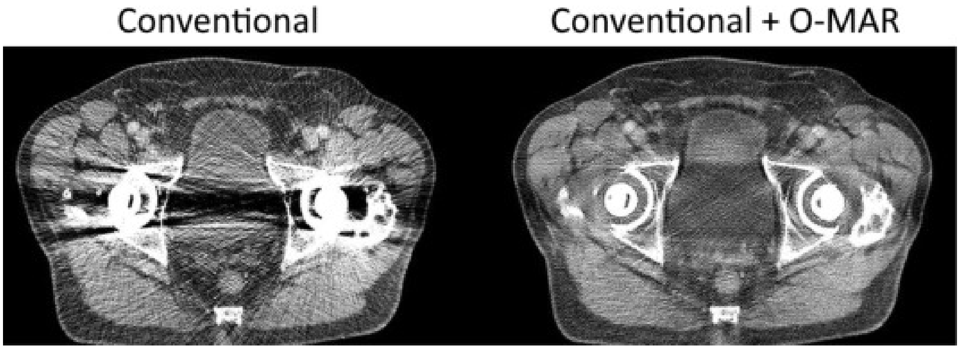

Figure 2.8: CT scan with bilateral hip arthroplasty demonstrating the effect of metallic implants (left) and metal artifact reduction with (right). The left image exhibits pronounced dark and bright streaks, a result of beam hardening and photon starvation, which obscure the implant and surrounding tissue. The right image shows a marked reduction using an iterative sinogram-based metal artifact reduction algorithm (O-MAR). Figure adapted from [48].

To enhance image quality, various metal artifact reduction (MAR) techniques have been developed for different applications, such as dental fillings, surgical clips, coils, and orthopedic hardware. These techniques range from tube prefiltration and iterative image reconstruction to specialized MAR algorithms like normalized MAR or frequency-split MAR [48], which often operate in the sinogram domain. This study includes a MAR technique that iteratively corrects the sinogram.

2.3.1. Iterative sinogram-based MAR

The first MAR technique evaluated in this study is a commercially available iterative approach to sinogram modification, called O-MAR (Philips Healthcare, Best, The Netherlands) [49]. This method starts by reconstructing an initial, uncorrected image directly from CT scan data, which serves as input for the first iteration. In each iteration, a series of steps are undertaken:

1. The uncorrected image is segmented into a tissue classified and a metal only image, using HU thresholding. In the tissue classified image, all pixels within a range near 0 are set to the average of the pixels within this range and other pixels are left unmodified.
2. The metal-only, tissue classified, and input image are forward projected into the sinogram domain.
3. The tissue classified sinogram is subtracted from the original image sinogram, resulting in the error sinogram, and should contain only metal pixels.
4. To remove any other nonmetal pixels from the error sinogram, a mask of the metal sinogram is applied.
5. Removed metal pixels are replaced with interpolated values which simulate tissue in place of the metal (Figure 2.9).
6. The error sinogram is back projected to make a correction image, which is then subtracted from the current input image to create the updated image for the next iteration.
7. Steps 1 - 6 are iteratively repeated until a point of convergence is reached.

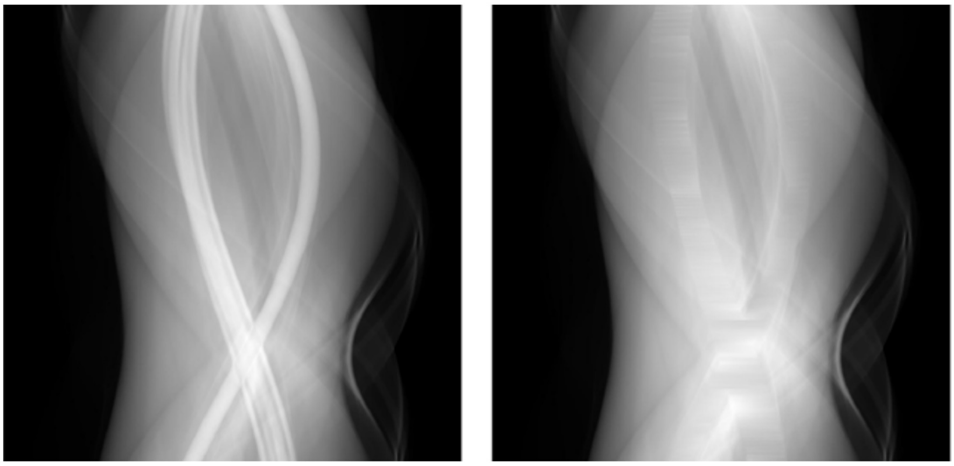

Figure 2.9: Original uncorrected sinogram containing projections from metal objects (left). After applying O-MAR, the metal projections in the corrected sinogram are replaced by interpolation with tissue projections (right). Figure adapted from [49].

In this algorithm, the accuracy of the metal-only mask serves as a critical foundation. It identifies projections within the sinogram affected by metal, ensuring the algorithm's modifications are targeted and precise. The use of a mask ensures that without presence of large clusters of metal pixels, the image will not be altered and therefore has no impact on nonmetal regions. However, in the first iteration, severe metal artifacts and hypodense areas in the initial uncorrected image may impact segmenting an accurate tissue mask. To circumvent this issue, the tissue mask is not generated from the initial uncorrected sinogram, but from the first metal-corrected sinogram. This sinogram is back projected and used to segment the tissue mask. This step is exclusive to the initial iteration, with no repetition in later stages. From the second iteration onward, the tissue mask is segmented from the updated input image as a substantial portion of metal artifacts has been reduced. Moreover, these corrections are specific to areas impacted by metal artifacts, thereby preserving the spatial resolution of uncorrected areas. This targeted approach differs from other algorithms that generate a completely new image for artifact correction, potentially compromising the spatial resolution of the corrected image [50].

Because the primary development of this MAR algorithm targets the reduction of artifacts induced by orthopedic hardware, there is an interest in investigating its efficacy in reducing artifacts from to metallic needles. Besides this dedicated MAR algorithm, this study focuses on two alternative approaches: spectral MAR and deep learning MAR, which are discussed below.

2.3.2. Spectral MAR

As discussed above, metal artifacts in polychromatic CT imaging mainly arise from beam hardening and photon starvation. Beam hardening stems from metals absorbing more low-energy photons, leading to a higher energy beam that underrepresents tissue absorption, causing dark streaks in images. Photon

starvation happens when metals absorb many photons, reducing the signal-to-noise ratio and producing similar dark streaks.
Spectral CT allows the generation of VMI across a broad energy spectrum (40-200 keV) by blending low and high-energy data with specific weighting factors. As VMI can emulate images that are acquired with high-energy photons, the mean beam energy suffers less “hardening”, in addition to the fact that more photons penetrate the metal as they travel through the body [51]. Spectral CT also enables examination of various energy levels, aiding radiologists in identifying the optimal balance to reduce metal artifacts without losing soft tissue contrast, which is generally better at low energies. This optimal imaging window is often between 100-140 keV [48]. In quantitative CT applications, where the focus is on precise measurements rather than visual inspection, the importance of image contrast is of less importance. In such contexts, the use of higher energy levels becomes a more feasible strategy for the reduction of metal artifacts. This ability to adjust VMI energy levels for certain cases, makes spectral CT a valuable tool in reducing metal artifacts.

Applying plain VMI to reduce metal artifacts is often not sufficient to reduce metal artifacts to an acceptable level. Therefore, VMI can be used in combination with other MAR techniques, as visualized in Figure 2.10.

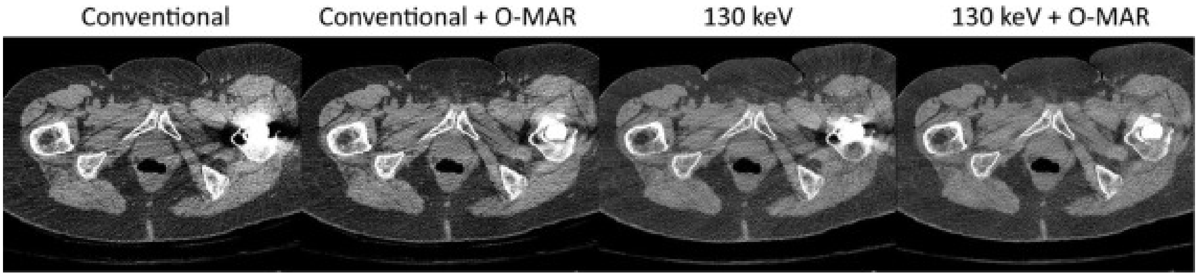

Figure 2.10: CT scan with unilateral hip arthroplasty demonstrating the effect of dedicated metal artifact reduction software (O-MAR) and virtual monochromatic imaging at 130 keV. In both the O-MAR and 130 keV VMI image, artifacts resulting from the hip implant continue to obscure surrounding tissue. The combination of 130 keV VMI and O-MAR shows superior artifact reduction over both plain O-MAR and VMI. Figure adapted from [48].

2.3.3. Deep learning MAR

Deep learning, a subset of artificial intelligence, is currently one of the most discussed techniques in medical research. The exponential growth of deep learning in healthcare is predominantly sparked by improved computational power and increased availability of healthcare data. This technology learns by processing labeled training data—where the inputs are paired with the correct outputs (ground truth)—enabling the models to improve iteratively, aimed at minimizing errors between predicted and ground truth.

Recently, deep learning-based MAR (DL-MAR) has been investigated. Researchers have developed DL-MAR algorithms that operate either in the sinogram or image domain and are trained through supervised or unsupervised learning methods, each demonstrating potential [48]. In supervised learning, algorithms typically require paired sets of input and ground truth images for training. However, this poses a challenge in metal artifact reduction, as often only the artifact-corrupted input images are available, without corresponding artifact-free ground truth images for comparison. The ground truth image, which would be the same image with metal but without the artifact, is often not available. To this end, Selles *et al.* used a method to simulate training data. Using metal-free CT images, both images with metal artifacts (input) and with metal but free from artifacts (ground truth) were simulated [52]. This approach enables the curation of large datasets with paired CT data that can be used for supervised learning. Furthermore, it facilitates the generation of training data with a diverse range of metal implants, such as small surgical clips and bilateral hip implants. In short the data generation process comprises the following steps:

1. **Water and bone images:** From the original CT image, a water image and a bone image is created.

2. **Anatomy identification:** Detect specific anatomical regions within the bone image and choose implant and position in bone image.
3. **Mask creation:** Create a metal mask that represents the shape and position of the metal implant.
4. **Projection and Simulation:** Generate forward projections for water, bone, and the metal mask to simulate projection data. Noise is also added in this step.
5. **Image combination and reconstruction:** Combine the simulated projections and reconstruct the image using filtered back projection to create an image with metal artifacts.
6. **Ground truth image generation:** Combine and reconstruct water and bone projections to create a ground truth image without artifacts, then replace CT values at position of implant with CT values of iron.

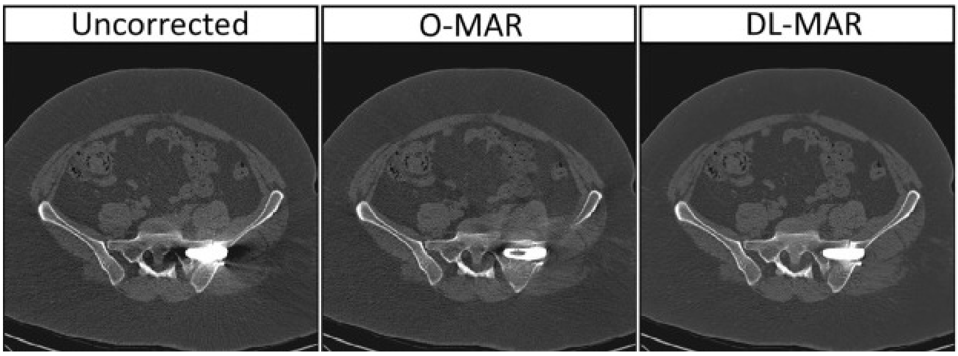

Figure 2.11: CT scan with an orthopedic hip screw demonstrating the effect of dedicated metal artifact reduction software (O-MAR) and deep learning-based metal artifact reduction (DL-MAR). In both the O-MAR and DL-MAR image, artifacts resulting from the hip screw were reduced. DL-MAR is able to reduce more artifacts in proximity of the metallic object. Additionally, while O-MAR introduced secondary artifacts inside the screw no secondary artifacts were introduced with DL-MAR. Figure adapted from [52].

Model training: the authors used this method to create a dataset of 105,163 artifact-corrupted images and paired ground truth, of which 83,192 served for training and 21,971 for model validation. A deep residual U-NET model was trained with a combined loss function prioritizing mean squared error (L2) loss, alongside structural similarity (SSIM) and mean absolute error (L1) losses. Optimization was performed using an Adam optimizer with an initial learning rate of 0.0001, adjusted by a ReduceLROnPlateau optimizer. Training data augmentation included probabilistic flipping, scaling, rotating, and shifting of the CT images. No augmentation was applied to the validation set. The model underwent 25 epochs of training with a batch size of 8, and the iteration with the lowest validation loss was selected as the final model.

2.4. CT thermometry

CT thermometry is a method that links changes in CT values to variations in temperature, based on the principle of thermal expansion. The influence of temperature on CT numbers was already investigated by Bydder and Kreel in 1979 to analyze the effects of temperature on the calibration process of CT scanners [22]. Until the introduction of spectral CT, temperature measurements relied solely on changes in CT attenuation [10]. Spectral CT, however, offers a new method to measure physical density with greater accuracy. The following section will explain these two methods in detail.

Principle of thermal expansion

The theory of thermal expansion is well understood; when a material is heated, its physical density is commonly reduced. This is expressed as:

$$\rho(T) = \frac{\rho(T_0)}{1 + \alpha\, \Delta T}, \tag{2.18}$$

where T_0 is the calibration temperature, $\Delta T = T - T_0$, and the thermal expansion coefficient is denoted by α. At an atomic level, this reduction in density can be attributed to the increased vibrational energy of atoms. As temperature rises, atoms vibrate more actively due to the increased thermal energy, causing them to occupy more space. This increase in the separation between atoms leads to a decrease in the material's density. These relationships, as visualized in Figure 2.12, explain the phenomenon of a decreasing CT value with increasing temperature and are the basis of CT thermometry.

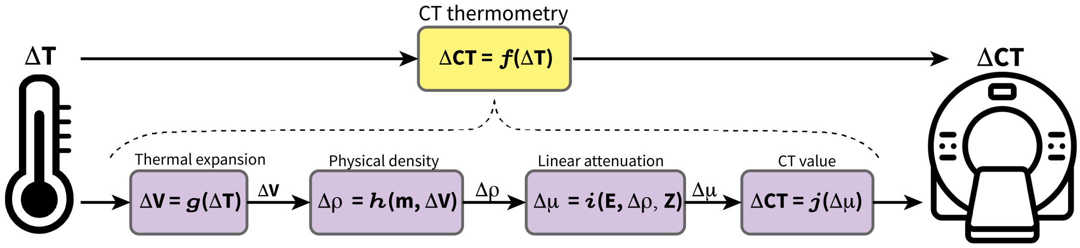

Figure 2.12: Schematic representation of the basic principles behind CT thermometry, illustrating the process from thermal expansion to CT value determination. The sequence involves transformations from temperature change (ΔT) to volume change (ΔV), physical density change ($\Delta\rho$), and linear attenuation change ($\Delta\mu$), finishing in the derivation of the CT value (ΔCT). Each transformation is influenced by specific parameters, indicating the relationship between the parameters.

CT attenuation-based

The temperature dependence of CT attenuation can be derived from the effect of thermal expansion on density. As shown in Figure 2.12, as temperature increases, density decreases, resulting in lower attenuation at higher temperatures. As proposed by Homolka *et al.* [53], linearization based on Taylor series expansion in $\alpha\Delta T$ gives:

$$[1 + \alpha\Delta T]^{-1} = 1 - \alpha\Delta T + O((\alpha\Delta T)^2) \tag{2.19}$$

The CT value at a given temperature relative to a reference temperature (T_0) can be noted as:

$$HU(T) \approx HU(T_0) - \frac{1000\; \mu(T_0)\; \alpha\; \Delta T}{\mu_{water}}. \tag{2.20}$$

With Equation 2.10 the change in CT value due to temperature can be approximated as:

$$\Delta HU(T) \approx -[1000 + HU(T_0)]\; \alpha\; \Delta T \tag{2.21}$$

where $\Delta HU = HU(T) - HU(T_0)$. This expression shows that temperature changes can be approximated by monitoring the CT values during an ablation. To examine how local temperatures affect the CT number and determine the thermal sensitivity, a regression analysis is conducted on the CT values and the corresponding temperature measurements:

$$\Delta HU = a\Delta T + b \tag{2.22}$$

The parameters temperature sensitivity (a) and intercept (b), measured in [HU/°C] and [HU] respectively, represent how HUs vary with temperature. This variation is specific to the type of tissue being imaged, the imaging protocol used, and how the tissue is heated. The slope of the fitted curve indicates the sensitivity of the attenuation-based CT thermometry: a larger slope reflects a higher thermal sensitivity a, which causes a greater change in CT numbers with temperature. The intercept b should approach 0 in this case. Multiple studies have investigated this linear relationship under varying circumstances and found temperature sensitivities ranging from -2.00 to -0.23 HU/°C for thermal heating (Appendix B).

Physical density-based

As can be seen in Figure 2.12, CT values not only reflect changes in temperature, but also changes in mass attenuation coefficient that result from changes in tissue composition. Moreover, in practice the scanner model and tube voltage influence the conventional HU, along with the patient size. These factors result in considerable variations in the thermal sensitivity values reported in prior studies (Appendix B). While a linear relationship has been used to model the dependence of attenuation on temperature with conventional CT, spectral CT can be used to develop more reproducible quantitative models by extracting material specific coefficients, α_{PE} and α_{CS}. Spectral quantifications not only provide more consistent and quantitative measures for diagnosis, but combining spectral maps can also be used to estimate other quantities, such as physical density.

The Alvarez-Macovski model [37] has been used in various simplified forms for the development of density mappings. One of these models is the Alvarez-Macovski physical density (AM-PD) model. It models the material specific coefficients α_{PE} and α_{CS} as follows:

$$\alpha_{PE} = K_1 \, \frac{\rho \, Z^n}{A} \tag{2.23}$$

$$\alpha_{CS} = K_2 \, \frac{\rho \, Z}{A}, \tag{2.24}$$

where K_1, K_2 and n are known constants. Combining this with Equation 2.11 results in the following relationship between attenuation coefficient and physical density:

$$\mu(E) = \frac{\rho}{A} \, [K_1 \, \frac{Z^n}{E^3} + K_2 \, Z \, f_{KN}(E)], \tag{2.25}$$

where E is the photon energy in keV and f_{KN} is the dimensionless Klein-Nishina function from Equation 2.2.

The research group of Noël has used these relationships to build two physical density models that rely on VMI and Z_{eff}, that are clinically available on spectral CT scanners [54]. Z_{eff} is computed on the scanner by comparing the measured α_{PE} and α_{CS} with materials with known α_{PE}, α_{CS} and Z. The effective atomic mass, A_{eff}, is not available on clinical scanners and was obtained by fitting a third-order polynomial between the atomic mass and number of the first 30 elements (H, He, Li, etc.), which yielded a good approximation, with R^2 = 0.9935:

$$A_{eff} = a_1 + a_2 Z_{eff} + a_3 Z_{eff}^2 + a_4 Z_{eff}^3 \tag{2.26}$$

where a_1, a_2, a_3, and a_4 are constants (Table 2.1). As VMI emulates the attenuation at a single energy, the linear attenuation coefficient, $\mu(E)$, can be extracted using Equation 2.10. By combining VMI, Z_{eff}, and A_{eff} the following model for physical density was used:

$$\text{(AM-PD)}: \qquad \rho = \frac{A_{eff} \, \mu(E)}{\frac{K_1 \, Z_{eff}^n}{E^3} + K_2 \, Z_{eff} \, f_{KN}(E)} \tag{2.27}$$

Additionally, this group utilized parameterized versions of the AM-PD model to account for multi-elemental tissues and model assumptions, such as the exclusion of Rayleigh scattering influence. They proposed the following parameterized version of the AM-PD model using VMIs of 70 keV:

(p. AM-PD) :

$$\rho = p_1 \frac{A_{eff}\ \mu^{p_2}(70keV)}{\frac{p_3\ Z_{eff}^{p_4}}{70^{p_5}} + Z_{eff}^{p_6}\ f_{KN}^{p_7}(70keV)} \tag{2.28}$$

The parameters of this model (Table 2.1) were fitted to 180 anthropomorphic tissues defined by the International Commission on Radiation Units and Measurements (ICRU) Reports 44 and 46 [55] with corresponding attenuation coefficients from the National Institute of Standard and Technology (NIST) XCOM [54], [56]. The authors validated the model's accuracy using a phantom containing inserts with known density and found a root mean square error of 0.0007 g/mL.

A_{eff}		Parametrized AM-PD	
a_1	0.436191	p_1	3.48632
a_2	1.85908	p_2	1.0704
a_3	0.015449	p_3	46.8754
a_4	-1.737E-4	p_4	4.1907
		p_5	2.94742
		p_6	1.01921
		p_7	0.995567

Table 2.1: Parameters for A_{eff} and AM-PD models [54].

The use of physical density maps for CT thermometry has been tested on a tissue mimicking phantom [32]. However, because differences in physical density are small when tissue is heated, the relative density is used instead of a density difference to perform the regression analysis to determine the parameters of the physical density-based model:

$$\frac{\rho(T_0)}{\rho(T)} = \alpha \Delta T + \beta \tag{2.29}$$

In the regression analysis, the thermal expansion coefficient (α) and the intercept (β) as defined in Equation 3.1 are determined. It is important to understand that these parameters, α and β, are distinct from a and b in Equation 2.22 and are independent of the imaging protocol employed.

Although the parameterized AM-PD method has shown promise for CT thermometry (see Appendix B and Figure 2.13), its use during heating procedures with an ablation needle remains untested. This leaves open questions regarding the potential impact of gas bubbles or metal artifacts on physical density measurements.

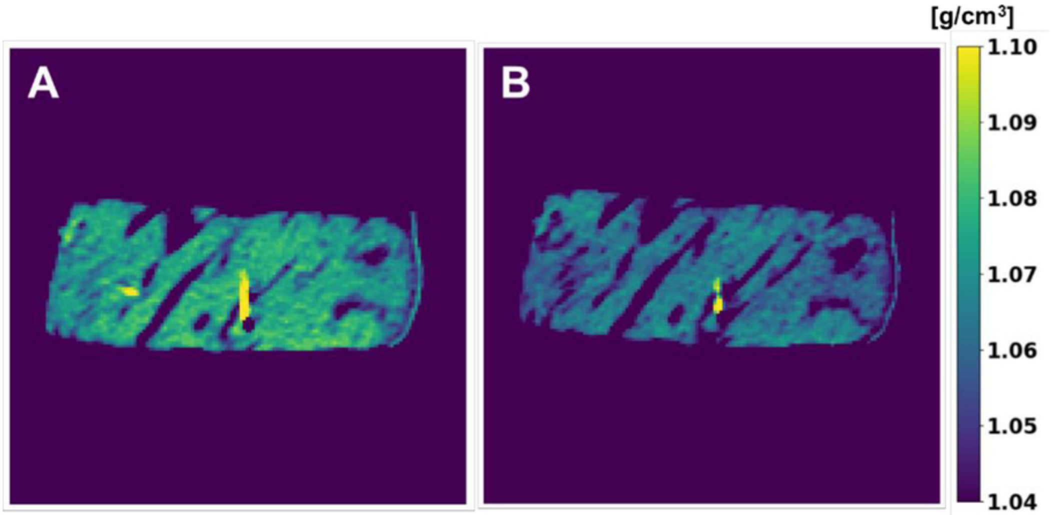

Figure 2.13: Physical density maps using the AM-PD model of ex vivo bovine muscle in a water bath at 22 °C **(A)** and 45.5 °C **(B)**. Physical density decreased with increased temperatures. The area of high physical density (yellow) corresponds to optical fiber temperature probes. These quantifications illustrate a strong relationship with change in temperature that corresponds to thermal volumetric expansion. Figure adapted from Liu *et al.* [57].

3
Materials and Methods

This chapter describes the materials and methods used in this project. A general description of the research setup is given after which the image processing and analysis is explained. Section 3.2 outlines the processing of the data used for building the CT thermometry models and making temperature maps. This is followed by section 3.3, which describes the different metrics to evaluate the applicability of CT thermometry.

3.1. Research setup

The study involved two scanning sessions where a total of six phantoms were heated through thermal MWA and imaged through CT. In this section, the materials, CT scan parameters, and the ablation procedure are detailed.

Ablation system: thermal heating was performed with a MWA system (EMPRINT, Medtronic, Minneapolis, USA) at a frequency of 2.45 GHz. This technique manages thermal control through a water cooling system extending to the antenna tip, and microwave field shape and wavelength regulation [58]. The MWA antenna tip was inserted to a depth of approximately 5 cm.

Temperature verification: four metallic k-type thermocouples (PH218, JBC tools, Barcelona, Spain) with 0.2°C accuracy and diameter of 0.4 mm were used to invasively verify material temperature around the MWA antenna. Thermocouples are small devices that consist of two dissimilar metal wires joined at one end, forming a junction. The junction generates a voltage that is proportional to the temperature difference and was measured by a dedicated instrument (NI-9211, National Instruments Corp, Austin, Texas, USA) that amplifies and converts the analogue voltage it into a temperature reading. A temperature logging tool (LabVIEW (DAQmx), National Instruments Corp, Austin, Texas, USA) logged temperature over time with a sample rate of 3 s^{-1}. Recorded temperature was logged in an Excel worksheet (Microsoft Office, Microsoft Corp, Redmond, WA, USA). The thermocouples were inserted at a depth of 4 cm on a horizontal line at different distances from the MWA antenna (Figure 3.1).

Scanning parameters: all CT acquisitions were performed with a dual-layer spectral CT (Spectral CT7500, Philips Healthcare, Best, The Netherlands). This system's detector has a thin yttrium-based scintillator to detect the low-energy x-rays, while a thicker gadolinium oxysulfide scintillator detects the higher-energy x-rays. The spectral material decomposition are based on the Alvarez and Macovksi model [37], and are performed in the sinogram domain. CT acquisitions were performed in axial mode with a tube voltage of 120 kVp and exposures of 387, 150, and 75 mAs. Collimation was set to 128 x 0.625 mm and the rotation time was 1.0 s. Images were reconstructed with a field of view of 350 mm, a smooth kernel B, and slice thickness/increments of 2.0/1.0 and 1.0/0.5 mm. The raw spectral data was sent to a dedicated workstation (IntelliSpace, Philips Healthcare, Best, The Netherlands) to generate the following spectral maps: VMI at 70, 90, 110, 130, 150 keV, and Z effective maps. Acquisition and reconstruction parameters are listed in Table 3.1. In addition to these parameters, in the second scanning session one repetition was reconstructed with an orthopedic MAR algorithm (O-MAR, Philips

Scanner	Philips Spectral CT 7500
Tube voltage	120 kVp
Exposure	387, 150, 75 mAs
Pitch	-
Rotation time	1.0 s
Collimation	128 x 0.625 mm
Slice thickness/increment	1.0/0.5, 2.0/1.0 mm
Kernel	B
FOV	350 mm
Matrix	512
Spatial resolution	0.683 mm
Reconstructions	120 kVp, VMI (70, 90, 110, 130, 150 keV), Z effective
Metal artifact reduction	DL-MAR, O-MAR

Table 3.1: Parameters for CT acquisition and reconstruction. VMI = virtual monochromatic image; DL-MAR = deep learning-based metal artifact reduction; O-MAR = orthopedic metal artifact reduction.

Healthcare, Best, The Netherlands). DL-MAR was applied employing the software developed by Selles *et al.* [52]. Both MAR methods were also applied in series (first O-MAR, then DL-MAR).
The DL-MAR algorithm was trained on a dataset containing images of predominantly orthopedic hardware in bone tissue, but no images containing needle-like object in soft tissue nor images of phantoms. Therefore, applying this algorithm in this study is an out-of-distribution use, which may lead to reduced performance.

3.1.1. Liver phantom

The initial ablation experiments were conducted on November 9th, 2023, at the University Medical Center Utrecht. These procedures utilized two porcine liver specimens that were approximately 60 hours post-extraction. Livers were collected from a local slaughterhouse and cut into cubes of roughly 8 x 8 x 8 cm. Each cube of liver tissue was placed into a transparant PMMA box with internal size 8.5 x 8.5 x 8.5 cm. This box contained holes to insert the ablation antenna and four temperature sensors. For the setup, the liver tissue was placed within an abdominal extension ring (Multi Energy phantom, Gammex™, Sun Nuclear, Middleton, WI, USA). The ablation antenna and thermocouples were placed on opposite sites and aligned in z-direction of the CT gantry. To precisely monitor the heat propagation during ablation, thermocouples were placed at distances of approximately 5, 10, 15, and 20 mm from the antenna. This arrangement is depicted in Figure 3.1.
Prior to starting the ablation procedure, a baseline scan was acquired with the ablation antenna and thermocouples in situ, serving as a reference for subsequent analyses. Subsequently, the tissue was heated at an ablation power of 100 W for 6 minutes and thermocouples recorded the internal temperature. The scanning protocol during the ablation had two phases: in the first 2 minutes of heating, a series of 8 scans were made at 15-second intervals. During the remaining 4 minutes an additional 8 scans were performed at 30-second intervals. During the two procedures, a total of 34 scans were made. After heating, a clear coagulative ablation zone was visible in the liver tissue (Figure 3.2).

3.1.2. Gel phantom

The second session of ablation experiments was conducted on February 19, 2024, at the University Medical Center Utrecht. Instead of porcine livers, a homogeneous polyacrylamide gel was produced to mimic the thermal, dielectric, and attenuation properties of a human liver [59]. In short, to prepare 1250 mL of polyacrylamide gel, 2.5 g of ammonium persulfate (Carl Roth GmbH, Karlsruhe, Germany) was dissolved in 6 mL of water. Separately, 725 mL of demineralized water was mixed with 500 mL of 40% acrylamide/bisacrylamide 19:1 (Carl Roth GmbH, Karlsruhe, Germany) solution. In concordance with

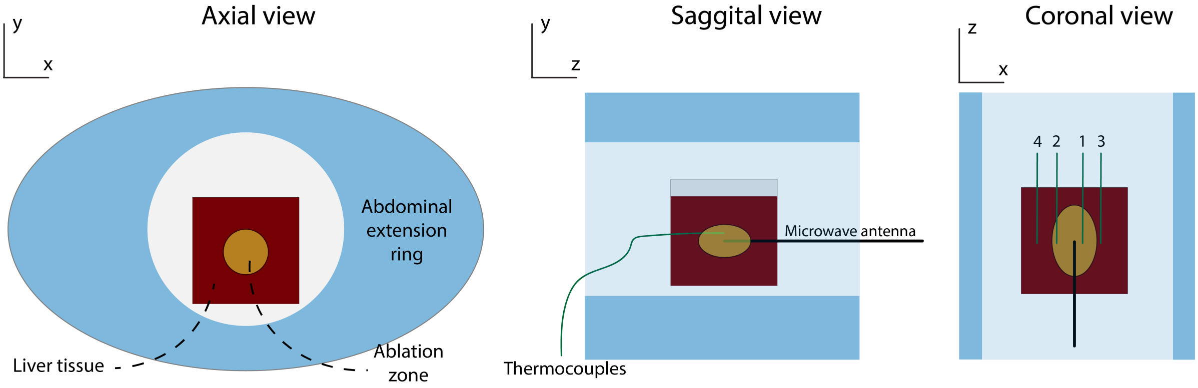

Figure 3.1: Schematic representation of the research setup of the liver phantom. Abdominal extension ring with, liver tissue box placed inside, was placed in the CT scanner. The thermocouple sensors were inserted at 5, 10, 15, and 20 mm from the microwave antenna.

(a) (b) (c)

Figure 3.2: Photos made of the research setup of the gel phantom. The abdominal extension ring with liver tissue was placed in the gantry of the CT scanner (a, b). After heating, a clear coagaluative ablation zone was visible in the liver tissue (c).

Leening *et al.* [32], 14.5 g of calcium chloride dihydrate (Carl Roth GmbH, Karlsruhe, Germany) was separately mixed in 25 mL water and added to the acrylamide/bis mixture. Then, to initiate and catalyze polymerisation, the ammonium persulfate solution and 2.5 mL of N,N,N',N'-tetramethylethylenediamine (Carl Roth GmbH, Karlsruhe, Germany) were added to the acrylamide solution. Finally, the gel was quickly poured into the four PMMA boxes, sealed airtight, and stored overnight in a refrigerator at 4°C. The phantom was then moved to room temperature until use.

For this setup, the ablation antenna and thermocouples were placed on opposite sites and aligned in x-direction of the CT gantry. This orientation of the ablation antenna, typically inserted in an anterolateral manner into the patient, aligns more closely with clinical practice than with the z-direction orientation. As a consequence, this alignment is expected to result in a higher presence of in-plane metal artifacts. Due to size constraints, the gel phantom was not placed within the abdominal extension ring. To monitor the heat propagation during ablation, thermocouples were placed at distances of approximately 10, 15, 20 and 25 mm from the antenna.

Prior to starting the ablation procedure, a baseline scan was acquired with the ablation antenna and thermocouples in situ. Subsequently, the gel phantom was heated at an ablation power of 60 W for 10 minutes and thermocouples recorded the internal temperature. The scanning protocol during the ablation had two phases: in the first 2 minutes of heating, a series of 7 scans were made at 15-second intervals. During the remaining 8 minutes an additional 15 scans were performed at 30-second intervals. After heating, a clear ablation zone was visible in the gel phantom (Figure 3.3b). This procedure was repeated 4 times, 3 times with a high exposure of 150 mAs, once with a low exposure of 75 mAs. During these four repetitions, a total of 94 scans were made.

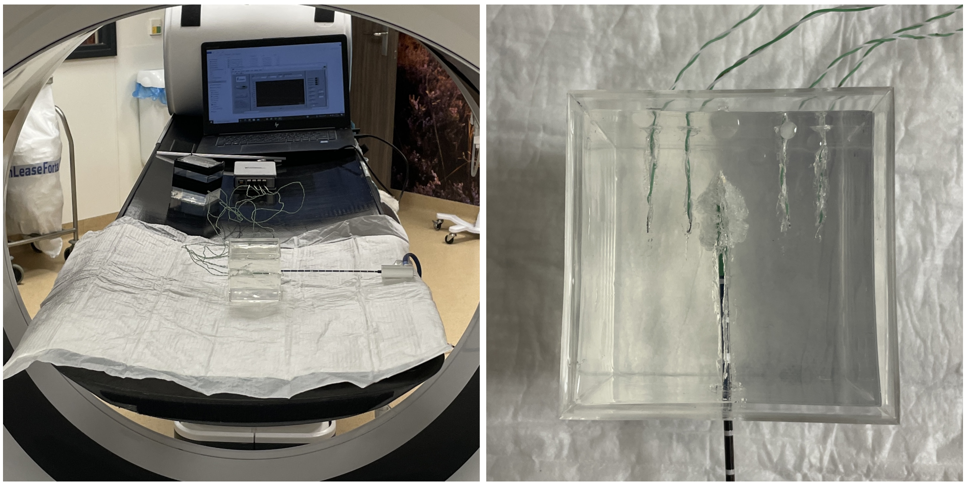
(a) (b)

Figure 3.3: Photos made of the research setup of the gel phantom. The gel phantom was placed in the gantry of the CT scanner and the ablation antenna was inserted in x-direction of the gantry (a). After heating, a clear ablation zone was visible at the tip of the antenna in the gel phantom. Temperature sensors were inserted at radial distances of 10, 15, 20 and 25 mm from the ablation antenna as seen in the top view in (b).

3.2. Image processing and analysis

The analysis of the acquired scans was conducted using a suite of software tools. Spectral mappings, including VMI and Z effective maps, were generated with IntelliSpace. Furthermore, a dedicated pipeline was built using Python 3.10, developed within the PyCharm environment (version 2023.1, Prague, Czechia). This pipeline was designed to process all acquired scans and temperature data. It encompasses the entire spectrum of data processing: the generation of physical density maps, automatic segmentation, determining model parameters, reproducibility, precision and accuracy of the CT thermometry models, and generation and visualization of temperature maps. The individual components of this pipeline are detailed in the subsequent sections. As the analysis was performed on both HUs and physical density we will simply refer to CT value for both terms.

3.2.1. Automatic segmentation of ablation needle and temperature sensors

The pipeline starts with the segmentation process, where the `ObjectAnalyzer` class identifies and isolates the ablation needle and temperature sensors from the CT scan data. Imported DICOM files undergo thresholding based on predefined values for the ablation antenna (1500 to 4000 HU), and temperature sensors (700 to 1200 HU). After refinement using morphological (closing) operations, sensor tips are located and used for subsequent region of interest (ROI) measurements, which was managed by the `ROIMeasurements` class.

3.2.2. Generating physical density maps

The `AM_PD.py` script serves as the backbone for generating physical density maps through the reparameterization of the AM-PD model. As described in section 2.4, the parameterized version of the AM-PD model was fitted to the physical density, effective atomic mass and number, and linear attenuation of 180 human tissues with or without iodine contrast. A list was made of physical density and the elemental composition of these materials [55]. The elements included elements are: H, C, N, O, Na, Mg, P, S, Cl, K, Ca, Fe, and I.

The developers of this model only parameterized this model for an x-ray energy of 70 keV [54]. Because the linear attenuation coefficient of materials varies with x-ray energy, the parameters of the model were fit to an energy range of 40 - 200 keV to enable the use of VMI in this energy range. To this end, the effective atomic number and mass of 180 materials were calculated using relations 2.15 and 2.26. Mass attenuation coefficients were retrieved from a well-accepted material property dataset [56] (Table 3.2). For every energy level within the 40-200 keV range, the optimal fit parameters (p_1 to p_7) for the parameterized AM-PD model (Equation 2.28) were found using a least squares fit. This approach aims to align the model closely with the reported physical density values. To measure and compare model accuracy, the absolute error and root mean square error (RMSE) relative to the reported physical density values were calculated. Subsequently, physical density maps of all CT acquisitions on the liver and gel phantom were generated using the reparameterized AM-PD model.

		Elemental mass fraction									Mass attenuation			
Tissue	ρ (kg/m^3)	H	C	N	...	S	Cl	...	Fe	I	μ/ρ (50 keV) (cm^{-1})	μ/ρ (70 keV) (cm^{-1})	μ/ρ (110 keV) (cm^{-1})	μ/ρ (150 keV) (cm^{-1})
Adipose tissue	970	1.12E-01	5.17E-01	1.30E-02		1.00E-03	1.00E-03		0.00E+00	0.00E+00	2.14E-01	1.88E-01	1.64E-01	1.50E-01
Iodinated blood	1064	1.02E-01	1.10E-01	3.30E-02		2.00E-03	3.00E-03		1.00E-03	3.77E-05	2.28E-01	1.92E-01	1.65E-01	1.49E-01
Heart	1050	1.03E-01	1.21E-01	3.20E-02	...	2.00E-03	3.00E-03	...	1.00E-03	0.00E+00	2.26E-01	1.92E-01	1.65E-01	1.49E-01
Liver	1060	1.02E-01	1.39E-01	3.00E-02		3.00E-03	2.00E-03		0.00E+00	0.00E+00	2.27E-01	1.92E-01	1.64E-01	1.49E-01
Skeleton-cartilage	1100	9.60E-02	9.90E-02	2.20E-02		9.00E-03	3.00E-03		0.00E+00	0.00E+00	2.33E-01	1.94E-01	1.64E-01	1.49E-01
Iodinated kidney	1056	1.03E-01	1.32E-01	3.00E-02		2.00E-03	2.00E-03		0.00E+00	5.71E-05	2.27E-01	1.92E-01	1.65E-01	1.49E-01

Table 3.2: An excerpt of the 180 ICRU materials with their physical density, elemental composition, and some attenuation values.

CT thermometry

CT thermometry correlates changes in CT values with temperature variations, relying on thermal expansion principles. As a material is heated, its physical density typically decreases, captured by the relationship:

$$\rho(T) = \frac{\rho(T_0)}{1 + \alpha \, \Delta T}, \tag{3.1}$$

In this study, linear regression was used to define two CT thermometry models. These models are described as follows:

Attenuation-based:

$$\Delta HU = a \Delta T + b \tag{3.2}$$

and

Physical density-based:

$$\frac{\rho(T_0)}{\rho(T)} = \alpha \Delta T + \beta \tag{3.3}$$

In the attenuation-based model, absolute changes in CT values are linearly correlated with temperature variations, allowing the determination of the thermal sensitivity a and intercept b. For the physical density-based model, relative density changes are correlated with temperature change to establish the parameters α and β, reflecting the tissue's thermal expansion coefficient and intercept.

3.2.3. ROI measurements

Assuming radial symmetry of temperature aorund the ablation antenna, two circular ROIs are placed adjacent to the tip of the temperature sensors as visualized in Figure 3.4. Voxels are thresholded to account for gas bubbles inside the tissue. CT value mean and standard deviation are measured. ROI measurements are performed individually for each scan and for each temperature sensor in that scan.

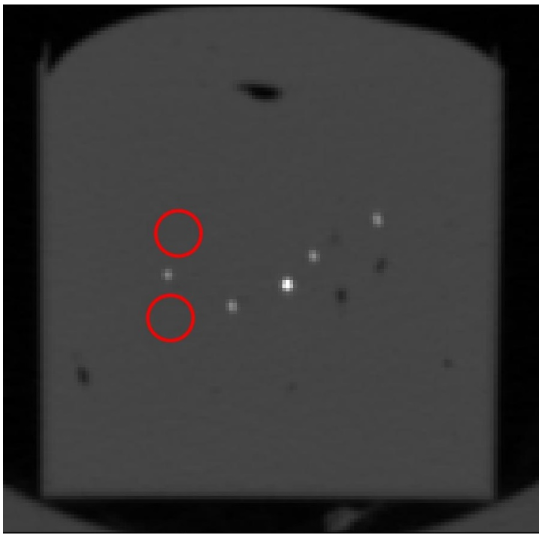

Figure 3.4: Region of Interest placement for both the liver and gel phantom. The central bright point is the ablation antenna. The surrounding darker points are the temperature sensors.

3.2.4. Determining thermometry model parameters

Prior to conducting regression analysis for thermal sensitivity assessment, the temperature data from the thermocouples were synchronized with the time stamps of CT scans. This synchronization ensures accurate pairing of each sensor's temperature reading with its corresponding CT value as measured in the ROIs.

In the script `TemperatureHURegression` class, regression analysis was executed to correlate the temperature measurement over time with the variation of CT value, and to determine the thermometry model parameters a or α and b or β. This analysis quantifies the relationship between temperature and HU or physical density, as represented by the equations 3.2 and 3.3 and recapitulated in Box *CT thermometry*.
For each repetition and sensor, a weighted linear regression, was performed using the `statsmodels` package. The weighting was based on the inverse variance of each ROI measurement, thus incorporating the uncertainty of ROI measurements into the analysis. Reference values T_0 and $CT(T_0)$, denoting the temperature and CT value before starting ablation procedure, were utilized. Subsequently, for every sensor and repetition, the derived parameters, and squared correlation coefficient (R^2) were recorded. To determine the parameters of the general models for CT thermometry in liver tissue and gel phantoms, a weighted linear regression was conducted on the combined data from all temperature sensors within one repetition. These models were fitted to CT series with highest dose and thickest slices to reduce uncertainty in ROI measurements. No MAR was applied to these series. The resulting parameters are averaged over the repetitions and the standard deviation are recorded.

3.2.5. Visualization of temperature maps and isolines

The visualization of temperature distribution within the tissue was accomplished by the `TempMap` class. This class employs the CT thermometry models found in 3.2.4 to convert the CT scans made during the ablation procedure into temperature maps. First, noise in the volumes was reduced by applying non-local means denoising which was implemented through the `scikit-image` package. This method operates by comparing each patch of the volume to other patches in a local neighborhood, thus allowing for the preservation of essential structures while effectively reducing noise. In this implementation, non-local means was applied to three-dimensional volumes with a noise standard deviation (σ) of 2.1, using 2x2 mm patches within a 6x6 mm search area, and a filtering parameter h set to 0.8xσ, all to ensure noise reduction while preserving small structures and gradient. The patch size and search area are optimized in the non-local means denoising process to effectively reduce noise and preserve both details and gradients in the temperature maps. The denoising was expedited by enabling fast_mode, which approximates patch comparisons for efficient computation. After denoising, rigid registration of CT scans from different time points to the reference scan was performed, ensuring accurate spatial alignment. This is important to accurately detect local difference in CT value after heating the tissue.

By applying attenuation or physical density-based thermometry, these volumes are transformed into temperature maps, visualizing the distribution and intensity of heat throughout the tissue. Additionally, temperature isolines and temperature overlay images can be generated in this class. The use of temperature isolines on the pre-ablation image provides an insightful representation of relevant temperatures, while having a reference where the tumour is. A temperature overlay on the pre-ablation image similarly provides information about spatial distribution of heat in the tumour and surrounding tissue.

3.3. Statistical analysis

3.3.1. Thermometry reproducibility

Parameters of the attenuation-based (Equation 3.2) and physical density-based thermometry model (3.3) were determined in section 3.2.4. The consistency of fit parameters was evaluated using the coefficient of variation (CV), defined as the standard deviation normalized by the mean. Additionally, scatter plots were created to visualize thermal volumetric expansion in each of the repetitions.

3.3.2. Temperature precision

In this study, the metric temperature precision was used. Temperature precision is defined as the maximum error between modeled and actual temperature measurements. This measure is vital for evaluating the precision of CT thermometry, where CT-based temperature measurements are influenced by measurement uncertainties, such as noise and metal artifacts, as well as uncertainty in thermometry model parameters. These uncertainties can undermine the reliability of CT thermometry, hence the need for a robust measure of precision.

Temperature precision was quantified by propagating the uncertainties in CT images and model parameters to ΔT as measured with CT thermometry. This metric quantifies the degree of uncertainty in ΔT attributable to uncertainties within the inputs of the thermometry model. This was done through mathematical error propagation for functions of multiple sources of uncertainty in the thermometry models:

$$\delta T = \sqrt{\left(\frac{\partial T}{\partial CT(T)}\delta CT(T)\right)^2 + \left(\frac{\partial T}{\partial CT(T_0)}\delta CT(T_0)\right)^2 + \left(\frac{\partial T}{\partial p_1}\delta p_1\right)^2 + \left(\frac{\partial T}{\partial p_2}\delta p_2\right)^2} \tag{3.4}$$

where $\delta CT(T_0)$ and $\delta CT(T)$ are the uncertainties of the ROI measurements in CT images at lowest and highest temperature, respectively. δp_1 and δp_2 are the standard deviations in the thermometry model parameters a or α and b or β, respectively.

More specifically, by applying the model for attenuation-based thermometry (Equation 3.2), temperature precision was calculated through error propagation as follows:

$$\delta T = \sqrt{\left(\frac{1}{a}\delta HU(T)\right)^2 + \left(-\frac{1}{a}\delta HU(T_0)\right)^2 + \left(-\frac{1}{a}\delta b\right)^2 + \left(-\frac{\delta a}{a^2}(HU(T) - HU(T_0) - b)\right)^2} \tag{3.5}$$

The temperature precision for physical density-based thermometry (Equation 3.3) was calculated as follows:

$$\delta T = \sqrt{\left(\frac{1}{\alpha\, \rho(T)}\delta\rho(T_0)\right)^2 + \left(-\frac{\rho(T_0)}{\alpha\, \rho(T)^2}\delta\rho(T)\right)^2 + \left(\frac{1}{\alpha}\delta\beta\right)^2 + \left(\left(-\frac{\rho(T_0)}{\rho(T)\, \alpha^2} + \frac{\beta}{\alpha^2}\right)\delta\alpha\right)^2} \tag{3.6}$$

Because a high standard deviation in CT images can be attributed to both high noise levels or severe metal artefacts, the placement of the ROI was varied to identify the true source of uncertainty. First, to determine the temperature precision at varying distances from the ablation antenna, rectangular ROIs of 2 by 2 mm were placed at 10, 15, 20, and 25 mm from the ablation antenna. These ROIs were placed such that the influence of metal artifacts was minimized. The measurement uncertainty in these ROIs was defined as the standard error of the mean (standard deviation divided by the square root of the number of voxels in the ROI).

Alternatively, to evaluate the effect of metal artifacts on temperature precision, two additional circular ROIs with a radius of 6 mm were placed—one in line with the ablation antenna and another lateral of the ablation antenna, within the slices most affected by metal artifacts (Figure 3.5). The measurement uncertainty in these artifact-corrupted ROIs was defined as the standard deviation divided in the ROI.

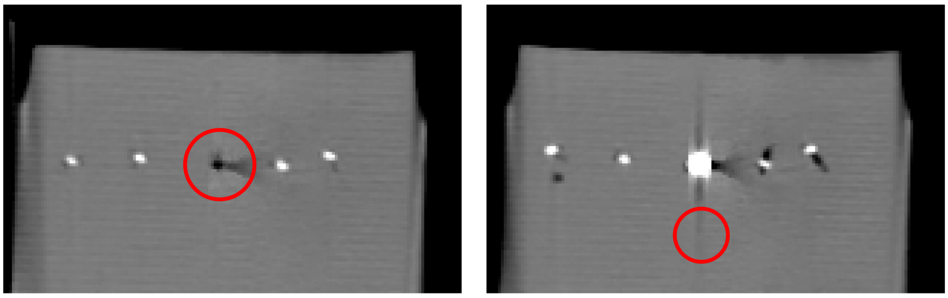

(a) Region of interest placed in line with ablation antenna, which is oriented orthogonal to the paper.

(b) Region of interest placed lateral to the ablation antenna, which is oriented orthogonal to the paper.

Figure 3.5: Placement of regions of interest in slices that contained severe metal artifacts. The standard deviation within these regions were used to calculate the temperature precision. Small white dots are the temperature sensors. Small white dots represent the temperature sensors. Note that the ablation antenna is absent in slice (a) but visible in slice (b).

To assess the precision of CT thermometry under diverse acquisition and reconstruction settings, the temperature precision was calculated across different combinations of MAR techniques, slice thicknesses, and radiation doses. The outcomes of these calculations are visually represented in a heatmap format, with each segment illustrating a specific combination of radiation dose and slice thickness. This visual approach facilitates the identification of the optimal combination of radiation dose, slice thickness, and MAR algorithm necessary to achieve clinically relevant temperature precision.

To examine the impact of increasing either the dose or slice thickness on precision, a paired t-test was utilized. Additionally, the efficacy of different MAR techniques under varying imaging conditions was compared. Given the paired nature of the data, an initial Shapiro-Wilk test was conducted to evaluate the normality of the dataset. The results revealed a non-normal distribution, leading to the use of non-parametric statistical methods for subsequent analysis.

In comparing the effectiveness of these MAR methods, the Wilcoxon signed-rank test was applied for pairwise comparisons. Each MAR method was compared against the others to assess the significance of differences in performance across all considered imaging conditions. The reduction of metal artifacts in physical density maps was quantified as the percentage decrease in temperature precision of the physical density map relative to attenuation images. Similarly, the effectiveness of different MAR algorithms was measured by the percentage decrease in temperature precision of the MAR method compared to when no MAR was applied.

3.3.3. Accuracy

In this study, two CT thermometry models were developed based on the three repetitions with a high dose. The model's accuracy was subsequently evaluated using the single repetition that was not incorporated into the model development, specifically the low dose repetition. For this, temperature maps for the low dose repetition were generated using the model parameters from 3.2.4. The modeled temperatures in proximity to the temperature sensors were recorded by employing ROI measurements as detailed in section 3.2.3. To assess the accuracy of modeled temperatures, a Bland-Altman analysis was made. This analysis provided the mean-of-difference between the temperature as measured by the thermocouples and modeled temperatures. Moreover, the 96% limits-of-agreement, calculated as 1.969 × standard deviation of differences, were established. The Bland-Altman plot graphically presents the difference between measured and modeled temperatures against the average of these temperatures.

3.4. Image quality assessment

Image quality of different MAR methods and of attenuation and physical density maps were assessed in a homogeneous slice of one repetition in the gel phantom. Only metrics related to image noise were utilized because the assessment of image contrast was not possible due to the homogeneity of the gel phantom. To evaluate image noise, the standard deviation of the mean CT value (HU or physical density) within 9 ROIs, each 10 × 10 mm and arranged radially, was computed in a slice without metal artifacts (Figure 3.6). The signal-to-noise ratio was defined as the mean CT value divided by the noise. Subsequently, the 2D noise power spectrum (NPS) and 1D normalized NPS were computed to further characterize image noise texture. The calculation of the NPS adhered to the method established by the ICRU as described below [60].

While the autocorrelation function describes noise correlation in the spatial domain, the NPS describes noise correlation in the Fourier domain. Considering a two-dimensional ROI, suppose $I_i(x,y)$ denotes the signal in the i^{th} ROI and $\bar{I}$ represents the average of $I_i(x,y)$. The calculation of the 2D NPS then proceeds as follows:

$$NPS_{2D}(f_x,f_y) = \frac{1}{N}\sum_{i=1}^{N} |DFT_{2D}[I_i(x,y)-\bar{I}]|^2 \frac{\Delta_x \Delta_y}{N_x N_y} \tag{3.7}$$

Here, the summation across i denotes the mean of the NPS values across N ROIs. The Δ values represent the pixel size within a specified slice. N_x and N_y are the voxel counts across each dimension of the ROI. The variables f_x and f_y represent the spatial frequencies in the x and y directions, respectively, while DFT_{2D} is the two-dimensional discrete Fourier transform.

The 1D NPS was derived from the 2D NPS via radial averaging. This was done by summing and averaging the noise power values along multiple radial lines extending from the center of the 2D NPS. This process transforms the 2D NPS into a 1D representation, providing a more comprehensive characterization of noise texture. The resulting 1D NPS was normalized by dividing the noise power at each frequency by the total noise power. The NPS analysis was performed in the same 9 ROIs from Figure 3.6.

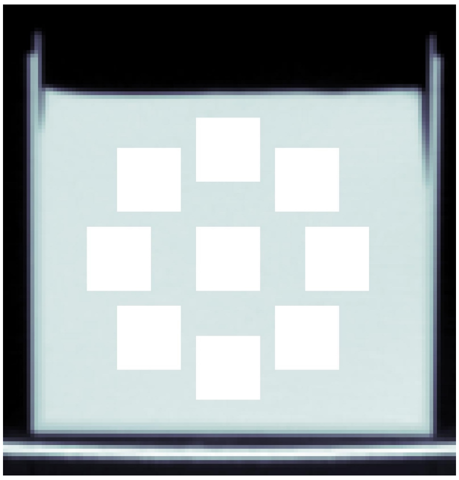

Figure 3.6: Region of interest placement for image quality assessment. Nine radially dispersed square (10 x 10 mm) regions of interest were placed in a homogeneous slice of the gel phantom that did not contain metal artifacts. Standard deviation, signal-to-noise ratio and the noise power spectrum were calculated in these regions.

4

Results

4.1. AM-PD reparameterization

The reparameterization of the AM-PD model demonstrated minimal variance in root mean square error across different energy levels (50 - 200 keV), with values spanning from 0.00283 to 0.00317 g/mL. The highest discrepancy observed, a maximum absolute error of 0.49 g/mL, was found in materials of greater density, such as breast calcifications and cortical bone. Conversely, in the middle density range, with tissues such as soft tissue, blood, and fat, the maximum absolute error was lowest, remaining under 0.01 g/mL. Increased error margins were again observed in lower-density regions, specifically in lung tissues (Figure 4.1). Nonetheless, the phantom materials used in this study predominantly fell within the mid-density range, ensuring that the absolute error for these materials did not exceed the 0.01 g/mL threshold. Model parameters and RMSE for x-ray energy levels of 70, 110, and 150 keV are shown in Table 4.1.

	X-ray energy		
	70 keV	110 keV	150 keV
p_1	3.5699	3.7651	3.6723
p_2	1.0761	1.0804	1.0816
p_3	44.2394	45.7486	42.6138
p_4	4.4857	5.3714	6.8218
p_5	3.1221	3.6567	4.4194
p_6	1.0303	1.0551	1.0436
p_7	1.0064	1.0869	1.1679
RMSE (g/mL)	0.00290	0.00290	0.00300

Table 4.1: Parameters of three AM-PD models at x-ray energy levels of 70, 110, and 150 keV. This table illustrates the variation in fitted parameters between each model, alongside their consistently similar root mean square error (RMSE) values. This demonstrates the model's uniform performance across diverse energy spectra.

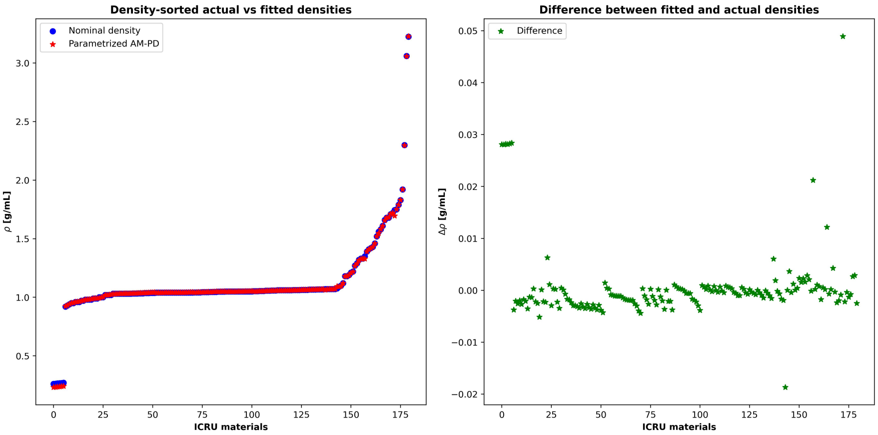

Figure 4.1: Left: Comparison of nominal densities with those predicted by the parameterized AM-PD model with an energy level of 150 keV. ICRU materials were sorted on increasing density. Right: Difference in density values between the nominal and fitted densities. The fitted densities deviate most from the nominal densities in the lower and higher density regions.

4.2. Liver phantom

The temperature in the livers rose from 9 to 150°C measured by the closest thermocouple. Other thermocouples recorded lower maximum temperatures. Figure 4.2 shows the CT and physical density images of the reference scan (before ablation) and after 60, 150, and 360 seconds of ablation.

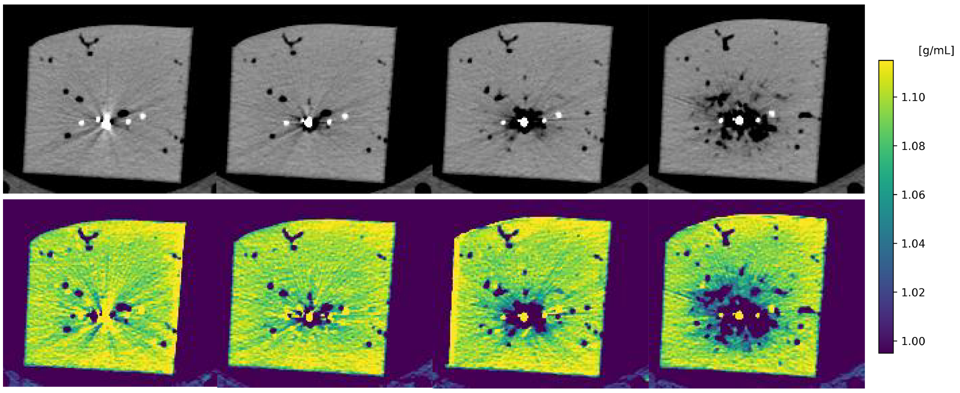

Figure 4.2: Example of CT and physical density images in the liver phantom before ablation and after 60, 150 and 360 seconds of ablation. The images show a hypodense area around the ablation antenna. Metal artifacts from the ablation antenna obscure both proximal and distal surrounding tissue. Setting for window/level were 400/60 and 0.12/1.055 for the CT images and physical density maps, respectively.

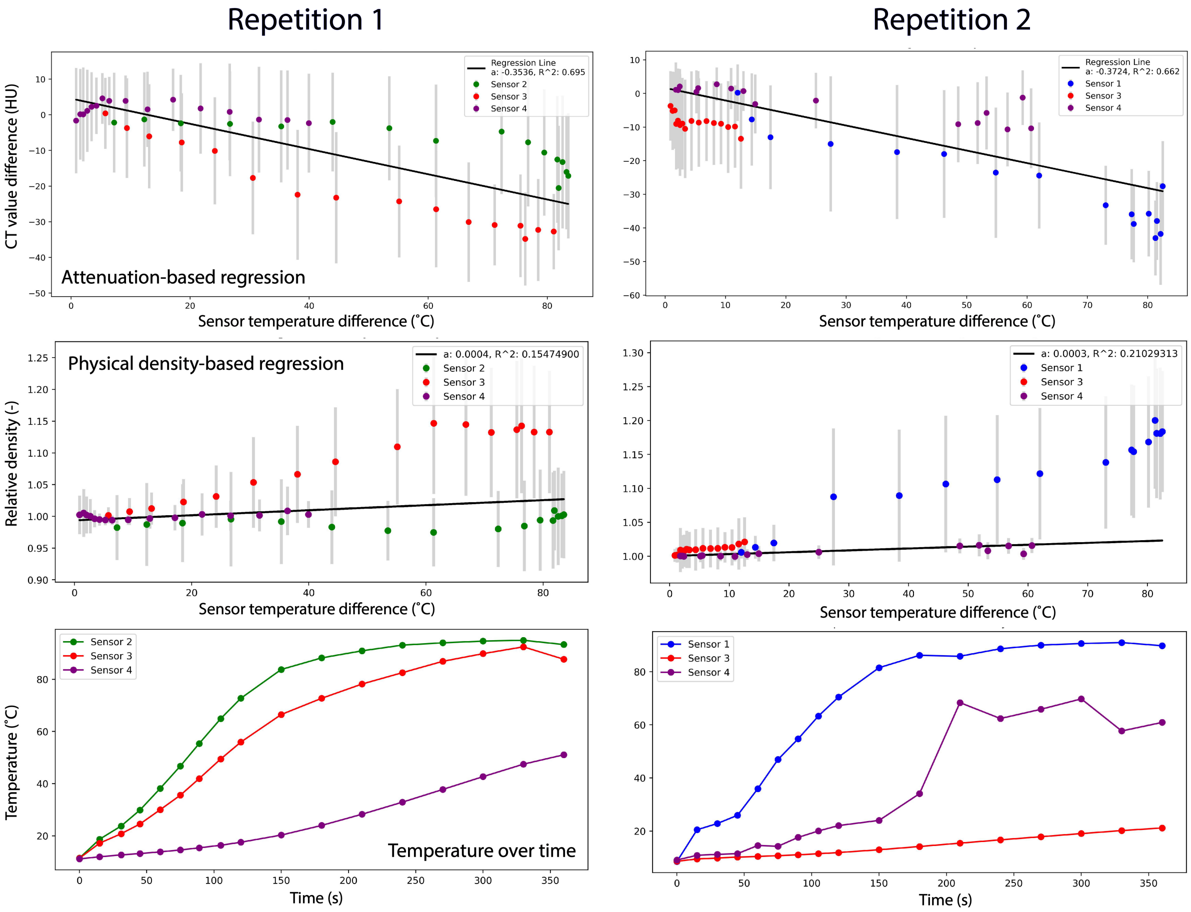

Figure 4.3: Assessment of reproducibility in attenuation-based (top) and physical density-based (middle) CT thermometry from 9 to 150 ºC (bottom) over two repetitions.

4.2.1. Thermometry reproducibility

In the analysis of attenuation-based images of liver phantoms, a mildly inverse correlation between HU difference and temperature difference was found in two separate test repetitions (Figure 4.3, top row). The thermal sensitivity (a) averaged -0.36 ± 0.013 HU/ºC, while the intercept (b) was 3.1 ± 2.1 HU. These values led to a CV of 0.037 for a and 0.66 for b, indicating a relatively high reproducibility in attenuation-based CT thermometry for this experiment. However, the linear relationship between HU difference and temperature difference was weak with a mean R^2 value of 0.68 across the two repetitions.

In a similar vein, physical density images in the liver phantoms showed an even weaker linear relationship between relative density change ($\rho(T_0)/\rho(T)$) and temperature difference ($\Delta T = T - T_0$) (Figure 4.3, middle row). The measured thermal expansion coefficient (α) was 0.00034 ± 0.000087 ºC^{-1} and the intercept (β) 0.99 ± 0.0047. These results, with a CV of 0.26 for α and 0.047 for β, reflect the challenges in the reproducibilty of physical density-based CT thermometry in this experiment. A mean R^2 value of 0.18 was found across the two repetitions.

4.2.2. Temperature precision

The evaluation of temperature precision in the liver phantom was conducted without the use of O-MAR or DL-MAR. Temperature precision improved through attenuation-based thermometry, thicker slices, and greater distances from the ablation antenna as visualized in a heatmap. Near the ablation antenna, attenuation-based thermometry yielded more favorable results than thermometry based on physical density. The temperature precision did not change with the use of high energy VMI for the physical density maps.

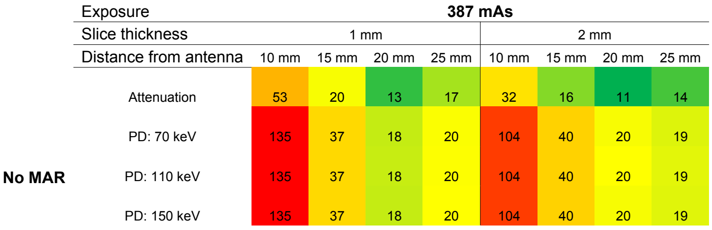

	Exposure	387 mAs							
	Slice thickness	1 mm				2 mm			
	Distance from antenna	10 mm	15 mm	20 mm	25 mm	10 mm	15 mm	20 mm	25 mm
No MAR	Attenuation	53	20	13	17	32	16	11	14
	PD: 70 keV	135	37	18	20	104	40	20	19
	PD: 110 keV	135	37	18	20	104	40	20	19
	PD: 150 keV	135	37	18	20	104	40	20	19

Table 4.2: Temperature precision heatmap in liver phantom calculated using equations 3.5 and 3.6. Colours demonstrate a superior temperature precision differences of attenuation-based thermometry. Additionally, greater slice thickness and distance from the ablation antenna improves precision.

4.3. Gel phantom

Figure 4.4 shows the CT and physical density images of the reference scan (before ablation) and after 120, 300, and 600 seconds of ablation. The temperature range as measured by the closest thermocouple was 18 to 98ºC.

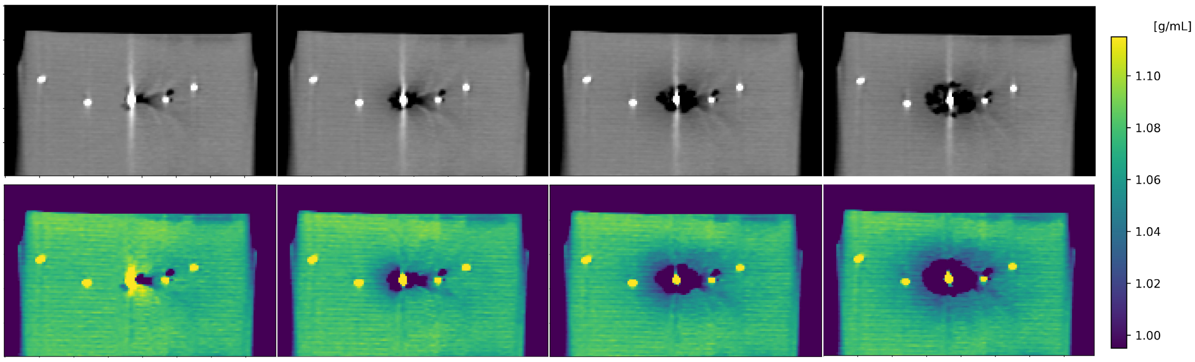

Figure 4.4: Example of CT and physical density images of the liver mimicking gel phantom before ablation and after 120, 300 and 600 seconds of ablation. The images show a hypodense area around the ablation antenna. Metal artifacts from the ablation antenna obscure both proximal and distal surrounding tissue. Setting for window/level were 400/60 and 0.12/1.055 for the CT images and physical density maps, respectively.

4.3.1. Phantom characterization

The attenuation of the liver mimicking gel phantom matched the attenuation of a human adult liver as described by the ICRU 44 and 46 [55]. At lower energies, the difference in attenuation was larger with a maximum of 8 HU, while this difference decreased to 0.5 HU at higher energies (Figure 4.5).

4.3.2. Thermometry reproducibility

In the analysis of attenuation-based images of gel phantoms, a strong inverse correlation between HU change ($\Delta HU = HU(T) - HU(T_0)$ and temperature difference ($\Delta T = T - T_0$) was found across the three separate test repetitions (Figure 4.6, top row). The thermal sensitivity (a) averaged -0.38 ± 0.0088 HU/ºC, while the intercept (b) was 0.31 ± 0.47 HU. These values led to a CV of 0.023 for a and 1.53 for b, indicating a high reproducibility in attenuation-based CT thermometry for this experiment. Note that although the CV for intercept b is very high, the standard deviation of 0.47 HU is still very small. The high mean R^2 value over three repetitions of 0.98 ± 0.0054 demonstrated the strong linear relationship between HU change and temperature difference.

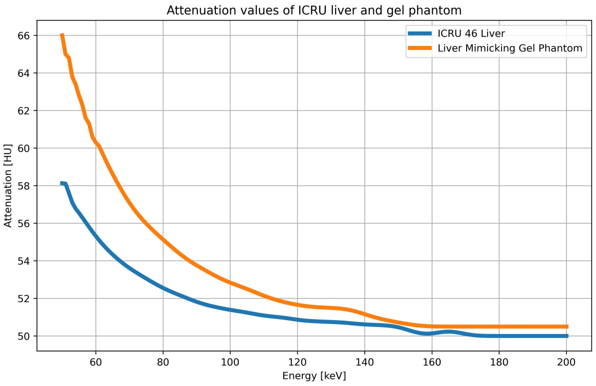

Figure 4.5: Attenuation values of ICRU 46 liver and the liver mimicking gel phantom at different energy levels. Differences in attenuation decreased with increasing energy levels.

In a similar vein, physical density images in the gel phantoms showed a comparable but direct relationship between relative density change ($\rho(T_0)/\rho(T)$) and temperature difference (Figure 4.6, middle row). The measured thermal expansion coefficient (α) was 0.00039 ± 0.000026 ºC^{-1} and the intercept (β) 0.99 ± 0.00054. These results, with a CV of 0.067 for α and 0.0005 for β, similarly reflect the high reproducibility of the CT thermometry in this experiment. The high mean R^2 value over three repetitions of 0.96 ± 0.019 demonstrated the strong linear relationship between relative physical density and temperature difference, recapitulating thermal volumetric expansion.

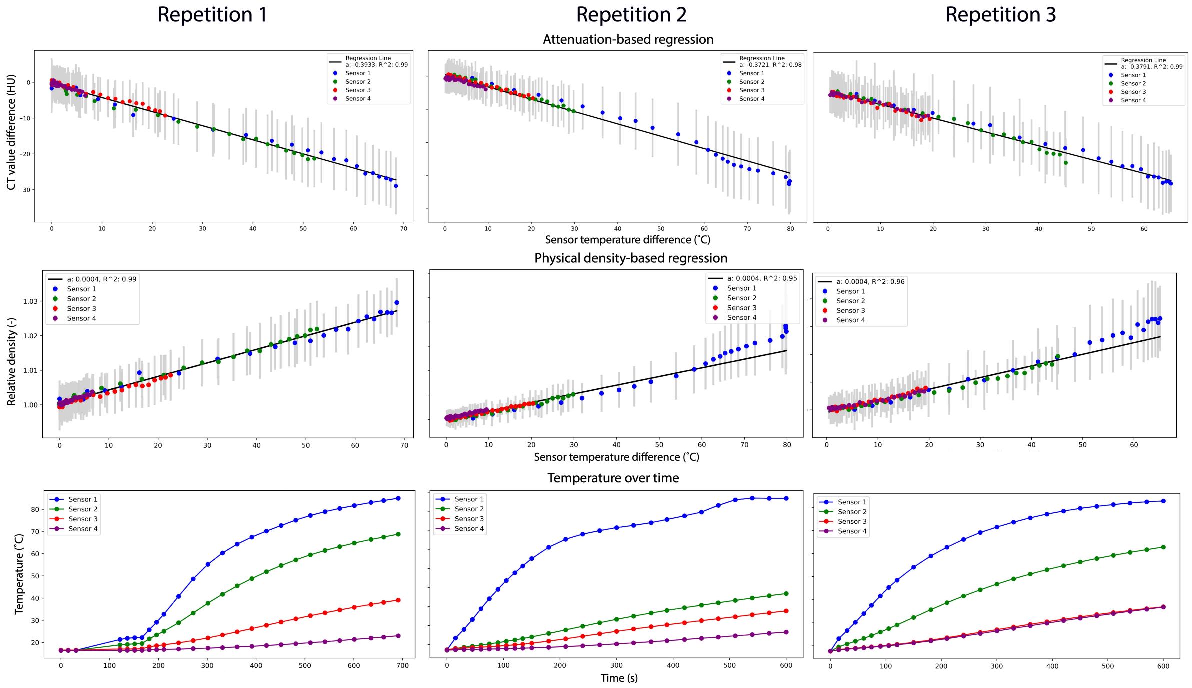

Figure 4.6: Reproducibility results from the experiments on the liver mimicking gel phantom. Weighted linear regression was performed on three repetitions to determine the parameters for the attenuation-based (top) and physical density-based (middle) thermometry models. Physical density-based CT thermometry was applied on physical density maps generated at 70 keV. The maximum temperature difference as measured by the thermocouples was 80 ºC.

4.3.3. Temperature precision

In the temperature precision analysis using equations 3.5 and 3.6, an improved temperature precision was observed with an increase in both distance from the ablation antenna and slice thickness, across all MAR methods, as shown in the heatmap (Table 4.3). Attenuation-based thermometry provided better precision close to the ablation antenna compared to physical density-based thermometry, but this advantage decreased as the distance from the antenna increased. In absence of metal artifacts, a constant level of precision was observed when using higher energy VMI for physical density-based thermometry (p>0.999).

Under the high dose and thin slice condition, the implementation of DL-MAR significantly improved temperature precision, showing a substantial decrease in temperature precision compared to when DL-MAR was not used (3.0 vs. 5.5, p<0.001), with a median difference of 2.7ºC. The use of O-MAR slightly improved precision compared to not using MAR (5.4 vs. 5.5, p=0.003). The combination of O-MAR and DL-MAR also improved temperature precision compared to no MAR (3.0 vs. 5.5, p<0.001).

Temperature precision was better in low dose (75 mAs) settings compared to high dose (150 mAs) settings (3.6 vs. 4.0, p<0.001). Increasing the slice thickness from 1 to 2 mm significantly improved temperature precision (4.6 vs. 5.5, p<0.001). When DL-MAR was applied, the precision difference between thin and thick slices decreased to 0.1ºC (3.0 vs. 2.9, p=0.03) The findings indicate that to achieve clinically acceptable temperature precision of 2ºC, a minimum distance of 20 mm from the ablation antenna is required when using DL-MAR with a slice thickness of 1 mm.

	Exposure	150 mAs								75 mAs							
	Slice thickness	1 mm				2 mm				1 mm				2 mm			
	Distance from antenna	10 mm	15 mm	20 mm	25 mm	10 mm	15 mm	20 mm	25 mm	10 mm	15 mm	20 mm	25 mm	10 mm	15 mm	20 mm	25 mm
No MAR	Attenuation	6.1	5.2	5.1	5.2	5.2	3.7	3.4	4.1	8.1	4.8	5.2	4.0	5.1	3.9	4.1	3.2
	PD: 70 keV	7.4	4.9	5.0	4.6	7.4	4.2	3.5	3.7	8.8	4.1	4.1	3.8	7.1	3.8	3.3	2.6
	PD: 90 keV	7.3	4.8	4.9	4.7	7.3	4.1	3.5	3.7	8.7	4.1	4.1	3.9	7.1	3.8	3.3	2.6
	PD: 110 keV	7.4	4.8	4.9	4.7	7.4	4.1	3.5	3.8	8.8	4.1	4.1	3.9	7.1	3.8	3.3	2.6
	PD: 130 keV	7.4	4.9	5.1	4.6	7.4	4.1	3.5	3.7	8.7	4.0	4.2	3.9	7.0	3.7	3.3	2.6
	PD: 150 keV	7.6	5.0	4.9	4.5	7.5	4.2	3.5	3.7	9.0	4.2	4.1	3.9	7.1	3.8	3.3	2.6
O-MAR	Attenuation	6.1	5.2	5.1	5.2	5.2	3.7	3.4	4.1								
	PD: 70 keV	7.2	4.8	5.0	4.6	7.2	4.1	3.5	3.7								
	PD: 90 keV	7.2	4.7	4.9	4.7	7.2	4.0	3.5	3.7								
	PD: 110 keV	7.2	4.8	4.9	4.7	7.2	4.0	3.5	3.7								
	PD: 130 keV	7.2	4.8	5.1	4.6	7.3	4.0	3.5	3.7								
	PD: 150 keV	7.4	4.9	4.9	4.5	7.3	4.1	3.5	3.6								
DL-MAR	Attenuation	2.8	1.8	1.5	2.0	2.9	1.9	1.4	1.4	3.2	1.7	1.5	1.5	2.0	1.7	1.5	1.4
	PD: 70 keV	5.8	3.1	2.3	1.8	5.6	3.3	2.2	1.7	5.3	3.1	2.0	1.6	4.0	3.1	1.8	1.6
	PD: 90 keV	5.7	3.1	2.2	1.7	5.4	3.2	2.1	1.7	5.2	3.0	1.8	1.6	3.8	3.0	1.7	1.7
	PD: 110 keV	5.6	3.2	2.2	1.7	5.3	3.2	2.2	1.7	5.1	3.0	1.8	1.6	3.7	3.0	1.8	1.6
	PD: 130 keV	5.6	3.2	2.2	1.7	5.4	3.2	2.2	1.7	5.0	2.9	1.8	1.6	3.6	2.9	1.8	1.7
	PD: 150 keV	5.7	3.3	2.3	1.7	5.5	3.3	2.1	1.8	5.1	3.0	1.8	1.6	3.6	3.0	1.9	1.7
O-MAR + DL-MAR	Attenuation	2.8	1.8	1.5	2.0	2.9	1.9	1.4	1.4								
	PD: 70 keV	5.8	3.0	2.3	1.8	5.6	3.3	2.2	1.7								
	PD: 90 keV	5.7	3.1	2.2	1.7	5.4	3.2	2.1	1.7								
	PD: 110 keV	5.6	3.2	2.2	1.7	5.4	3.2	2.2	1.7								
	PD: 130 keV	5.6	3.2	2.2	1.7	5.4	3.2	2.2	1.7								
	PD: 150 keV	5.7	3.3	2.3	1.7	5.4	3.3	2.1	1.8								

Table 4.3: Temperature precision heatmap calculated using equations 3.5 and 3.6. This metric quantifies the degree of uncertainty in ΔT attributable to uncertainties within the inputs of the thermometry model. Green colors demonstrate a superior temperature precision of attenuation-based thermometry and the use of DL-MAR. Additionally, greater slice thickness and distance from the ablation antenna improves precision. A clinically required level of precision was found from 20 mm from the ablation antenna when using DL-MAR and 1 mm slice thickness.

4.3.4. Needle artifact reduction

The temperature precision in artifact-corrupted slices was evaluated using ROI measurements from Figure 3.5 and equations 3.5 and 3.6. In the assessment of efficacy of physical density maps in reducing needle artifacts in CT scans at a 1 mm slice thickness and a 150 mAs setting, the Wilcoxon signed-rank test indicated significant differences with attenuation maps. These differences were most notable when comparing attenuation maps to physical density maps at varying energy levels. A clear decrease in needle artifacts was observed with the use of higher energy physical density maps for artifacts in line with the ablation antenna, though this trend was less pronounced for lateral artifacts (Figure 4.7). Pairwise comparisons revealed that physical density maps at 70 keV did not significantly reduce needle artifacts compared to attenuation maps. However, at higher energy levels, the reduction of needle artifacts became more substantial. Specifically, physical density maps at 90 keV reduced needle artifacts by an average of 53% (95% CI, 11% - 96%) compared to attenuation maps, with a median difference of 104°C (p<0.05). At 110 keV, the reduction was 66% (95% CI, 47% - 84%) on average, with a median difference of 129°C (p<0.05). At 130 keV, the average reduction reached 71% (95% CI, 60% - 81%), with a median difference of 127°C (p<0.05), and at 150 keV, there was a 73% (95% CI, 61% - 84%) average reduction, with a median difference of 125°C (p<0.05).

Further analysis on the effectiveness of MAR techniques at the same settings showed that the Wilcoxon signed-rank test revealed notable differences between having no MAR approach and applying various MAR techniques. O-MAR reduced needle artifacts on average by 49% compared to no MAR, with a median difference of 72°C (p=0.001). DL-MAR showed a 12% average reduction, with a median difference of 37°C (p=0.01). The combined use of O-MAR and DL-MAR further reduced needle artifacts to 60% on average, with a median difference of 119°C (p=0.001).

Adjustments to the scan parameters also influenced metal artifact reduction. Specifically, doubling the slice thickness led to a 6.1% reduction in metal artifacts, with a mean difference of 9°C (p<0.001). Increasing the exposure doubled the reduction effect to 29%, with a mean difference of 162°C (p=0.003). This evaluation illustrates the effectiveness of physical density maps and MAR techniques in the context of thermal ablation.

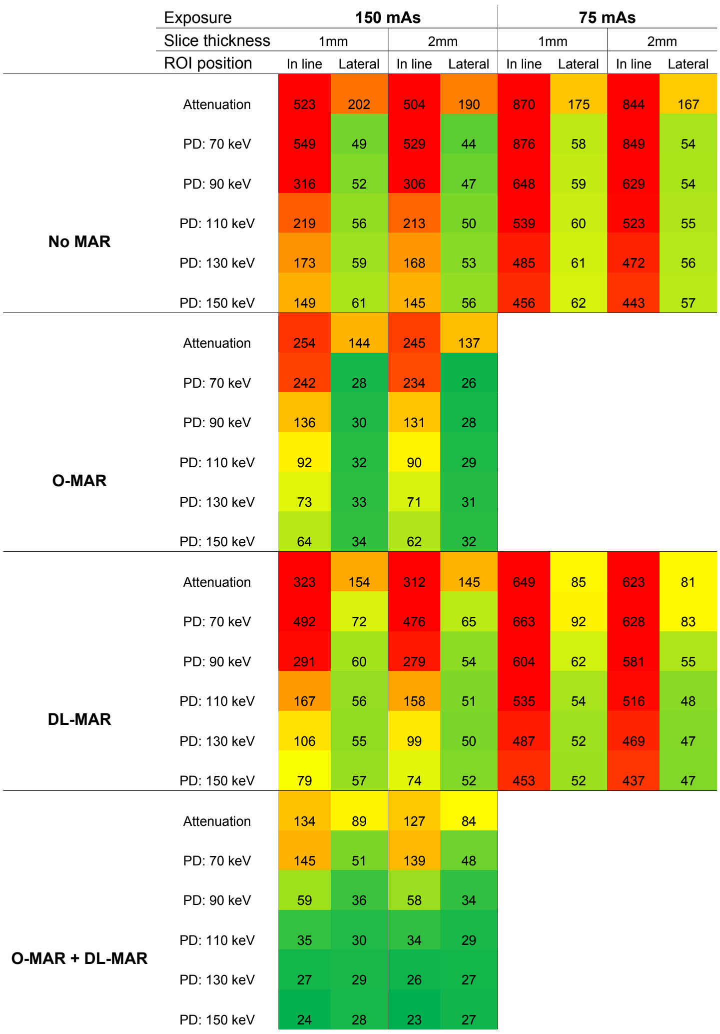

	Exposure	150 mAs				75 mAs			
	Slice thickness	1mm		2mm		1mm		2mm	
	ROI position	In line	Lateral	In line	Lateral	In line	Lateral	In line	Lateral
No MAR	Attenuation	523	202	504	190	870	175	844	167
	PD: 70 keV	549	49	529	44	876	58	849	54
	PD: 90 keV	316	52	306	47	648	59	629	54
	PD: 110 keV	219	56	213	50	539	60	523	55
	PD: 130 keV	173	59	168	53	485	61	472	56
	PD: 150 keV	149	61	145	56	456	62	443	57
O-MAR	Attenuation	254	144	245	137				
	PD: 70 keV	242	28	234	26				
	PD: 90 keV	136	30	131	28				
	PD: 110 keV	92	32	90	29				
	PD: 130 keV	73	33	71	31				
	PD: 150 keV	64	34	62	32				
DL-MAR	Attenuation	323	154	312	145	649	85	623	81
	PD: 70 keV	492	72	476	65	663	92	628	83
	PD: 90 keV	291	60	279	54	604	62	581	55
	PD: 110 keV	167	56	158	51	535	54	516	48
	PD: 130 keV	106	55	99	50	487	52	469	47
	PD: 150 keV	79	57	74	52	453	52	437	47
O-MAR + DL-MAR	Attenuation	134	89	127	84				
	PD: 70 keV	145	51	139	48				
	PD: 90 keV	59	36	58	34				
	PD: 110 keV	35	30	34	29				
	PD: 130 keV	27	29	26	27				
	PD: 150 keV	24	28	23	27				

Table 4.4: Heatmap of temperature precision, calculated using equations 3.5 and 3.6 in presence of needle artifacts. Temperature precision quantifies the degree of uncertainty in ΔT attributable to uncertainties within the inputs of the thermometry model. Green colors indicate the enhanced effectiveness of high-energy physical density maps, O-MAR, DL-MAR, and their combination in reducing needle artifacts. Artifact measurements are conducted both inline and laterally to the ablation antenna.

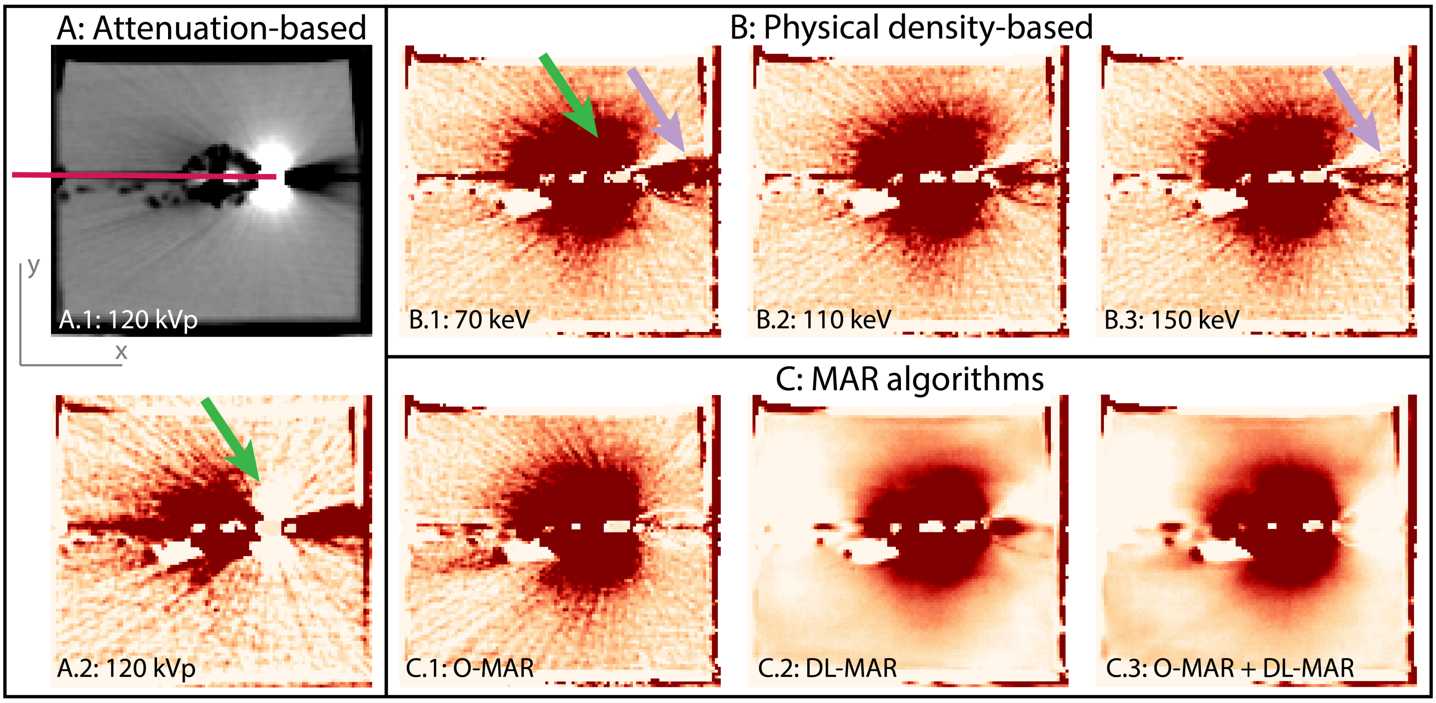

Figure 4.7: The effect of various MAR methods on temperature maps after a 10-minute ablation procedure is illustrated. In panel **A.1**, the ablation antenna's trajectory is depicted as a pink line on an 120 kVp attenuation map (window/level = 400/60 HU). Panel **A.2** shows the application of attenuation-based thermometry (window/level = 80/50ºC), which led to significant artifacts laterally to (green arrow) and in line with the antenna. Panels **B.1** through **B.3** demonstrate the use of physical density-based thermometry with VMIs at energies of 70, 110, and 150 keV, respectively. This approach resulted in fewer artifacts laterally to the antenna (green arrow in **B.1**). Increasing VMI energy levels progressively reduced artifacts in line with the antenna (purple arrows in **B.1** and **B.3**). In panel **C**, O-MAR, DL-MAR, and their combination were applied to 150 keV physical density-based thermometry. The use of O-MAR **(C.1)** significantly reduced overall artifact presence compared to no MAR **(B.3)**. Applying DL-MAR in **C.2** substantially reduced image noise and slightly decreased artifacts both laterally and along the antenna. The most effective strategy for reducing metal artifacts, shown in **C.3**, involves applying both O-MAR and DL-MAR to 150 keV physical density maps.

4.3.5. Accuracy

Using attenuation-based thermometry, the Bland-Altman analysis shows a mean-of-difference of -1.2°C with limits of agreement of -7.7°C and 5.3°C. A high agreement was observed at lower temperatures, while this agreement was weaker at increasing temperatures (Figure 4.8 top). In the Bland-Altman analysis using physical density-based thermometry a mean-of-difference of -0.7°C with limits of agreement of -9.47°C and 8.05°C was found (Figure 4.8 bottom).

When analyzing temperature differences up to a clinically relevant maximum of 40°C using Bland-Altman analysis, the results for attenuation-based thermometry and physical density-based thermometry show a better agreement than the full temperature range. Attenuation-based thermometry yielded a mean-of-difference of -0.2°C, with limits of agreement ranging from -5.0°C to 4.6°C (Figure 4.9 top). In contrast, physical density-based thermometry demonstrated a mean-of-difference of 0.7°C, with a range of agreement from -4.5°C to 6.0°C (Figure 4.9 bottom).

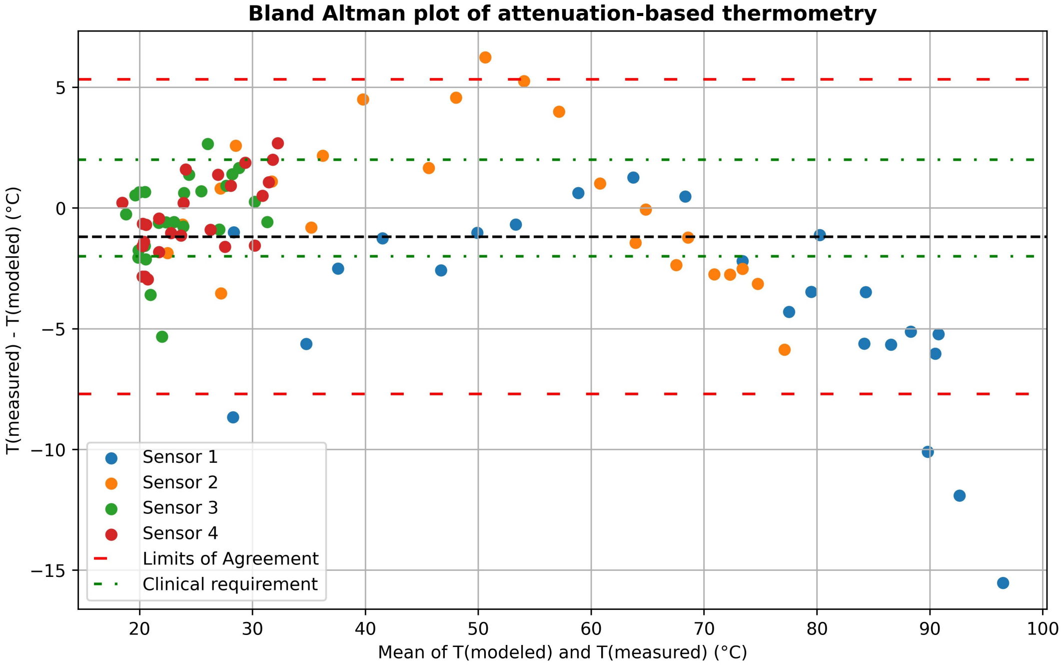

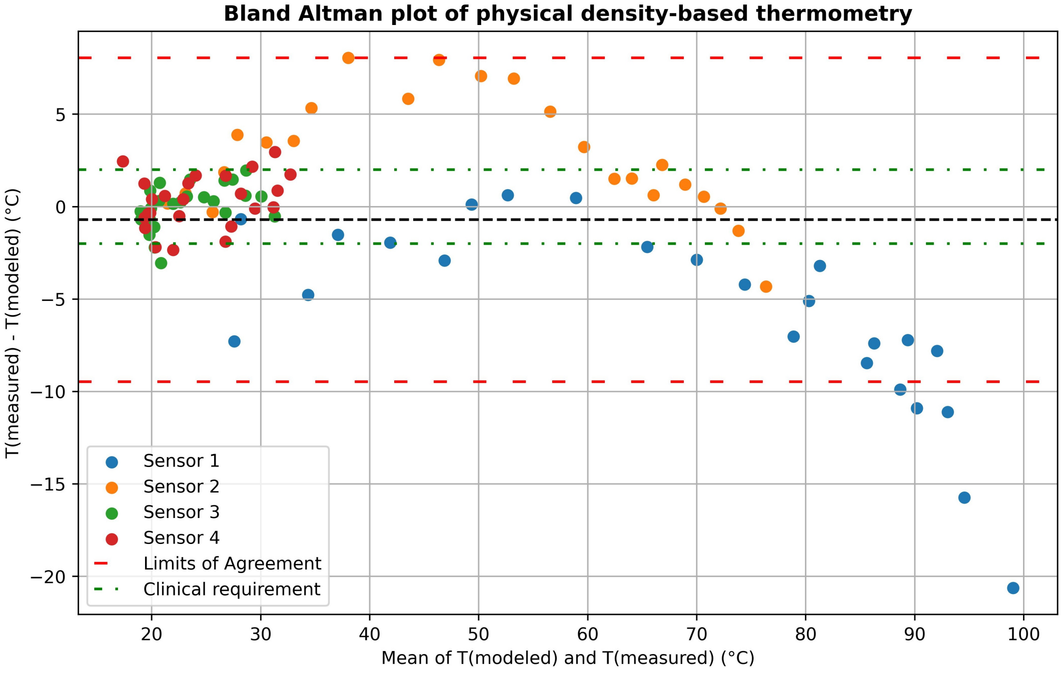

Figure 4.8: Comparative Bland-Altman plots for attenuation (top) and physical density-based CT thermometry at 150 keV (bottom). The plots display the difference between measured and modeled temperatures on the y-axis against the mean of the two temperatures on the x-axis. Limits of agreement are marked by the dashed red lines, while the clinical requirement threshold is indicated by the dashed green line. In both thermometry methods a high agreement is observed at low temperatures while this agreement decreases with increasing temperature. The reduced agreement at high temperatures could be due to more presence of metal artifacts, as Sensor 1 was positioned closest to the ablation antenna.

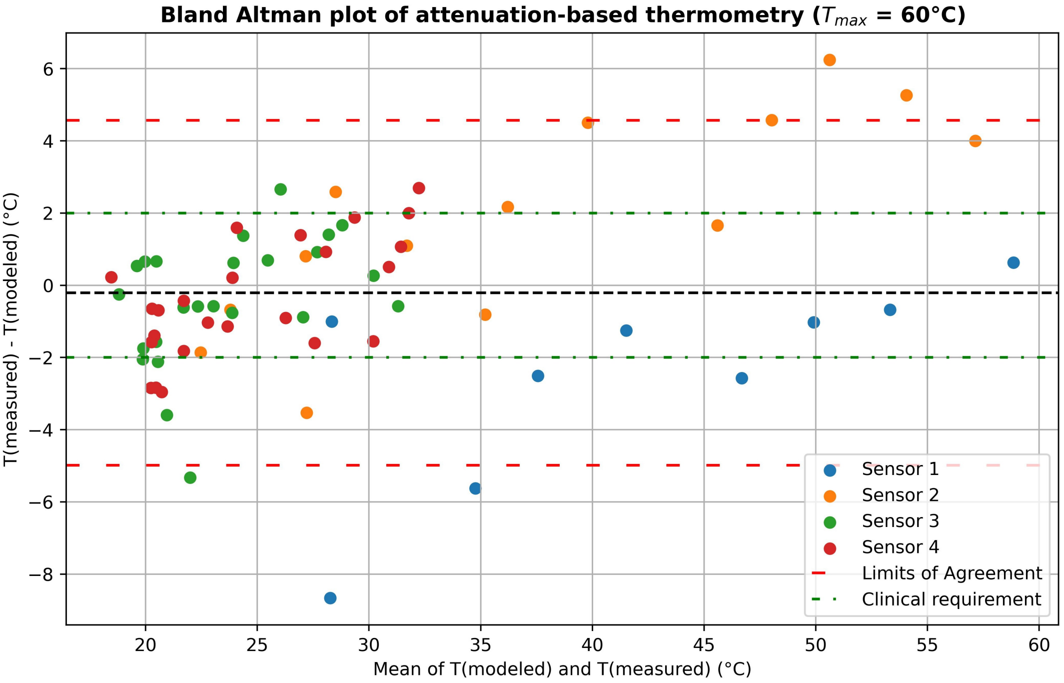

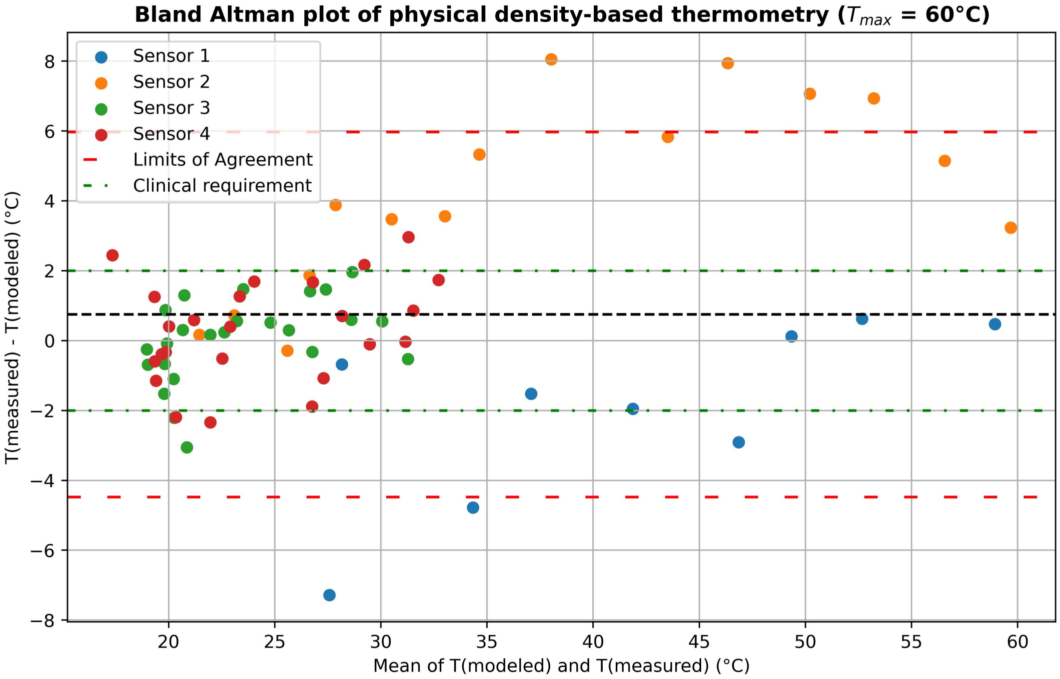

Figure 4.9: Comparative Bland-Altman plots for attenuation (top) and physical density-based CT thermometry at 150 keV (bottom) with a maximum temperature of 60°C. The plots displays the difference between measured and modeled temperatures on the y-axis against the mean of the two temperatures on the x-axis. Limits of agreement are marked by the dashed red lines, while the clinical requirement threshold is indicated by the dashed green line. In both thermometry methods a high agreement is observed in this clinically relevant situation where the maximum temperature difference was 40°C.

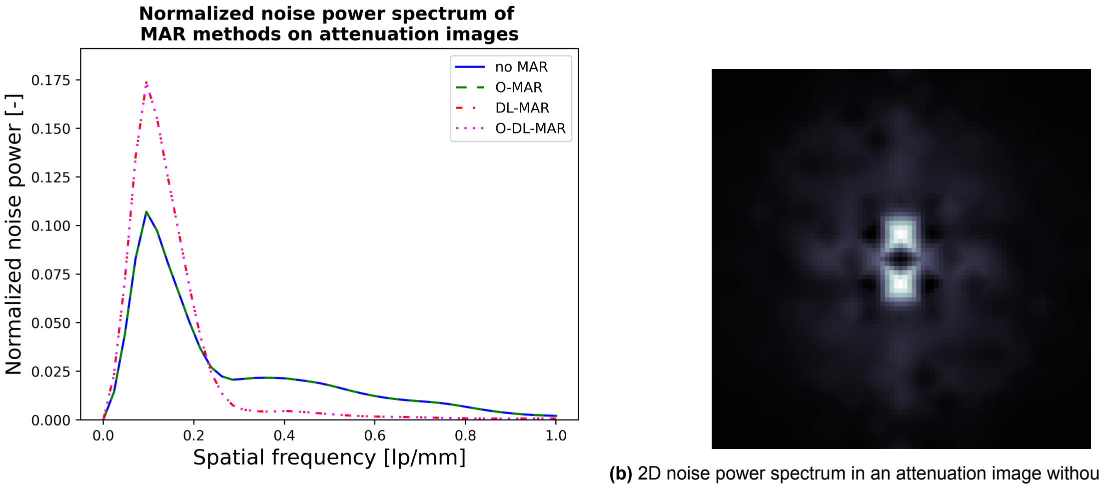

(a) The use of DL-MAR shifts high-frequency noise to the low-frequency noise peak in attenuation maps. Overlapping NPS plots suggest no difference in noise texture.

(b) 2D noise power spectrum in an attenuation image without MAR. The central peak and surrounding distribution visible in the 2D noise spectrum indicates an anisotropic noise pattern, with a notable low-frequency noise peak in the y-direction.

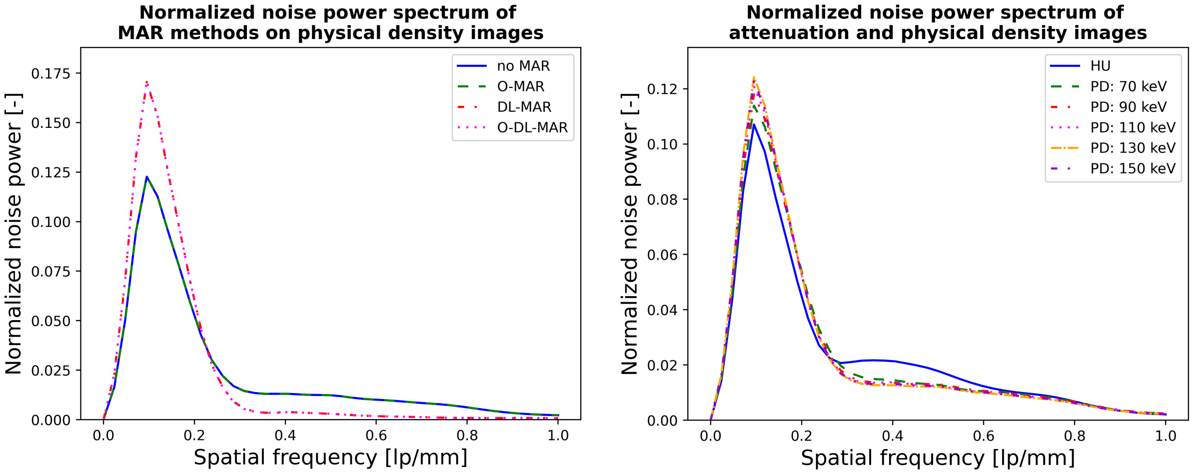

(c) The use of DL-MAR shifts high-frequency noise to the low-frequency noise peak in physical density maps. Overlapping NPS plots suggest no difference in noise texture.

(d) The normalized noise power spectrum shows that by using physical density maps, the low-frequency noise will increase at the cost of high-frequency noise.

Figure 4.10

4.4. Image quality assessment

Table 4.5 presents the measured outcomes related to image noise magnitude. When DL-MAR was applied, both HU and physical density images had decreased noise levels, leading to an improved SNR. No significant changes in noise levels were observed with the use of O-MAR. The SNR for physical density images significantly exceeded that of HU images, with a more than tenfold increase observed.

Although DL-MAR and physical density images enhance SNR, they also both alter the frequency distribution of noise, as shown in Figure 4.10. Specifically, there was a relative increase in noise power at lower frequencies, with a corresponding decrease in high-frequency noise. The texture of the noise remained unchanged with the application of O-MAR. Note that the 1D NPS curves are normalized, meaning the heights of the curves are not assigned absolute numerical values. The 2D noise spectrum indicates an anisotropic noise pattern, characterized by a peak in low-frequency noise in the y-direction.

	Noise	SNR
No MAR **(a)**	4.99 HU	11.2
O-MAR **(a)**	4.99 HU	11.2
DL-MAR **(a)**	4.2 HU	13.4
O-DL-MAR **(a)**	4.2 HU	13.4
No MAR **(c)**	0.00555 g/mL	188
O-MAR **(c)**	0.00555 g/mL	188
DL-MAR **(c)**	0.00516 g/mL	202
O-DL-MAR **(c)**	0.00516 g/mL	202
HU **(d)**	4.99 HU	11.2
PD: 70 keV **(d)**	0.00540 g/mL	196
PD: 90 keV **(d)**	0.00542 g/mL	194
PD: 110 keV **(d)**	0.00548 g/mL	191
PD: 130 keV **(d)**	0.00553 g/mL	189
PD: 150 keV **(d)**	0.00555 g/mL	188

Table 4.5: Noise and signal-to-noise ratio of different MAR methods, attenuation maps, and physical density maps. The letter in **boldface** correspond to the noise power spectrum curves from Figures 4.10 **a, c, d**.

5

Discussion

The aim of this study was to assess the applicability of spectral CT for non-invasive temperature measurements in thermal liver ablation. More specifically, reproducibility, temperature precision, temperature accuracy and metal artifact reducing capabilities of spectral CT thermometry based on physical density maps were compared to attenuation-based thermometry. Additionally, a sinogram-based MAR and deep learning-based MAR algorithm were applied to further reduce artifacts from the ablation antenna.

5.1. Key findings and comparison to literature

This study demonstrated that thermal volumetric expansion during liver thermal ablation can be effectively monitored using spectral CT. We observed a strong linear correlation between tissue temperature and physical density, with a consistent variation of only 0.067 across three separate ablation procedures using a liver-mimicking gel phantom. By employing DL-MAR on physical density maps, we achieved temperature precision below the clinically required 2°C threshold. Attenuation-based thermometry reached the 2°C precision mark at a 15 mm distance from the ablation antenna. In contrast, physical density-based thermometry achieved this precision at a 25 mm distance, suggesting potential for improvement closer to the antenna. Nonetheless, this might be less relevant considering the ablation zone extended to about 20 mm within the gel phantom.

Physical density maps at 150 keV proved most effective in reducing metal artifacts from the ablation antenna, achieving an average reduction of 73%, compared to attenuation maps. Furthermore, the combined use of O-MAR and DL-MAR facilitated a 60% reduction in metal artifacts compared to no MAR. In terms of accuracy, CT thermometry using physical density maps at 150 keV showed high temperature accuracy, with limits of agreement ranging from -4.5°C to 6.0°C.

In this study, we identified a thermal sensitivity of -0.38 HU/°C in a liver-mimicking phantom using attenuation-based thermometry. This result aligns with the established range in literature, which spans from -2.00 to -0.23 HU/°C (see Appendix B). Additionally, we determined a thermal expansion coefficient (α) of 0.00039 °C^{-1} using physical density-based thermometry. This figure is slightly lower than those reported by Noël's research group, who developed the AM-PD model. They documented coefficients of 0.00042 and 0.00053 °C^{-1} for a liver-mimicking phantom and ex vivo bovine liver, respectively [31], [32]. The difference in results could be attributed to differences in heating methods: while our study employed thermal ablation, their approach involved slow heating in a warm water bath, potentially causing greater thermal expansion.

To our knowledge, this study is the first to apply equations 3.5 and 3.6 for quantifying temperature precision. Although Liu *et al.* utilized a similar metric known as temperature tolerance, direct comparisons with their results are difficult due to methodological differences [32].

A Bland-Altman analysis was performed on a set of data not previously used for determining CT thermometry parameters, revealing a mean-of-difference of 0.7 °C. Comparatively, a study by Pohlan *et al.* showed that binary logistic regression could distinguish between tissue temperatures below and above 70°C with 89.2% accuracy [27]. In another study, Hübner *et al.* evaluated the accuracy of

CT thermometry during cryoablation [61]. Using Bland-Altman analysis, they achieved thermometry accuracy within the 1-2°C requirement, but the broad limits-of-agreement (24.7°C and -22.2°C) hinder its direct clinical application.

These findings should be contrasted to the current gold standard, MR thermometry. Since the introduction of MR thermometry two decades ago, a variety of thermometry techniques have been developed [62]. While effective, interventional MRI is rarely applied due to high costs and the necessity for metal-free instruments. As CT thermometry approaches the performance of MR thermometry, CT presents an cost-effective alternative that is already integral to intervention planning and probe positioning.

In summary, applying O-MAR and DL-MAR to spectral CT and generating physical density maps at 150 keV can achieve the necessary clinical temperature precision in areas unaffected by metal artifacts, potentially reducing these artifacts by up to 93%.

5.2. Clinical implications

To ensure the effective monitoring of thermal ablation in clinical settings, the criteria from Table 1.1 for non-invasive thermometry were established. In short, a spatial resolution below 2 mm, a CT acquisition time under 30 seconds, and a temperature precision within 2°C must be met [6]. This study achieved the spatial resolution and acquisition time criteria with measures of 0.68 mm and 1 second, respectively. Although the image reconstruction and registration time was not recorded, it was well below 30 seconds. Moreover, by employing O-MAR and DL-MAR on spectral CT to generate physical density maps at 150 keV, it is possible to achieve the clinically desired temperature precision within approximately 20 mm of the ablation antenna. Liu *et al.* have previously explored denoising strategies, such as bilateral and non-local means filtering, aiming to improve temperature tolerance [28]. Although they did not use an ablation antenna in their study, they showed that applying non-local means denoising to physical density-based CT thermometry—conducted with 2 mm slices at a radiation dose of 2 mGy—could achieve a temperature precision of under 2°C.

In contrast to other imaging modalities like MRI, CT technology offers superior spatial and temporal resolution, allowing for a detailed depiction of small structures, such as vessels or small tumors, in three dimensions. However, the radiation exposure associated with CT, and in particular the additional dose associated with CT thermometry poses a potential concern in clinical applications. Standard practice for monitoring ablation success involves two contrast-enhanced scans. CT thermometry introduces at least two additional non-contrast scans to track temperature-related changes in CT values. Despite the increase in radiation exposure, it is important to weigh this against the potential for reduced local tumor recurrence rates. In their 2012 study, Pandeya *et al.* reported an increased radiation dose of 8 mSv per ablation procedure when CT thermometry was performed, correlating to an additional fatal tumor in 1 out of 2,500 patients [63]. Over the past decade, advancements in CT technology have significantly focused on minimizing radiation doses. Consequently, a new evaluation of the risk versus benefit, taking into account the advancements in CT technology and its impact on patient outcomes, is needed.

Physical density-based thermometry represents a significant benefit in the determination of the thermal expansion coefficient of various tissue types. This methodological advancement lies in the inherent stability of physical density measurements, which unlike attenuation-based thermometry, remain unaffected by the variations in imaging parameters typically associated with CT scans. This consistency may streamline the process by removing the variability and complexity often introduced by differing imaging protocols, thereby enhancing its universal applicability. Such standardization could facilitate broader acceptance and normalization of CT thermometry practices. Nevertheless, further research is needed to determine if the thermal expansion coefficient of tissues can be accurately measured without relying on CT, and how these measurements can be effectively integrated into physical density-based CT thermometry for optimal accuracy.

During a standard ablation procedure, several minutes can elapse between two CT scans. The time gap between consecutive CT scans can lead to interscan motion artifacts resulting from breathing, organ pulsation, or movements by the patient. These artifacts can significantly hinder the monitoring of the ablation zone, as consecutive scans are compared voxel-wise for CT thermometry. To minimize these

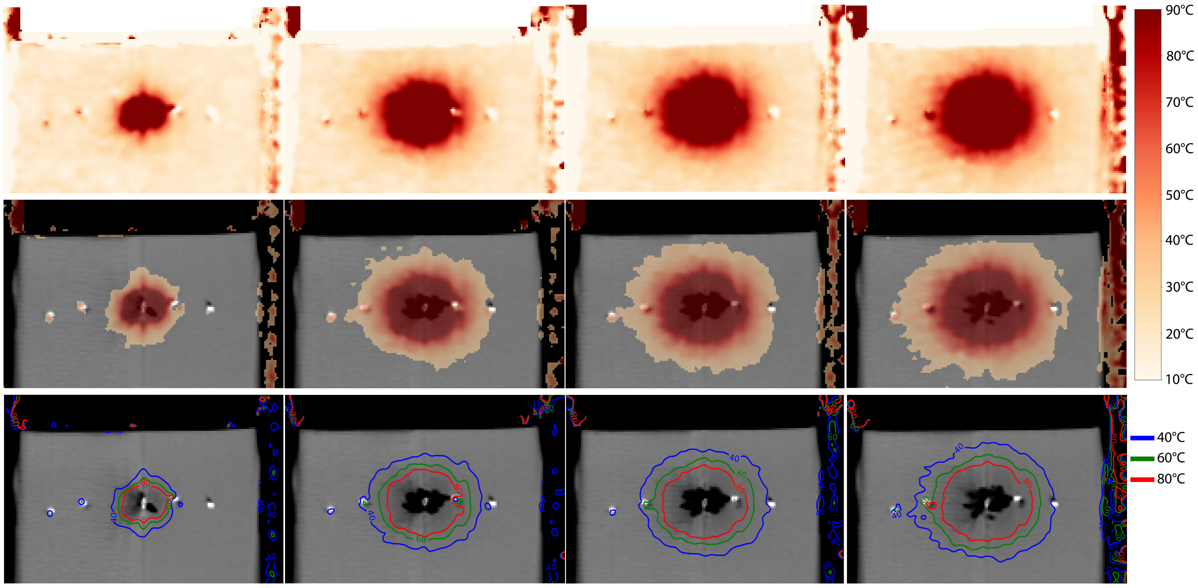

Figure 5.1: This figure presents three methods for visualizing temperature data as acquired with CT during a thermal ablation procedure. The temperature data was obtained using physical density-based thermometry at an energy level of 150 keV, without metal artifacts reduction. The images shown are after 60, 300, 450 and 600 seconds of ablation. The top row depicts thermal maps with a temperature range of 10°C to 90°C. The middle row integrates the thermal map onto the CT images, highlighting regions where the temperature has exceeded 30°C. The bottom row delineates regions of specific thermal significance on the CT image, with isolines at temperatures of 40°C, 60°C, and 80°C. To improve image quality, bilateral filtering was employed on the density maps used to derive the temperature data. This visualization approach assists physicians in accurately delineating the ablation zone.

artifacts, it is essential to accurately register successive images. In a study conducted by Kostyrko *et al.* an in vivo MWA procedure was performed on a pig [64]. Rigid and elastic registration were evaluated both qualitatively and quantitatively for their effectiveness in CT thermometry. The qualitative analysis indicated that rigid registration was marginally less effective compared to other techniques, while quantitative assessments showed that a combined approach of rigid and elastic registration significantly improved movement reduction.

The O-MAR algorithm is effective in reducing metal artifact from large metal implants in CT scans, but faces limitations with smaller metal objects such as surgical stents or needles. Secondary artifacts may arise due to the dimensions of these small objects as O-MAR is not designed for such objects [50]. Challenges are particularly pronounced when these metal objects are adjacent to air spaces; the algorithm tends to mask and exclude these areas, leaving some artifacts uncorrected. This potentially limits the efficacy of O-MAR when gas bubbles are formed around the ablation antenna. The developer of O-MAR advises against using this algorithm for images containing small metal objects near air and have highlighted cases where metal's proximity to air or lung tissue can lead to diagnostic challenges. Furthermore, this study also used the DL-MAR algorithm, which was trained on images with large orthopedic devices implanted in bone tissue. Its performance on needle-like structures in soft tissue has not been investigated before this study. Although DL-MAR demonstrated superior capabilities in reducing image noise and enhancing temperature precision, it was inferior to O-MAR at minimizing artifacts caused by the ablation antenna. Therefore, combining O-MAR and DL-MAR emerges as a synergistic approach to improve CT thermometry. Moreover, training the DL-MAR's deep learning network with images containing artifacts from needle-like structures in soft tissues could establish it as a one-stop solution for enhancing both precision and metal artifact reduction in CT thermometry.

For CT thermometry to be successfully implemented in clinical settings, special focus must be placed on how temperature maps are visualized for physicians. Spectral CT thermometry must achieve two critical goals to be effective: producing precise and accurate temperature maps without metal artifacts, and presenting these maps to physicians in a comprehensive and meaningful manner. Figure 5.1 illustrates various methods for displaying temperature distribution in one repetition conducted in this study. The first row depicts a basic temperature map, ranging from 10°C to 90°C. However, such maps alone are insufficient for clinicians to assess the success of an ablation procedure. It is essential to visualize the tumor location within the temperature distribution to verify that both the tumor and ablation margin are covered by the cytotoxic threshold.

To address this, the second row of Figure 5.1 integrates a temperature overlay on a CT image, ideally one that is contrast-enhanced and taken before ablation to accurately represent the tumor's original volume and position. Alternatively, as shown in the third row, temperature isolines indicating clinically relevant thresholds can be superimposed on the CT image. These isolines simplify the task of determining whether specific tissue areas have exceeded the cytotoxic temperature threshold. Beyond these methods, visualization techniques could extend into three dimensions or incorporate the ablation procedure's duration, offering a more dynamic and informative approach to interpreting temperature data and evaluating treatment efficacy.

5.3. Methodological considerations

Several methodological considerations should be taken into account for this study. Firstly, the design for experiments using porcine liver could have been improved. Conducting these experiments 60 hours after extraction introduced the complication of putrefaction, a decomposition process involving tissue breakdown and gas formation by bacterial and fungal activity. This issue, combined with the utilization of a high ablation power setting, led to the formation of gas bubbles significantly larger than those typically observed in clinical scenarios. In measuring ROIs, a threshold was applied to exclude voxels containing gas. However, the partial volume effect at the borders between gas and tissue might have led to artificially decreased CT values, affecting the reliability of these measurements. Furthermore, the inherent heterogeneity of liver tumors posed challenges in objectively assessing temperature precision and the effectiveness of metal artifact reduction.

Taking these considerations into account, subsequent experiments employed a liver-mimicking gel phantom, designed to replicate the attenuation, dielectric, and thermal properties of human liver tissue [32]. While this choice aimed to eliminate the confounding effects of liver tissue heterogeneity and allow for a more controlled assessment of precision and artifact reduction, it does not fully mimic clinical conditions. Moreover, unlike the experiments with the liver phantom, these tests did not utilize an anthropomorphic abdominal phantom ring. Future research should strive for a more anthropomorphic approach that better reflects the complexities of the clinical environment.

Secondly, the study utilized metallic thermocouples to verify temperature measurements. Previous research has highlighted that the metallic junction's interaction with the microwave field may cause inaccuracies in temperature readings [65]. While this effect was not directly observed in the gel phantom, the liver phantom exhibited exceptionally high temperatures, exceeding 140°C. Switching to fiber optic temperature sensors could potentially eliminate these reading artifacts, as these sensors do not contain metallic components.

The results indicate a notable difference in temperature precision and, in certain instances, the prevalence of metal artifacts between low and high-dose repetitions, with low doses demonstrating more favorable outcomes. Contrary to the expected reduction factor of $\sqrt{2}$ in the high dose setting, such an improvement was not realized. This may originate from the experimental setup. Specifically, the fact that the temperature precision and metal artifact assessments for low and high doses were not conducted within identical repetitions. The high-dose repetitions might have exhibited a greater concentration of metal artifacts in the ROI measurements, in contrast to a more dispersed presence of artifacts throughout the volume in low-dose scans. To address this confounding effect and ensure a more accurate comparison, future research conduct both low and high-dose measurements within the same repetition.

Physical density-based thermometry demonstrated an inferior temperature precision near the ablation antenna compared to attenuation-based thermometry. This lowered precision could be attributed to the fact that the AM-PD model showed an increased root mean square error when applied to materials of lower density, indicating a lower accuracy in these materials. Consequently, the AM-PD model accuracy decreases after heating, as the physical density in proximity to the ablation antenna was substantially lowered. To address this limitation, further research may be needed to improve the accuracy of the AM-PD model in low-density materials.

5.4. Future research

Although CT thermometry is based on a simple concept, it has a significant challenge: different tissues, patients, and ablation methods can have different parameters of the thermometry model (α and β). These parameters are difficult or impossible to measure in vivo, and they can be substantially different from the ex vivo measurements that are done under different physiological conditions. Also, the thermal properties of the target region may be altered by the intense heat during thermal ablation, which may introduce further errors [10].

Some studies have also reported that the thermometry parameters are not constant with large temperature variations, implying that α and β are a function of temperature. These studies suggest that quadratic [66], [67], cubic [68] or exponential [69], [70] models fit the experimental data better than the linear model. These studies also suggest that tissue heating and cooling affect the CT numbers differently.

Lastly, tissue properties may change due to heating, for instance, with increasing distance from the microwave antenna. Lopresto *et al.* investigated the impact of temperature-dependent variations in tissue properties on the outcomes of MWA. They concluded that a maximum variation of ± 25% in dielectric and thermal properties must be incorporated into the accurate prediction of the ablation zone [71]. This highlights the importance of considering tissue property variability in MWA treatment planning to enhance the predictability of ablation outcomes. It also suggests that the parameters of a thermometry model are not constant with temperature changes, implying that these parameters should be adjusted based on the distance from the ablation antenna.

Future studies, essential for the clinical translation of CT thermometry, should include evaluations that consider tissue heterogeneity, the presence of other anatomical structures, and the heat-sink effect. Research could be structured around experiments using ex vivo liver tissues or phantoms that are perfused, incorporate various tissue types—healthy, cirrhotic, or tumorous—or are subject to intraprocedural movement. A critical step before human trials could involve using CT thermometry, including postprocessing such as registration, denoising, and MAR, to monitor different ablation procedures (such as radiofrequency, microwave, or cryoablation and variations in ablation power) on living pigs. Finally, active research must focus on establishing thermometry parameters across diverse conditions, tissue types, and patient demographics. Given the wide range of variance sources, this field presents a range of research opportunities.

Spectral CT may enhance CT thermometry by leveraging its ability to discriminate between materials, which enables the generation of mappings for specific tissues such as liver and tumors. This capability is a significant advancement over single-energy CT, which lacks the specificity to distinguish between different types of tissues with similar densities. By discriminating tissues and voxel-wise assigning them varying thermometry parameters specific to their composition, more accurate temperature mappings may be generated. Furthermore, improved tissue discrimination provided by spectral CT facilitates the development of personalized treatment plans. Understanding how various tissues respond to temperature changes enables clinicians to tailor treatments to individual patients, thereby improving treatment efficacy and reducing recurrence rates.
Recently, Wang *et al.* used improved material decomposition capabilities of photon-counting CT to develop a deep learning-based thermometry tool [72]. This tool was developed using the linear attenuation coefficient in four energy bins at different temperatures to build a non-linear thermometry model. Although the tool was tested on non-anthropomorphic materials, results showed a mean absolute error of 3.40°C. Further research is needed to determine if either photon-counting CT or deep learning-based thermometry is promising for the future.

CT thermometry shows potential for monitoring ablation procedures in the liver, but it is not the only image post-processing technique to monitor the ablation zone. Ziv and colleagues developed two algorithms designed to noninvasively evaluate treatment success during the procedure [73]. Similar to CT thermometry, these algorithms necessitate a pre-ablation and a intra-procedure scan for analysis. The first algorithm is based on image subtraction, thresholding, and morphological refinement. It implicitly draws on CT thermometry principles because of its reliance on changes in HU. The algorithm was compared to a gold standard, which were gross pathology contours of corresponding CT scan slices. Results demonstrated a mean absolute difference from pathology contours of the ablation zone radius of 1.04 ± 0.74 mm, indicating a high accuracy.

The second algorithm utilizes radial optical flow, specifically the Lucas-Kanade method, applied to a polar transformation of the CT images [74]. Although the details are complex, its core concept is based on detecting the radial expansion of the ablation front around the antenna. By focusing on changes in the texture of consecutive CT images, radial optical flow calculates the expansion of the ablation area over time. This method was tested in an in vivo pig ablation study and was validated against contrast-enhanced post-ablation CT scans. It demonstrated high accuracy in contouring the ablation zone and effectively handled challenges associated with major blood vessels and blood flow.

However, both algorithms entail a significant increase in radiation dose due to the necessity for multiple consecutive scans. In conclusion, when evaluating these post-processing algorithms for ablation zone monitoring against CT thermometry, a thorough comparison is essential to ascertain which method offers superior predictive accuracy for the success of ablation treatments.

6

Conclusion

This study has demonstrated the applicability of spectral CT thermometry for non-invasive temperature monitoring during liver microwave ablation, comparing physical density-based thermometry to attenuation-based methods. The results indicate that physical density maps, especially at 150 keV when used in combination with DL-MAR and O-MAR, significantly reduce metal artifacts. Additionally, they enhance temperature precision and accuracy, bringing temperature measurements closer to the clinically required 2°C threshold.

One of the primary challenges in spectral CT thermometry lies in accurately determining the parameters of the thermometry model, which can vary significantly across different tissue types, perfusion rates, patient characteristics, or ablation techniques. These parameters are critical as they directly influence the accuracy of temperature predictions. Variations in tissue composition and the dynamic nature of thermal properties during ablation make it difficult to standardize these parameters, thereby complicating the calibration of CT thermometry for individual cases.
Looking forward, the potential use of photon counting CT in this domain is particularly promising. This technology could enhance the discrimination of tissue types and improve the accuracy of temperature mappings, which is crucial for tailoring treatments to individual patients. Furthermore, considering the complex behavior of tissue when heated, the development of deep learning-based thermometry tools represents a significant advancement toward more precise and personalized ablation treatments.

The findings from this study establish a robust foundation for advancing the development and clinical application of spectral CT thermometry. By continuously refining CT parameters, this research strives to improve the safety and effectiveness of CT-guided microwave ablation procedures. Furthermore, the progression of spectral CT thermometry is streamlining the clinical adoption of non-invasive temperature monitoring in thermal ablation treatments, ultimately reducing the risk of local tumor recurrence.

References

[1] L. Crocetti, T. de Baére, P. L. Pereira, *et al.*, “CIRSE Standards of Practice on Thermal Ablation of Liver Tumours,” *Cardiovascular and Interventional Radiology*, Jul. 2020. DOI: 10.1007/s00270-020-02471-z.

[2] M. Nikfarjam, V. Muralidharan, and C. Christophi, “Mechanisms of Focal Heat Destruction of Liver Tumors,” *Journal of Surgical Research*, Aug. 2005. DOI: 10.1016/j.jss.2005.02.009.

[3] E. M. Knavel and C. L. Brace, “Tumor Ablation: Common Modalities and General Practices,” *Techniques in Vascular and Interventional Radiology*, Ablation Update, Dec. 2013. DOI: 10.1053/j.tvir.2013.08.002.

[4] S. Clasen, H. Rempp, R. Hoffmann, *et al.*, “Image-guided radiofrequency ablation of hepatocellular carcinoma (HCC): Is MR guidance more effective than CT guidance?” *European Journal of Radiology*, Jan. 2014. DOI: 10.1016/j.ejrad.2013.09.018.

[5] L. Crocetti, C. Della Pina, D. Cioni, *et al.*, “Peri-intraprocedural imaging: US, CT, and MRI,” *Abdominal Imaging*, Dec. 2011. DOI: 10.1007/s00261-011-9750-9.

[6] L. Frich, “Non□invasive thermometry for monitoring hepatic radiofrequency ablation,” *Minimally Invasive Therapy & Allied Technologies*, Jan. 2006. DOI: 10.1080/13645700500470025.

[7] S. N. Goldberg, C. J. Grassi, J. F. Cardella, *et al.*, “Image-guided Tumor Ablation: Standardization of Terminology and Reporting Criteria,” *Journal of Vascular and Interventional Radiology*, Society of Interventional Radiology 2009 Standards’ Division Guidelines Supplement, Jul. 2009. DOI: 10.1016/j.jvir.2009.04.011.

[8] N. V. Violi, R. Duran, B. Guiu, *et al.*, “Efficacy of microwave ablation versus radiofrequency ablation for the treatment of hepatocellular carcinoma in patients with chronic liver disease: A randomised controlled phase 2 trial,” *The Lancet Gastroenterology & Hepatology*, May 2018. DOI: 10.1016/S2468-1253(18)30029-3.

[9] P. Saccomandi, E. Schena, and S. Silvestri, “Techniques for temperature monitoring during laser-induced thermotherapy: An overview,” *International Journal of Hyperthermia*, Nov. 2013. DOI: 10.3109/02656736.2013.832411.

[10] F. Fani, E. Schena, P. Saccomandi, *et al.*, “CT-based thermometry: An overview.,” *International journal of hyperthermia : the official journal of European Society for Hyperthermic Oncology, North American Hyperthermia Group*, Jun. 2014. DOI: 10.3109/02656736.2014.922221.

[11] A. Tang, O. Hallouch, V. Chernyak, *et al.*, “Epidemiology of hepatocellular carcinoma: Target population for surveillance and diagnosis,” *Abdominal Radiology (New York)*, Jan. 2018. DOI: 10.1007/s00261-017-1209-1.

[12] J. D. Yang, P. Hainaut, G. J. Gores, *et al.*, “A global view of hepatocellular carcinoma: Trends, risk, prevention and management,” *Nature Reviews Gastroenterology & Hepatology*, Oct. 2019. DOI: 10.1038/s41575-019-0186-y.

[13] A. Villanueva, “Hepatocellular Carcinoma,” *The New England Journal of Medicine*, Apr. 2019. DOI: 10.1056/NEJMra1713263.

[14] M. Reig, A. Forner, J. Rimola, *et al.*, “BCLC strategy for prognosis prediction and treatment recommendation: The 2022 update,” *Journal of hepatology*, Mar. 2022. DOI: 10.1016/j.jhep.2021.11.018.

[15] J. M. Llovet, X. Mas, J. J. Aponte, *et al.*, “Cost effectiveness of adjuvant therapy for hepatocellular carcinoma during the waiting list for liver transplantation,” *Gut*, Jan. 2002.

[16] K. F. Chu and D. E. Dupuy, “Thermal ablation of tumours: Biological mechanisms and advances in therapy,” *Nature Reviews Cancer*, Mar. 2014. DOI: 10.1038/nrc3672.

[17] B. Cady, R. L. Jenkins, G. D. Steele, *et al.*, “Surgical margin in hepatic resection for colorectal metastasis: A critical and improvable determinant of outcome,” *Annals of Surgery*, Apr. 1998. DOI: `10.1097/00000658-199804000-00019`.

[18] K. Verdonschot, S. Arts, P. Van den Boezem, *et al.*, “Ablative margins in percutaneous thermal ablation of hepatic tumors: A systematic review,” *Expert Review of Anticancer Therapy*, Sep. 2023. DOI: `10.1080/14737140.2023.2247564`.

[19] M. G. Lubner, C. L. Brace, J. L. Hinshaw, *et al.*, “Microwave tumor ablation: Mechanism of action, clinical results, and devices,” *Journal of vascular and interventional radiology: JVIR*, Aug. 2010. DOI: `10.1016/j.jvir.2010.04.007`.

[20] A. S. Wright, F. T. Lee, and D. M. Mahvi, “Hepatic microwave ablation with multiple antennae results in synergistically larger zones of coagulation necrosis,” *Annals of Surgical Oncology*, Apr. 2003. DOI: `10.1245/aso.2003.03.045`.

[21] B. G. Fallone, P. R. Moran, and E. B. Podgorsak, “Noninvasive thermometry with a clinical x-ray CT scanner.,” *Medical physics*, Oct. 1982. DOI: `10.1118/1.595117`.

[22] G. M. Bydder and L. Kreel, “The temperature dependence of computed tomography attenuation values,” *Journal of computer assisted tomography*, Aug. 1979. DOI: `10.1097/00004728-197908000-00013`.

[23] A. H. Mahnken and P. Bruners, “CT thermometry: Will it ever become ready for use?” *International journal of clinical practice. Supplement*, Apr. 2011. DOI: `10.1111/j.1742-1241.2011.02651.x`.

[24] J. Jenne, M. Bahner, J. Spoo, *et al.*, “CT on-line monitoring of HIFU therapy,” in *1997 IEEE Ultrasonics Symposium Proceedings. An International Symposium (Cat. No.97CH36118)*, Oct. 1997. DOI: `10.1109/ULTSYM.1997.661833`.

[25] P. Bruners, E. Levit, T. Penzkofer, *et al.*, “Multi-slice computed tomography: A tool for non-invasive temperature measurement?” *International journal of hyperthermia : the official journal of European Society for Hyperthermic Oncology, North American Hyperthermia Group*, 2010. DOI: `10.3109/02656731003605654`.

[26] G. D. Pandeya, J. H. G. M. Klaessens, M. J. W. Greuter, *et al.*, “Feasibility of computed tomography based thermometry during interstitial laser heating in bovine liver.,” *European radiology*, Aug. 2011. DOI: `10.1007/s00330-011-2106-6`.

[27] J. Pohlan, W. Kress, K.-G. Hermann, *et al.*, “Computed Tomography Thermography for Ablation Zone Prediction in Microwave Ablation and Cryoablation: Advantages and Challenges in an Ex Vivo Porcine Liver Model.,” *Journal of computer assisted tomography*, Oct. 2020. DOI: `10.1097/RCT.0000000000001081`.

[28] L. P. Liu, R. Pua, D. N. Rosario-Berrios, *et al.*, “Spectral CT thermometry with improved temperature sensitivity for image-guided thermal ablation,” in *Medical Imaging 2023: Physics of Medical Imaging*, Apr. 2023. DOI: `10.1117/12.2649111`.

[29] A. Heinrich, S. Schenkl, D. Buckreus, *et al.*, “CT-based thermometry with virtual monoenergetic images by dual-energy of fat, muscle and bone using FBP, iterative and deep learning-based reconstruction.,” *European radiology*, Jan. 2022. DOI: `10.1007/s00330-021-08206-z`.

[30] J. Paul, T. J. Vogl, and A. Chacko, “Dual energy computed tomography thermometry during hepatic microwave ablation in an ex-vivo porcine model.,” *Physica medica : PM : an international journal devoted to the applications of physics to medicine and biology : official journal of the Italian Association of Biomedical Physics (AIFB)*, Nov. 2015. DOI: `10.1016/j.ejmp.2015.05.014`.

[31] L. P. Liu, M. Hwang, M. Hung, *et al.*, “Non-invasive mass and temperature quantifications with spectral CT.,” *Scientific reports*, Apr. 2023. DOI: `10.1038/s41598-023-33264-2`.

[32] L. P. Liu, R. Pua, D. N. Rosario-Berrios, *et al.*, “Reproducible spectral CT thermometry with liver-mimicking phantoms for image-guided thermal ablation,” *Physics in Medicine and Biology*, Jan. 2024. DOI: `10.1088/1361-6560/ad2124`.

[33] J. D. B. O’Sullivan, J. Behnsen, T. Starborg, *et al.*, “X-ray micro-computed tomography (μCT): An emerging opportunity in parasite imaging,” *Parasitology*, Jun. 2018. DOI: `10.1017/S0031182017002074`.

[34] W. Huda, “Review of Radiologic Physics,” *Journal of Applied Clinical Medical Physics*, Mar. 2003. DOI: 10.1120/jacmp.v4i2.2535.

[35] F. E. Boas and D. Fleischmann, “CT artifacts: Causes and reduction techniques,” *Imaging in Medicine*, Apr. 2012. DOI: 10.2217/iim.12.13.

[36] Z. Fatima, N. Ali, M. A. Williams, *et al.*, “X-ray scattering and attenuation cross-sections and coefficients of bone, brain, lung, fat, and soft tissue for applications in dosimetry, cancer detection, and treatment,” *Radiation Physics and Chemistry*, Jul. 2023. DOI: 10.1016/j.radphyschem.2023.110908.

[37] R. E. Alvarez and A. Macovski, “Energy-selective reconstructions in X-ray computerised tomography,” *Physics in Medicine & Biology*, Sep. 1976. DOI: 10.1088/0031-9155/21/5/002.

[38] J. A. Seibert and J. M. Boone, “X-Ray Imaging Physics for Nuclear Medicine Technologists. Part 2: X-Ray Interactions and Image Formation,” *Journal of Nuclear Medicine Technology*, Mar. 2005.

[39] M. J. Willemink, M. Persson, A. Pourmorteza, *et al.*, “Photon-counting CT: Technical Principles and Clinical Prospects,” *Radiology*, Nov. 2018. DOI: 10.1148/radiol.2018172656.

[40] C. H. McCollough, K. Boedeker, D. Cody, *et al.*, “Principles and applications of multienergy CT: Report of AAPM Task Group 291,” *Medical Physics*, 2020. DOI: 10.1002/mp.14157.

[41] C. H. McCollough, S. Leng, L. Yu, *et al.*, “Dual- and Multi-Energy CT: Principles, Technical Approaches, and Clinical Applications,” *Radiology*, Sep. 2015. DOI: 10.1148/radiol.2015142631.

[42] J. F. Williamson, S. Li, S. Devic, *et al.*, “On two-parameter models of photon cross sections: Application to dual-energy CT imaging,” *Medical Physics*, Nov. 2006. DOI: 10.1118/1.2349688.

[43] C.-h. Hua, N. Shapira, T. E. Merchant, *et al.*, “Accuracy of electron density, effective atomic number, and iodine concentration determination with a dual-layer dual-energy computed tomography system,” *Medical Physics*, 2018. DOI: 10.1002/mp.12903.

[44] J. Greffier, S. Si-Mohamed, D. Dabli, *et al.*, “Performance of four dual-energy CT platforms for abdominal imaging: A task-based image quality assessment based on phantom data,” *European Radiology*, Jul. 2021. DOI: 10.1007/s00330-020-07671-2.

[45] C. Maass, M. Baer, and M. Kachelriess, “Image-based dual energy CT using optimized precorrection functions: A practical new approach of material decomposition in image domain,” *Medical Physics*, Aug. 2009. DOI: 10.1118/1.3157235.

[46] A. So and S. Nicolaou, “Spectral Computed Tomography: Fundamental Principles and Recent Developments,” *Korean Journal of Radiology*, Jan. 2021. DOI: 10.3348/kjr.2020.0144.

[47] M. J. Willemink, P. A. de Jong, T. Leiner, *et al.*, “Iterative reconstruction techniques for computed tomography Part 1: Technical principles,” *European Radiology*, Jun. 2013. DOI: 10.1007/s00330-012-2765-y.

[48] M. Selles, J. A. C. van Osch, M. Maas, *et al.*, “Advances in metal artifact reduction in CT images: A review of traditional and novel metal artifact reduction techniques,” *European Journal of Radiology*, Jan. 2024. DOI: 10.1016/j.ejrad.2023.111276.

[49] *Philips Metal Artifact Reduction for Orthopedic Implants (O□MAR). White paper.* 2012.

[50] H. Li, C. Noel, H. Chen, *et al.*, “Clinical evaluation of a commercial orthopedic metal artifact reduction tool for CT simulations in radiation therapy,” *Medical Physics*, Dec. 2012. DOI: 10.1118/1.4762814.

[51] T. M. Coupal, P. I. Mallinson, P. McLaughlin, *et al.*, “Peering through the glare: Using dual-energy CT to overcome the problem of metal artefacts in bone radiology,” *Skeletal Radiology*, May 2014. DOI: 10.1007/s00256-013-1802-5.

[52] M. Selles, D. J. Slotman, J. A. C. van Osch, *et al.*, “Is AI the way forward for reducing metal artifacts in CT? Development of a generic deep learning-based method and initial evaluation in patients with sacroiliac joint implants,” *European Journal of Radiology*, Jun. 2023. DOI: 10.1016/j.ejrad.2023.110844.

[53] P. Homolka, A. Gahleitner, and R. Nowotny, “Temperature dependence of HU values for various water equivalent phantom materials,” *Physics in Medicine & Biology*, Aug. 2002. DOI: 10.1088/0031-9155/47/16/307.

[54] M. Hwang, H. I. Litt, P. B. Noël, *et al.*, "Accurate physical density assessments from clinical spectral results," in *Medical Imaging 2021: Physics of Medical Imaging*, Feb. 2021. DOI: `10.1117/12.2581748`.

[55] D. R. White, J. Booz, R. V. Griffith, *et al.*, "4. The Composition of Body Tissues," *Reports of the International Commission on Radiation Units and Measurements*, Jan. 1989. DOI: `10.1093/jicru_os23.1.20`.

[56] "XCOM: Photon Cross Sections Database," *NIST*, Sep. 2009.

[57] L. P. Liu, M. Hung, M. C. Soulen, *et al.*, "Real-time spectral CT thermometry via physical density for image-guided tumor ablation," in *Medical Imaging 2022: Physics of Medical Imaging*, Apr. 2022. DOI: `10.1117/12.2608743`.

[58] M. Alonzo, A. Bos, S. Bennett, *et al.*, "The Emprint™ Ablation System with Thermosphere™ Technology: One of the Newer Next-Generation Microwave Ablation Technologies," *Seminars in Interventional Radiology*, Dec. 2015. DOI: `10.1055/s-0035-1564811`.

[59] A. H. Negussie, A. Partanen, A. S. Mikhail, *et al.*, "Thermochromic tissue-mimicking phantom for optimisation of thermal tumour ablation.," *International journal of hyperthermia : the official journal of European Society for Hyperthermic Oncology, North American Hyperthermia Group*, May 2016. DOI: `10.3109/02656736.2016.1145745`.

[60] International Commission on Radiation Units and Measurements, "ICRU Report No. 87: Radiation dose and image-quality assessment in computed tomography," *Journal of the ICRU*, Apr. 2012. DOI: `10.1093/jicru/ndt007`.

[61] F. Hübner, R. Schreiner, B. Panahi, *et al.*, "Evaluation of the thermal sensitivity of porcine liver in CT-guided cryoablation: An initial study.," *Medical physics*, Oct. 2020. DOI: `10.1002/mp.14432`.

[62] L. Winter, E. Oberacker, K. Paul, *et al.*, "Magnetic resonance thermometry: Methodology, pitfalls and practical solutions," *International Journal of Hyperthermia*, Jan. 2016. DOI: `10.3109/02656736.2015.1108462`.

[63] G. D. Pandeya, M. J. W. Greuter, B. Schmidt, *et al.*, "Assessment of thermal sensitivity of CT during heating of liver: An ex vivo study.," *The British journal of radiology*, Sep. 2012. DOI: `10.1259/bjr/23942179`.

[64] B. Kostyrko, K. Rubarth, C. Althoff, *et al.*, "Evaluation of Different Registration Algorithms to Reduce Motion Artifacts in CT-Thermography (CTT).," *Diagnostics (Basel, Switzerland)*, Jun. 2023. DOI: `10.3390/diagnostics13122076`.

[65] K. Gammampila, P. B. Dunscombe, B. M. Southcott, *et al.*, "Thermocouple thermometry in microwave fields," *Clinical Physics and Physiological Measurement: An Official Journal of the Hospital Physicists' Association, Deutsche Gesellschaft Fur Medizinische Physik and the European Federation of Organisations for Medical Physics*, Nov. 1981. DOI: `10.1088/0143-0815/2/4/005`.

[66] N. Weiss, J. Sosna, S. N. Goldberg, *et al.*, "Non-invasive temperature monitoring and hyperthermic injury onset detection using X-ray CT during HIFU thermal treatment in ex vivo fatty tissue.," *International journal of hyperthermia : the official journal of European Society for Hyperthermic Oncology, North American Hyperthermia Group*, Mar. 2014. DOI: `10.3109/02656736.2014.883466`.

[67] E. Schena, P. Saccomandi, F. Giurazza, *et al.*, "Experimental assessment of CT-based thermometry during laser ablation of porcine pancreas.," *Physics in medicine and biology*, Aug. 2013. DOI: `10.1088/0031-9155/58/16/5705`.

[68] K.-W. Li, D. Fujiwara, A. Haga, *et al.*, "Physical density estimations of single- and dual-energy CT using material-based forward projection algorithm: A simulation study.," *The British journal of radiology*, Dec. 2021. DOI: `10.1259/bjr.20201236`.

[69] L. Strigari, S. Minosse, D. D'Alessio, *et al.*, "Microwave thermal ablation using CT-scanner for predicting the variation of ablated region over time: Advantages and limitations.," *Physics in medicine and biology*, May 2019. DOI: `10.1088/1361-6560/ab1a67`.

[70] N. Weiss, S. N. Goldberg, J. Sosna, *et al.*, "Temperature-density hysteresis in X-ray CT during HIFU thermal ablation: Heating and cooling phantom study.," *International journal of hyperthermia : the official journal of European Society for Hyperthermic Oncology, North American Hyperthermia Group*, Feb. 2014. DOI: `10.3109/02656736.2013.860241`.

[71] V. Lopresto, R. Pinto, L. Farina, *et al.*, "Microwave thermal ablation: Effects of tissue properties variations on predictive models for treatment planning," *Medical Engineering & Physics*, Aug. 2017. DOI: `10.1016/j.medengphy.2017.06.008`.

[72] N. Wang, M. Li, and P. Haverinen, "Photon-counting computed tomography thermometry via material decomposition and machine learning.," *Visual computing for industry, biomedicine, and art*, Jan. 2023. DOI: `10.1186/s42492-022-00129-w`.

[73] O. Ziv, S. N. Goldberg, Y. Nissenbaum, *et al.*, "Optical flow and image segmentation analysis for noninvasive precise mapping of microwave thermal ablation in X-ray CT scans - ex vivo study.," *International journal of hyperthermia : the official journal of European Society for Hyperthermic Oncology, North American Hyperthermia Group*, Sep. 2018. DOI: `10.1080/02656736.2017.1375160`.

[74] O. Ziv, S. N. Goldberg, Y. Nissenbaum, *et al.*, "In vivo noninvasive three-dimensional (3D) assessment of microwave thermal ablation zone using non-contrast-enhanced x-ray CT," *Medical Physics*, 2020. DOI: `10.1002/mp.14428`.

A

Source Code

```python
# Standard library imports
import math
import os
import re
from datetime import date, datetime, timedelta

# Third-party libraries for data handling and computation
import numpy as np
import pandas as pd
import pydicom
import statsmodels.api as sm
from scipy.ndimage import rotate
from scipy.optimize import curve_fit, least_squares
from sklearn.linear_model import LinearRegression
from sklearn.metrics import mean_squared_error, r2_score

# Image processing and analysis libraries
import SimpleITK as sitk
from skimage import io, measure, restoration
from skimage.morphology import (closing, cube, opening, remove_small_objects,
                                skeletonize, square)

# Visualization libraries
import matplotlib.pyplot as plt
from matplotlib.colors import Normalize
from matplotlib.ticker import MaxNLocator


def main():
    object_analyzer = ObjectAnalyzer(C.ref_scan_path)
    segment_results = object_analyzer.analyze(C.lower_thresh_1, C.upper_thresh_1, C.
        lower_thresh_2, C.upper_thresh_2)
    metal_rois = object_analyzer.view_slice_draw_roi()
    folder = 'DICOM_O_DL_MAR' if (C.DLMAR and C.O_MAR) else 'DICOM_DL_MAR' if C.DLMAR else '
        DICOM_O_MAR' if C.O_MAR else 'DICOM'
    # Perform PD-based thermometry
    if C.thermometry_method == 'PD':
        PD_maps = {}
        monoE_maps = {}
        PD_dataframes = []
        metal_dataframes = []
        columns = [['Object␣Label', 'Mean', 'SD', '#Voxels', 'Scan␣Time', 'Acquisition'],
                   ['Scan␣time', 'mean_prox', 'SD_prox', 'mean_dist', 'SD_dist']]
        # Perform reparametrization
        params, mu_water = Reparametrization(C.monoE_level).fit_model()
        for mono_entry in tqdm(os.listdir(os.path.join(C.root_path, f'MonoE{C.monoE_level}',
            folder)), desc="Making␣PD␣maps"):
            mono_entry_path = os.path.join(C.root_path, f'MonoE{C.monoE_level}', folder,
                mono_entry)

```

```
            if os.path.isdir(mono_entry_path):
                for file in os.listdir(mono_entry_path):
                    if file.startswith(('I', 'E')):
                        dcm_data = pydicom.dcmread(os.path.join(mono_entry_path, file))
                        mono_image_time = dcm_data.AcquisitionTime
                        break

                for zeff_entry in os.listdir(os.path.join(C.root_path, 'Zeff', folder)):
                    zeff_entry_path = os.path.join(C.root_path, 'Zeff', folder, zeff_entry)

                    if os.path.isdir(zeff_entry_path):
                        for file2 in os.listdir(zeff_entry_path):
                            if file2.startswith('I'):
                                dcm_data = pydicom.dcmread(os.path.join(zeff_entry_path,
                                    file2))
                                zeff_image_time = dcm_data.AcquisitionTime
                                break

                        if mono_image_time == zeff_image_time:
                            PD_map = AM_PD(mono_entry_path, zeff_entry_path, C.monoE_level,
                                params,
                                                   mu_water).generate_PD_map()
                            PD_maps[zeff_image_time] = PD_map
                            roi_analyzer = ROIMeasurements(mono_entry_path, segment_results,
                                C.lower_threshold_liver_PD,
                                                           C.upper_threshold_liver_PD, PD_map
                                                               =PD_map)
                            roi_results = roi_analyzer.calculate_roi_2()
                            # Convert roi_results to DataFrame and store it in the list
                            for label, data in roi_results.items():
                                row = [label, data['mean'], data['SD'], data['#voxels'], data
                                    ['Scan␣time'],
                                       data['Acquisition']]
                                PD_dataframes.append(pd.DataFrame([row], columns=columns[0]))
                            #     analyze and store results from noise_metal function
                            metal_roi_results = roi_analyzer.noise_metal(metal_rois)
                            row = [metal_roi_results['Scan␣time'], metal_roi_results['
                                mean_prox'],
                                   metal_roi_results['SD_prox'],
                                   metal_roi_results['mean_dist'], metal_roi_results['SD_dist
                                       ']]
                            metal_dataframes.append(pd.DataFrame([row], columns=columns[1]))
        # Concatenate all DataFrames in the list
        roi_results_df = pd.concat(PD_dataframes, ignore_index=True)
        metal_results_df = pd.concat(metal_dataframes, ignore_index=True)
        # Process temperature sensor data
        temperature_processor = TemperatureDataProcessor(C.temperature_sensor_path)
        processed_sensor_data = temperature_processor.load_and_process_data(C.scan_date)
        # Save the DataFrame to an Excel file
        current_time = datetime.now().strftime("%Y%m%d-%H%M%S")
        file_name = os.path.basename(C.thermometry_method) + str(C.monoE_level) + "_" +
            folder + '_' + str(C.slice) + 'mm_' + current_time + ".xlsx"
        excel_path = os.path.join(C.output_path, file_name)

        with pd.ExcelWriter(excel_path, engine='openpyxl',
                            mode='a' if os.path.exists(excel_path) else 'w') as writer:
            roi_results_df.to_excel(writer, index=False, sheet_name='ROI␣measurements')
            processed_sensor_data.to_excel(writer, index=False, sheet_name='Sensor␣
                measurements')
            metal_results_df.to_excel(writer, index=False, sheet_name='Metal␣ROI␣measurements
                ')

        # Temp_sensitivity
        linear_regression = TemperatureHURegression(excel_path)
        linear_regression.temperature_tolerance()

        # temperature mapping
        temperature_mapper = TempMap(PD_maps, ref_temp=18.2, monoE=monoE_maps)
        temp_maps = temperature_mapper.perform_temperature_map_NLM()
        temperature_mapper.plot_temperature_maps(53)
        temperature_mapper.plot_temperature_maps_with_isolines(53)
```

```python
        temperature_mapper.plot_temp_overlay(53)

        # Calculate mean temperature in ROIs close to sensors
        columns = ['Object Label', 'Mean', 'SD', '#Voxels', 'Scan Time']
        temp_dataframes = []
        for scan_time, temp_map in tqdm(temp_maps.items(), desc='Calculating ROI on temp_maps'):
            temp_analyzer = ROIMeasurements(None, segment_results, C.lower_temp_threshold, C.upper_temp_threshold, temp_map=temp_map)
            temp_roi_results = temp_analyzer.calculate_roi_2()
            # Convert temp_results to DataFrame and store it in the list
            for label, data in temp_roi_results.items():
                row = [label, data['mean'], data['SD'], data['#voxels'], scan_time]
                temp_dataframes.append(pd.DataFrame([row], columns=columns))

        all_temp_df = pd.concat(temp_dataframes, ignore_index=True)
        with pd.ExcelWriter(excel_path, engine='openpyxl', mode='a' if os.path.exists(excel_path) else 'w', if_sheet_exists='replace') as writer:
            all_temp_df.to_excel(writer, index=False, sheet_name='Temp ROI measurements')
        # Check if temperature maps correspond to sensor measuremenst
        temperature_regression = TemperatureHURegression(excel_path)
        temperature_regression.temp_map_sensor_regression()
        temperature_regression.bland_altman_plot()

    # Perform HU-based thermometry
    if C.thermometry_method == 'HU':
        HU_dataframes = []
        metal_dataframes = []
        columns = [['Object Label', 'Mean', 'SD', '#Voxels', 'Scan Time', 'Acquisition'],
                   ['Scan time', 'mean_prox', 'SD_prox', 'mean_dist', 'SD_dist', '#Voxels']]
        for entry in tqdm(os.listdir(os.path.join(C.root_path, 'Idose', folder)), desc="Analyzing Scans"):
            entry_path = os.path.join(C.root_path, 'Idose', folder, entry)
            if os.path.isdir(entry_path):
                if C.thermometry_method == 'HU':
                    roi_analyzer = ROIMeasurements(entry_path, segment_results, C.lower_threshold_liver_HU,
                                                   C.upper_threshold_liver_HU)
                    roi_results = roi_analyzer.calculate_roi_2()
                # Convert roi_results to DataFrame and store it in the list
                for label, data in roi_results.items():
                    row = [label, data['mean'], data['SD'], data['#voxels'], data['Scan time'], data['Acquisition']]
                    HU_dataframes.append(pd.DataFrame([row], columns=columns[0]))
                metal_roi_results = roi_analyzer.noise_metal(metal_rois)
                row = [metal_roi_results['Scan time'], metal_roi_results['mean_prox'],
                       metal_roi_results['SD_prox'],
                       metal_roi_results['mean_dist'], metal_roi_results['SD_dist'], metal_roi_results['#Voxels']]
                metal_dataframes.append(pd.DataFrame([row], columns=columns[1]))
        # Concatenate all DataFrames in the list
        roi_results_df = pd.concat(HU_dataframes, ignore_index=True)
        metal_results_df = pd.concat(metal_dataframes, ignore_index=True)
        # Process temperature sensor data
        temperature_processor = TemperatureDataProcessor(C.temperature_sensor_path)
        processed_sensor_data = temperature_processor.load_and_process_data(C.scan_date)
        # Save the DataFrame to an Excel file
        current_time = datetime.now().strftime("%Y%m%d-%H%M%S")
        file_name = os.path.basename(C.thermometry_method) + "_" + folder + '_' + str(C.slice) + 'mm_' + current_time + ".xlsx"
        excel_path = os.path.join(C.output_path, file_name)

        with pd.ExcelWriter(excel_path, engine='openpyxl', mode='a' if os.path.exists(excel_path) else 'w') as writer:
            roi_results_df.to_excel(writer, index=False, sheet_name='ROI measurements')
            processed_sensor_data.to_excel(writer, index=False, sheet_name='Sensor measurements')
            metal_results_df.to_excel(writer, index=False, sheet_name='Metal ROI measurements')
        # Temp_sensitivity
        linear_regression = TemperatureHURegression(excel_path)
```

```
        linear_regression.temperature_tolerance()
        #temperature mapping
        temperature_mapper = TempMap(os.path.join(C.root_path, 'Idose', folder), ref_temp=18.2)
        temp_maps = temperature_mapper.perform_all_temperature_mappings()
        temperature_mapper.plot_temperature_maps(95)
        temperature_mapper.plot_temperature_maps_with_isolines(95)
        temperature_mapper.plot_temp_overlay(65)
        # Calculate mean temperature in ROIs close to sensors
        temp_dataframes = []
        for scan_time, temp_map in tqdm(temp_maps.items(), desc='Calculating␣ROI␣on␣temp_maps'):
            temp_analyzer = ROIMeasurements(None, segment_results, C.lower_temp_threshold, C.upper_temp_threshold, temp_map=temp_map)
            temp_roi_results = temp_analyzer.calculate_roi_2()


class ObjectAnalyzer:
    def __init__(self, directory_path):
        self.directory_path = directory_path
        self.volume = None
        self.labeled_volume = None
        self.endpoints = None
        self.rois = {}

    def load_dicom_volume(self):
        files = [pydicom.dcmread(os.path.join(self.directory_path, f)) for f in os.listdir(self.directory_path) if f.startswith(('I', 'E'))]
        files.sort(key=lambda x: float(x.ImagePositionPatient[2]))
        rescale_slope = files[0].RescaleSlope
        rescale_intercept = files[0].RescaleIntercept
        self.volume = np.stack([s.pixel_array * rescale_slope + rescale_intercept for s in files])
        self.volume = rotate(self.volume, angle=90, axes=(0, 2), reshape=True, mode='constant')
        self.volume = self.volume[200:300, 200:300, :]
        return self.volume


    def threshold_and_label(self, lower_thresh_1, upper_thresh_1, lower_thresh_2, upper_thresh_2, min_size=150):
        binary_1 = (self.volume >= lower_thresh_1) & (self.volume <= upper_thresh_1)
        binary_2 = (self.volume >= lower_thresh_2) & (self.volume <= upper_thresh_2).astype(int)
        binary_2 = closing(binary_1 | binary_2, cube(5))

        labeled_volume_1 = measure.label(binary_2)
        self.labeled_volume = labeled_volume_1
        self.labeled_volume = remove_small_objects(self.labeled_volume, min_size=min_size)

    def find_object_endpoints(self):
        properties = measure.regionprops(self.labeled_volume)
        self.endpoints = []
        for prop in properties:
            min_slice, min_row, min_col, max_slice, max_row, max_col = prop.bbox
            object_label = prop.label
            y_indices_bottom, x_indices_bottom = np.where(self.labeled_volume[min_slice, :, :] == object_label)
            cxb, cyb = self.calculate_center(x_indices_bottom, y_indices_bottom, min_slice)
            y_indices_top, x_indices_top = np.where(self.labeled_volume[max_slice - 1, :, :] == object_label)
            cxt, cyt = self.calculate_center(x_indices_top, y_indices_top, max_slice - 1)
            if cxb is not None and cyt is not None:
                self.endpoints.append({
                    'object_label': object_label,
                    'bottom': (cxb, cyb, min_slice),
                    'top': (cxt, cyt, max_slice - 1),
                    'size': prop.area
                })

    def calculate_center(self, x_indices, y_indices, slice_index):
```

```
        if len(y_indices) > 0 and len(x_indices) > 0:
            cx = int(round(np.median(x_indices)))
            cy = int(round(np.median(y_indices)))
            return cx, cy
        return None, None

    def find_longest_object(self):
        longest_length = 0
        longest_object = None
        for obj in self.endpoints:
            length = np.linalg.norm(np.array(obj['top']) - np.array(obj['bottom']))
            if length > longest_length:
                longest_length = length
                longest_object = obj
        return longest_object

    def calculate_circle_center_radius(self, other_object, longest_object):
        z_top = other_object['top'][2]
        y_indices, x_indices = np.where(self.labeled_volume[z_top, :, :] == longest_object['object_label'])

        if len(y_indices) > 0 and len(x_indices) > 0:
            cx = np.median(x_indices)
            cy = np.median(y_indices)
            center = (cx, cy, z_top)
            radius = np.linalg.norm(np.array([cx, cy]) - np.array([other_object['top'][0], other_object['top'][1]]))
            return {'center': center, 'radius': radius}
        return None


    def analyze(self, lower_thresh_1, upper_thresh_1, lower_thresh_2, upper_thresh_2):
        self.load_dicom_volume()
        self.threshold_and_label(lower_thresh_1, upper_thresh_1, lower_thresh_2, upper_thresh_2)
        self.find_object_endpoints()
        longest_object = self.find_longest_object()
        results = {}
        for obj in self.endpoints:
            if obj['object_label'] != longest_object['object_label']:
                circle_info = self.calculate_circle_center_radius(obj, longest_object)
                if circle_info:
                    results[obj['object_label']] = {
                        'circle_center': circle_info['center'],
                        'circle_radius': circle_info['radius'],
                        'sensor_top'   : obj['top']
                    }
        self.visualize_segmented_objects_and_circles()
        return results


class Reparametrization:
    def __init__(self, E):
        self.df = pd.read_excel('path', sheet_name="Zeff␣Aeff␣keV")
        self.rho = np.array([self.df['Rho␣[kg*m^-3]'][1:181]], dtype=float) / 1000
        self.Zeff = np.array([self.df['Zeff'][1:181]], dtype=float)
        self.Aeff = np.array([self.df['Aeff'][1:181]], dtype=float)
        self.E = E
        self.mu_water = self.df[self.df['E'] == self.E]['mu_water'].iloc[0]
        self.muE = np.array([self.df[f'{self.E}␣keV'][1:181]], dtype=float)
        self.muE = self.muE * self.rho
        self.optimized_params = None
        self.fKN = None

    def residuals(self, params):
        p1, p2, p3, p4, p5, p6, p7 = params
        model = (p1 * self.Aeff * (self.muE ** p2)) / ((p3 * (self.Zeff ** p4) / (self.E ** p5)) + (self.Zeff ** p6) * (self.fKN ** p7))

        return (model - self.rho).transpose().flatten()

```

```python
    def fit_model(self):
        # klein nishina calculation
        alpha = self.E / 510.975
        fKN = ((1 + alpha) / alpha ** 2) * (
                    (2 + 2 * alpha) / (1 + 2 * alpha) - 1 / alpha * math.log(1 + 2 * alpha))
                        + 1 / \
              (2 * alpha) * math.log(1 + 2 * alpha) - (1 + 3 * alpha) / (1 + 2 * alpha) ** 2
        self.fKN = fKN
        # Initial guess
        initial_guess = np.array([3.5, 1.1, 46, 4.2, 2.9, 1, 1])
        lower_bounds = np.array([0, 0, 0, 0, 0, 0, 0])
        upper_bounds = np.array([100, 100, 100, 100, 100, 100, 100])
        # Perform least squares optimization
        result = least_squares(self.residuals, initial_guess, bounds=(lower_bounds,
            upper_bounds))
        self.optimized_params = result.x
        return result.x, self.mu_water


class AM_PD:
    def __init__(self, mono_entry_path, zeff_entry_path, E, params, mu_water):
        self.Aeff = None
        self.E = E
        self.mono_entry_path = mono_entry_path
        self.zeff_entry_path = zeff_entry_path
        self.params = params
        self.mu_water = mu_water
        self.muE = None
        self.Zeff = None
        self.PD_map = None
        self.patient_ID = None
        self.series_description = None
        self.scan_time = None

    def load_muE(self):
        files = [pydicom.dcmread(os.path.join(self.mono_entry_path, f)) for f in os.listdir(
            self.mono_entry_path) if f.startswith(('I', 'E'))]
        files.sort(key=lambda x: float(x.ImagePositionPatient[2]))
        self.scan_time = files[0].AcquisitionTime
        self.patient_ID = files[0].PatientID
        self.series_description = files[0].SeriesDescription
        rescale_slope = files[0].RescaleSlope
        rescale_intercept = files[0].RescaleIntercept
        monoE = np.stack([s.pixel_array * rescale_slope + rescale_intercept for s in files])
        monoE = rotate(monoE, angle=90, axes=(0, 2), reshape=True, mode='constant')
        monoE = monoE[200:300, 200:300, :]
        self.muE = (monoE * self.mu_water) / 1000 + self.mu_water
        return self.muE

    def load_Zeff_Aeff(self):
        """Loads Zeff and Aeff values from DICOM files"""
        files = [pydicom.dcmread(os.path.join(self.zeff_entry_path, f)) for f in os.listdir(
            self.zeff_entry_path) if f.startswith(('I', 'E'))]
        files.sort(key=lambda x: float(x.ImagePositionPatient[2]))
        rescale_slope = files[0].RescaleSlope
        rescale_intercept = files[0].RescaleIntercept
        self.Zeff = np.stack([f.pixel_array * rescale_slope + rescale_intercept for f in
            files])
        self.Zeff = rotate(self.Zeff, angle=90, axes=(0, 2), reshape=True, mode='constant')
        self.Zeff = self.Zeff[200:300, 200:300, :]
        self.Aeff = 0.436191 + 1.85908 * self.Zeff + 0.0154491 * self.Zeff ** 2 - 0.000173656
             * self.Zeff ** 3

    def generate_PD_map(self):
        """Generates the PD map"""
        self.load_muE()
        self.load_Zeff_Aeff()
        p1, p2, p3, p4, p5, p6, p7 = self.params
        alpha = self.E / 510.975  # Klein-Nishina calculation
        fKN = ((1 + alpha) / alpha ** 2) * ((2 + 2 * alpha) / (1 + 2 * alpha) - 1 / alpha *
            np.log(1 + 2 * alpha)) + 1 / (2 * alpha) * np.log(1 + 2 * alpha) - (1 + 3 * alpha
```

```
            ) / (1 + 2 * alpha) ** 2
        self.PD_map = (p1 * self.Aeff * self.muE**p2) / ((p3 * self.Zeff**p4) / self.E**p5 +
            self.Zeff**p6 * fKN**p7)
        self.PD_map[np.isnan(self.PD_map)] = 0
        self.PD_map[np.isinf(self.PD_map)] = 0
        self.PD_map[self.PD_map < 0.05] = 0
        self.PD_map[self.PD_map > 1000] = 0
        return self.PD_map


class ROIMeasurements:
    def __init__(self, directory_path, results, lower_threshold_liver, upper_threshold_liver,
         PD_map=None, temp_map=None):
        self.patient_ID = None
        self.series_description = None
        self.directory_path = directory_path
        self.volume = None
        self.PD_map = PD_map
        self.temp_map = temp_map
        self.results = results
        self.lower_threshold_liver = lower_threshold_liver
        self.upper_threshold_liver = upper_threshold_liver
        self.roi_results = {}
        self.metal_roi_results = {}
        self.scan_time = None

    def load_dicom(self):
        files = [pydicom.dcmread(os.path.join(self.directory_path, f)) for f in os.listdir(
            self.directory_path) if f.startswith(('I', 'E'))]
        files.sort(key=lambda x: float(x.ImagePositionPatient[2]))
        rescale_slope = files[0].RescaleSlope
        rescale_intercept = files[0].RescaleIntercept
        self.scan_time = files[0].get('AcquisitionTime', None)
        self.patient_ID = files[0].get('PatientID', None)
        self.series_description = files[0].get('SeriesDescription', None)
        self.volume = np.stack([s.pixel_array * rescale_slope + rescale_intercept for s in
            files])
        self.volume = rotate(self.volume, angle=90, axes=(0, 2), reshape=True, mode='constant
            ')
        self.volume = self.volume[200:300, 200:300, :]

    def resample_slices(self, slice_thickness, increment, current_thickness=1):
        new_slices = []
        num_slices_to_avg = int(slice_thickness / current_thickness)
        increment_steps = int(increment / current_thickness)
        # Padding both ends of the volume by mirroring
        pad_width = num_slices_to_avg // 2
        padded_volume = np.pad(self.volume, ((pad_width - 1, pad_width), (0, 0), (0, 0)),
            mode='reflect')
        i = 0
        while i < len(padded_volume) - num_slices_to_avg + 1:
            averaged_slice = np.mean(padded_volume[i:i + num_slices_to_avg], axis=0)
            new_slices.append(averaged_slice)
            i += increment_steps

        new_volume = np.array(new_slices)
        return new_volume

    def calculate_roi_tolerance_2(self):
        if C.thermometry_method == 'HU':
            self.load_dicom()
        elif C.thermometry_method == 'PD':
            self.load_dicom()
            self.volume = self.PD_map

        ROI_dim_mm = np.array([2, 2, C.slice])  # Desired ROI dimensions in mm
        voxel_size_mm = np.array([0.6836, 0.6836, 1])  # [x, y, z] in mm
        ROI_dim_voxels = np.ceil(ROI_dim_mm / voxel_size_mm).astype(int)  # Convert mm to
            voxels

        for obj_label, obj_info in self.results.items():
```

```
            center = np.array(obj_info['circle_center'])
            angle = 2.3
            radius = obj_info['circle_radius']
            start = center + 1.114 * radius * np.array([0, np.sin(angle), np.cos(angle)]) #1.114 for correction of different z,y voxels sizes
            included_voxels = []

            z_indices = []
            if C.slice == 1:
                z_indices = range(int(start[2]), int(start[2]) + 1)  # For slice thickness of 1
            elif C.slice == 2:
                z_indices = [int(start[2]), int(start[2]) + 2]  # For slice thickness of 2

            for z in z_indices:
                for y in range(int(start[1]), int(start[1]) + ROI_dim_voxels[1]):
                    for x in range(int(start[0]), int(start[0]) + ROI_dim_voxels[0]):
                        included_voxels.append(self.volume[x, y, z])

            if filtered_voxels:
                mean_val = np.mean(filtered_voxels)
                std_dev = np.std(filtered_voxels)
                voxel_count = len(filtered_voxels)

                self.roi_results[obj_label] = {
                    'mean': mean_val,
                    'SD': std_dev,
                    '#voxels': voxel_count,
                    'Scan␣time': self.scan_time,
                    'Acquisition': self.patient_ID + self.series_description
                }
        return self.roi_results


    def calculate_roi_2(self):
        if (C.thermometry_method == 'HU' or C.thermometry_method == 'mu') and (self.temp_map is None): # for measurements on HU maps
            self.load_dicom()
            roi_radius = 6
        elif (C.thermometry_method == 'PD') and (self.temp_map is None): # for measurements on PD maps
            self.load_dicom()
            self.volume = self.PD_map
            roi_radius = 6
        else: # for ROI measurements in temp_maps
            self.volume = self.temp_map
            roi_radius = 6
        if C.slice != 1:
            self.volume = self.resample_slices(C.slice, C.increment)

        for obj_label, obj_info in self.results.items():
            center = obj_info['circle_center']
            radius = obj_info['circle_radius']
            object_top = obj_info['sensor_top']

            angle_object_top = np.arctan2(object_top[1] - center[1], object_top[2] - center[2])
            shift_angle = np.arctan2(2.5 * roi_radius, radius)
            angle_roi_1 = angle_object_top + shift_angle
            angle_roi_2 = angle_object_top - shift_angle
            roi_center_1 = center + radius * np.array([0, np.sin(angle_roi_1), np.cos(angle_roi_1)])
            roi_center_2 = center + radius * np.array([0, np.sin(angle_roi_2), np.cos(angle_roi_2)])

            self.roi_visualization_data[obj_label] = {
                'roi_center_1': roi_center_1,
                'roi_center_2': roi_center_2,
                'roi_radius': roi_radius,
                'slice_index': int(center[0])
            }
```

```
            def calculate_roi_metrics(roi_center, roi_radius):
                included_voxels = []
                x = int(roi_center[0])
                for y in range(self.volume.shape[1]):
                    for z in range(self.volume.shape[2]):
                        dist_to_center = np.linalg.norm(np.array([y, z]) - roi_center[1:])
                        if dist_to_center <= roi_radius:
                            included_voxels.append(self.volume[x, y, z])
                return included_voxels

            voxels_roi_1 = calculate_roi_metrics(roi_center_1, roi_radius)
            voxels_roi_2 = calculate_roi_metrics(roi_center_2, roi_radius)

            combined_voxels = voxels_roi_1 + voxels_roi_2

            if combined_voxels:
                combined_mean = np.mean(combined_voxels)
                combined_std_dev = np.std(combined_voxels)
                combined_voxel_count = len(combined_voxels)

            self.patient_ID = "" if self.patient_ID is None else self.patient_ID
            self.series_description = "" if self.series_description is None else self.series_description
            self.roi_results[obj_label] = {
                    'mean': combined_mean,
                    'SD': combined_std_dev,
                    '#voxels': combined_voxel_count,
                    'Scan␣time': self.scan_time,
                    'Acquisition': self.patient_ID + self.series_description
            }
        return self.roi_results

    def noise_metal(self, metal_rois):
        if C.thermometry_method == 'PD':
            self.volume = self.PD_map
        elif C.thermometry_method == 'HU' or C.thermometry_method == 'mu':
            self.load_dicom()
        if C.slice != 1:
            self.volume = self.resample_slices(C.slice, C.increment)
        prox_center = metal_rois[0][0:3]
        prox_radius = metal_rois[0][3]
        dist_center = metal_rois[1][0:3]
        dist_radius = metal_rois[1][3]

        def calculate_roi_metrics(roi_center, roi_radius):
            included_voxels = []
            x = int(roi_center[0])
            for y in range(self.volume.shape[1]):
                for z in range(self.volume.shape[2]):
                    dist_to_center = np.linalg.norm(np.array([y, z]) - roi_center[1:])
                    if dist_to_center <= roi_radius:
                        included_voxels.append(self.volume[x, y, z])
            return included_voxels

        voxels_prox_roi = calculate_roi_metrics(prox_center, prox_radius)
        voxels_dist_roi = calculate_roi_metrics(dist_center, dist_radius)

        self.patient_ID = "" if self.patient_ID is None else self.patient_ID
        self.series_description = "" if self.series_description is None else self.series_description
        self.metal_roi_results = {
            'mean_prox': np.mean(voxels_prox_roi),
            'mean_dist': np.mean(voxels_dist_roi),
            'SD_prox': np.std(voxels_prox_roi),
            'SD_dist': np.std(voxels_dist_roi),
            '#Voxels': len(voxels_dist_roi),
            'Scan␣time': self.scan_time,
            'Acquisition': self.patient_ID + self.series_description
        }

        return self.metal_roi_results
```

```


class TemperatureHURegression:
    def __init__(self, file_path):
        self.file_path = file_path
        self.roi_df = pd.read_excel(file_path, sheet_name='ROI␣measurements')
        self.sensor_df = pd.read_excel(file_path, sheet_name='Sensor␣measurements')
        self.roi_df['Scan␣Time'] = pd.to_datetime(self.roi_df['Scan␣Time'], format='%H%M%S').dt.time
        self.sensor_df['Rounded␣Time'] = pd.to_datetime(self.sensor_df['Rounded␣Time']).dt.time
        self.coupled_data = {}

    def find_closest_time(self, roi_time, sensor_times):
        roi_time = datetime.strptime(str(roi_time), '%H:%M:%S').time()
        # add time to align scan time with sensor time, see notes in phone
        roi_time_with_offset = (datetime.combine(datetime.today(), roi_time) + timedelta(seconds=28)).time()
        min_diff = None
        closest_time = None
        for time in sensor_times:
            diff = (datetime.combine(datetime.today(), roi_time_with_offset) -
                    datetime.combine(datetime.today(), time)).total_seconds()
            if min_diff is None or abs(diff) < abs(min_diff):
                min_diff = diff
                closest_time = time
        return closest_time


    def perform__combined_weighted_regression_hu(self):
        # Combined data across all objects for regression
        combined_temp_diffs, combined_hu_diffs, combined_sd_hus = [], [], []
        for object_label in range(1, 5):
            object_data = self.roi_df[self.roi_df['Object␣Label'] == object_label]
            temps, mean_hus, sd_hus, times = [], [], [], []
            for _, row in object_data.iterrows():
                closest_sensor_time = self.find_closest_time(row['Scan␣Time'], self.sensor_df['Rounded␣Time'])
                temperature = self.sensor_df[self.sensor_df['Rounded␣Time'] == closest_sensor_time][
                    f'Temp{object_label}'].values
                if temperature.size > 0:
                    temps.append(temperature[0])
                    mean_hus.append(row['Mean'])
                    sd_hus.append(row['SD'])
                    times.append(closest_sensor_time)
            # Filtering and sorting data
            hu_temp_time_pairs = [(HU, SD, temp, time) for HU, SD, temp, time in zip(mean_hus, sd_hus, temps, times) if
                                  pd.notna(HU) and pd.notna(temp)]
            if not hu_temp_time_pairs:
                continue

            # Sort by time
            hu_temp_time_pairs.sort(key=lambda x: x[3])
            mean_hus_sorted, sd_hus_sorted, temps_sorted, times_sorted = zip(*hu_temp_time_pairs)

            # Convert to numpy arrays
            ref_HU = np.array(mean_hus_sorted)[0]
            ref_temp = np.array(temps_sorted)[0]

            hu_temp_time_pairs = hu_temp_time_pairs[1:]     # exclude measurements from reference scan

            hu_temp_time_pairs.sort(key=lambda x: x[0])
            mean_hus_sorted, sd_hus_sorted, temps_sorted, _ = zip(*hu_temp_time_pairs)
            mean_hus_sorted, sd_hus_sorted, temps_sorted = map(np.array, [mean_hus_sorted, sd_hus_sorted, temps_sorted])

            temp_diffs = temps_sorted - ref_temp
```

```
            hu_diffs = mean_hus_sorted - ref_HU

            # Append to combined data for regression
            combined_temp_diffs.extend(temp_diffs)
            combined_hu_diffs.extend(hu_diffs)
            combined_sd_hus.extend(sd_hus_sorted)

        # Perform regression on combined data
        combined_temp_diffs, combined_hu_diffs, combined_sd_hus = map(np.array,
                                                                      [
                                                                          combined_temp_diffs
                                                                          ,
                                                                       combined_hu_diffs,
                                                                       combined_sd_hus])

        weights = 1 / np.square(combined_sd_hus)
        X = sm.add_constant(combined_temp_diffs.reshape(-1, 1))
        wls_model = sm.WLS(combined_hu_diffs, X, weights=weights)
        results = wls_model.fit()

        # Store the results
        self.coupled_data = {
            'coefficients': coefficient,
            'intercept': intercept,
            'std_err_coefficient': std_err_coefficient,
            'std_err_intercept': std_err_intercept,
            'r_squared': results.rsquared  # Store R^2 score
        }


    def perform__combined_weighted_regression_pd(self):
        # Combined data across all objects for regression
        combined_relative_pd, combined_temps, combined_mean_pds, combined_sd_pds,
            combined_temp_diffs = [], [], [], [], []
        for object_label in range(1, 5):
            object_data = self.roi_df[self.roi_df['Object␣Label'] == object_label]
            temps, mean_pds, sd_pds, times = [], [], [], []
            for _, row in object_data.iterrows():
                closest_sensor_time = self.find_closest_time(row['Scan␣Time'], self.sensor_df
                    ['Rounded␣Time'])
                temperature = self.sensor_df[self.sensor_df['Rounded␣Time'] ==
                    closest_sensor_time][
                    f'Temp{object_label}'].values
                if temperature.size > 0:
                    temps.append(temperature[0])
                    mean_pds.append(row['Mean'])
                    sd_pds.append(row['SD'])
                    times.append(closest_sensor_time)
            # Filtering and sorting data
            pd_temp_time_pairs = [(PD, SD, temp, time) for PD, SD, temp, time in zip(mean_pds
                , sd_pds, temps, times) if
                                  pd.notna(PD) and pd.notna(temp)]
            if not pd_temp_time_pairs:
                continue
            pd_temp_time_pairs.sort(key=lambda x: x[3])
            mean_pds_sorted, sd_pds_sorted, temps_sorted, _ = zip(*pd_temp_time_pairs)
            mean_pds_sorted, sd_pds_sorted, temps_sorted = map(np.array, [mean_pds_sorted,
                sd_pds_sorted, temps_sorted])
            ref_PD, ref_temp = mean_pds_sorted[0], temps_sorted[0]
            relative_pd = (np.ones_like(mean_pds_sorted) * ref_PD) / mean_pds_sorted
            temp_diff = temps_sorted - ref_temp

            relative_pd = relative_pd[1:] # exclude reference scan from regression analysis
            temp_diff = temp_diff[1:]
            sd_pds_sorted = sd_pds_sorted[1:]
            # Append to combined data for regression
            combined_relative_pd.extend(relative_pd)
            combined_temps.extend(temps_sorted)
            combined_mean_pds.extend(mean_pds_sorted)
            combined_sd_pds.extend(sd_pds_sorted)
            combined_temp_diffs.extend(temp_diff)
```

```
        # Perform regression on combined data
        combined_temps, combined_relative_pd, combined_sd_pds, combined_temp_diffs = map(np.array,
                                                                                          [combined_temps,
                                                                                           combined_relative_pd,
                                                                                           combined_sd_pds,
                                                                                           combined_temp_diffs])
        weights = 1 / np.square(combined_sd_pds)
        X = sm.add_constant(combined_temp_diffs.reshape(-1, 1))
        wls_model = sm.WLS(combined_relative_pd, X, weights=weights)
        results = wls_model.fit()
        # Store the results
        self.coupled_data = {
            'coefficients': coefficient,
            'intercept': intercept,
            'std_err_coefficient': std_err_coefficient,
            'std_err_intercept': std_err_intercept,
            'r_squared': results.rsquared  # Store R^2 score
        }


    def temperature_tolerance(self):
        def calculate_tolerance(mean, sd, vox, times):
            if mean and sd:
                HU_sorted, sd_sorted, vox_sorted, times_sorted = zip(*sorted(zip(mean, sd, vox, times), key=lambda x: x[3]))
                mean_ref = np.array(HU_sorted)[0]
                sd_ref = np.array(sd_sorted)[0] / np.array(vox_sorted)[0]**0.5
                mean_T = np.array(HU_sorted)[-1]
                sd_T = np.array(sd_sorted)[-1] / np.array(vox_sorted)[-1]**0.5
                if 'HU' in self.file_path:
                    alpha, del_alpha = C.alphaHU, C.alphaHUsd
                    beta, del_beta = C.betaHU, C.betaHUsd
                    err_ref = (1/alpha * sd_ref)**2
                    err_T = (-1/alpha * sd_T)**2
                    err_alpha = ((mean_T - mean_ref - beta)/alpha**2 * del_alpha)**2
                    err_beta = (1/alpha * del_beta)**2
                    return (err_ref + err_T + err_alpha + err_beta)**0.5
                elif 'PD' in self.file_path:
                    alpha, del_alpha = C.alphaPD, C.alphaPDsd
                    beta, del_beta = C.betaPD, C.betaPDsd
                    err_ref = (1/(alpha * mean_T) * sd_ref)**2
                    err_T = (mean_ref/(alpha * mean_T**2) * sd_T)**2
                    err_alpha = ((-1/alpha**2)*((mean_ref/mean_T) - beta) * del_alpha)**2
                    err_beta = (1/alpha * del_beta)**2
                    return (err_ref + err_T + err_alpha + err_beta)**0.5
            else:
                return None
        #noise tolerance
        noise_tolerance = {}
        for object_label in [10, 15, 20, 25]:      #range(1, 5):  # Assuming there are 4 objects
            object_data = self.roi_df[self.roi_df['Object␣Label'] == object_label]
            mean = []
            sd = []
            vox = []
            times = []
            for _, row in object_data.iterrows():
                mean.append(row['Mean'])
                sd.append(row['SD'])
                vox.append(row['#Voxels'])
                times.append(row['Scan␣Time'])

            noise_tolerance[object_label] = calculate_tolerance(mean, sd, vox, times)
        self.coupled_data['noise_tolerance'] = noise_tolerance

```

```
        #metal tolerance
        mean_prox, sd_prox, mean_dist, sd_dist = [], [], [], []
        times = []
        vox = []
        for _, row in self.metal_df.iterrows():
            mean_prox.append(row['mean_prox'])
            sd_prox.append(row['SD_prox'])
            vox.append(1)                           # because we dont want to have the standard error for artifacts
            mean_dist.append(row['mean_dist'])
            sd_dist.append(row['SD_dist'])
            times.append(row['Scan␣time'])

        tolerance_prox = calculate_tolerance(mean_prox, sd_prox, vox, times)
        tolerance_dist = calculate_tolerance(mean_dist, sd_dist, vox, times)

        # Combine the tolerances into a single dictionary
        metal_tolerance = {'prox': tolerance_prox, 'dist': tolerance_dist}
        self.coupled_data['metal_tolerance'] = metal_tolerance


    def bland_altman_plot(self):
        temp_roi_df = self.temp_roi_df
        sensor_df = self.sensor_df
        df_merged = pd.DataFrame()

        for sensor in range(1, 5):
            sensor_measurements = sensor_df.copy()
            sensor_measurements['Sensor'] = sensor  # Adding sensor identifier to sensor measurements
            sensor_measurements['Temp'] = sensor_measurements[f'Temp{sensor}']  # Simplify column naming

            for index, row in temp_roi_df.iterrows():
                if row['Object␣Label'] == sensor:
                    closest_sensor_time = self.find_closest_time(row['Scan␣Time'], sensor_measurements['Rounded␣Time'])
                    matched_sensor_row = sensor_measurements[sensor_measurements['Rounded␣Time'] == closest_sensor_time]
                    if not matched_sensor_row.empty:
                        df_merged = pd.concat([df_merged, pd.DataFrame({
                            'Mean': [row['Mean']],
                            'Measured␣Temp': matched_sensor_row['Temp'].values[0],
                            'Sensor': [sensor],
                            'Rounded␣Time': [closest_sensor_time]
                        })])
        # Calculate differences and means after merging
        df_merged['Difference'] = df_merged['Measured␣Temp'] - df_merged['Mean']
        df_merged['Mean'] = (df_merged['Measured␣Temp'] + df_merged['Mean']) / 2
        # Add mean difference and limits of agreement
        mean_diff = df_merged['Difference'].mean()
        std_diff = df_merged['Difference'].std()
        upper_loa = mean_diff + 1.96 * std_diff
        lower_loa = mean_diff - 1.96 * std_diff


class TempMap:
    def __init__(self, base_directory_path, ref_temp, monoE=None):
        self.scan_time = None
        self.bilateral_filter = None
        self.base_directory_path = base_directory_path
        self.ref_temp = ref_temp # Temperature of tissue of reference scan, measured by sensors
        self.alpha = None # best alpha to be determined
        self.volume_t0 = None  # Reference scan at T0
        if C.thermometry_method == 'PD':
            self.monoE = monoE
        self.temperature_maps = {}  # Stores temperature maps for t1, t2, t3, etc.
        self.volume_t = {} # store volumes for t1, t2, t3 etc.

    def load_dicom_volume(self, directory_path):
```

```python
        files = [pydicom.dcmread(os.path.join(directory_path, f)) for f in os.listdir(directory_path) if
                 f.startswith('I')]
        files.sort(key=lambda x: float(x.ImagePositionPatient[2]))
        self.scan_time = files[0].get('AcquisitionTime', None)
        rescale_slope = files[0].RescaleSlope
        rescale_intercept = files[0].RescaleIntercept
        volume = np.stack([s.pixel_array * rescale_slope + rescale_intercept for s in files])
        volume = rotate(volume, angle=90, axes=(0, 2), reshape=True, mode='constant')
        volume = volume[200:300, 200:300, :]
        return volume

    def calculate_temperature_map(self, volume_t, ref_temp):
        # Register volume_t to volume_t0
        elastixImageFilter = sitk.ElastixImageFilter()
        if np.ndim(self.volume_t0) > 1:
            elastixImageFilter.SetFixedImage(sitk.GetImageFromArray(self.volume_t0))
        else:
            elastixImageFilter.SetFixedImage(self.volume_t0)
        elastixImageFilter.SetMovingImage(volume_t)
        elastixImageFilter.LogToConsoleOn()
        # Set up the parameters for translation
        parameterMap = sitk.GetDefaultParameterMap('rigid')
        elastixImageFilter.SetParameterMap(parameterMap)
        # Execute the registration
        elastixImageFilter.Execute()
        volume_t = elastixImageFilter.GetResultImage()
        # Get the result
        volume_t = sitk.GetArrayFromImage(volume_t)
        if np.ndim(self.volume_t0) < 2:
            self.volume_t0 = sitk.GetArrayFromImage(self.volume_t0)
        if C.thermometry_method == 'HU':
            # Calculate the change in Hounsfield Units (Delta HU) voxel-wise
            self.alpha = C.alphaHU
            beta = C.betaHU
            delta_hu = volume_t - self.volume_t0
            delta_t = (delta_hu - beta) / self.alpha
        elif C.thermometry_method == 'PD':
            self.alpha = C.alphaPD
            beta = C.betaPD
            relative_pd = self.volume_t0 / volume_t
            delta_t = (relative_pd - beta) / self.alpha
        T = delta_t + ref_temp
        return T

    def perform_temperature_map_NLM(self):
        if C.thermometry_method == 'HU':
            def extract_number(directory_name):
                match = re.search(r'S(\d+)', directory_name)
                return int(match.group(1)) if match else 0

            directories = [d for d in os.listdir(self.base_directory_path) if
                           os.path.isdir(os.path.join(self.base_directory_path, d))]
            directories.sort(key=extract_number)  # Sort directories based on the extracted number
            reference_directory = directories[0]  # Reference scan directory
            print("Reference directory:", reference_directory)
            self.volume_t0 = self.load_dicom_volume(
                os.path.join(self.base_directory_path, reference_directory, 'DICOM_DL_MAR'))
            # estimate the noise standard deviation from the noisy image
            sigma = 2.1
            patch_kw = dict(patch_size=3,  # 3x3 patches
                            patch_distance=4)  # 9x9 search area
            # fast algorithm
            self.volume_t0 = restoration.denoise_nl_means(self.volume_t0, h=0.8 * sigma, sigma=sigma,
                                                          fast_mode=True,
                                                          **patch_kw)
            for directory in tqdm(directories[1:], desc='Filter and register'):  # Skip the reference directory
                volume_t = self.load_dicom_volume(os.path.join(self.base_directory_path,
```

```
                    directory, 'DICOM_DL_MAR'))
                scan_time = self.scan_time
                self.volume_t[scan_time] = volume_t
                volume_t = restoration.denoise_nl_means(volume_t, h=0.8 * sigma, sigma=sigma,
                                                        fast_mode=True,
                                                        **patch_kw)
                volume_t = sitk.GetImageFromArray(volume_t)
                temperature_map = self.calculate_temperature_map(volume_t, self.ref_temp)
                self.temperature_maps[scan_time] = temperature_map
        elif C.thermometry_method == 'PD':
            PD_maps = self.base_directory_path
            sorted_PD_maps = sorted(PD_maps.items(), key=lambda item: item[0])
            reference_ac_time, self.volume_t0 = sorted_PD_maps[0]
            print('Reference␣acquisition␣time␣is:', reference_ac_time)
            self.volume_t = dict(sorted_PD_maps[1:])
            sigma = 0.02
            patch_kw = dict(patch_size=3,  # 3x3 patches
                            patch_distance=4)  # 9x9 search area
            # fast algorithm
            self.volume_t0 = restoration.denoise_nl_means(self.volume_t0, h=0.8 * sigma,
                sigma=sigma,
                                                          fast_mode=True,
                                                          **patch_kw)
            # Iterate over each directory and calculate temperature maps
            for scan_time, PD_map in tqdm(self.volume_t.items(), desc='Filter␣and␣register'):
                PD_map = restoration.denoise_nl_means(volume_t, h=0.8 * sigma, sigma=sigma,
                                                            fast_mode=True, **patch_kw)
                PD_map = sitk.GetImageFromArray(PD_map)
                temperature_map = self.calculate_temperature_map(PD_map, self.ref_temp)
                self.temperature_maps[scan_time] = temperature_map
        return self.temperature_maps

    def plot_temperature_maps(self, initial_slice_index):
        def extract_number(time_point):
            match = re.search(r'S(\d+)', time_point)
            return int(match.group(1)) if match else 0
        rowcol = math.ceil(np.sqrt(len(self.temperature_maps)))
        fig, axs = plt.subplots(rowcol, rowcol, figsize=(20, 20))
        axs = axs.flatten()  # Flatten the 2D array of axes

        # Initial plotting
        for i, (time_point, temperature_map) in enumerate(sorted_temperature_maps):
            ax = axs[i]
            window_width = 80
            window_level = 50
            lower_bound = window_level - (window_width / 2)
            upper_bound = window_level + (window_width / 2)
            windowed_map = np.clip(temperature_map, lower_bound, upper_bound)
            im = ax.imshow(windowed_map[initial_slice_index], cmap='OrRd', interpolation='
                nearest', vmin=lower_bound, vmax=upper_bound) #'gist_heat'
            ax.set_title(f'Slice␣of␣scan␣{time_point}␣-␣Slice␣{initial_slice_index}')
            ax.axis('off')
        plt.show()

    def plot_temperature_maps_with_isolines(self, initial_slice_index):
        def extract_number(time_point):
            match = re.search(r'S(\d+)', time_point)
            return int(match.group(1)) if match else 0
        window_width = 400
        window_level = 60
        lower_bound = window_level - (window_width / 2)
        upper_bound = window_level + (window_width / 2)

        rowcol = math.ceil(np.sqrt(len(self.temperature_maps)))
        fig, axs = plt.subplots(rowcol, rowcol, figsize=(20, 20))
        axs = axs.flatten()
        sorted_temperature_maps = sorted(self.temperature_maps.items(), key=lambda x:
            extract_number(x[0]))
        max_slices = max(len(temp_map) for temp_map in self.temperature_maps.values())
        # Pre-calculate and store isoline data
        isoline_data = {}
```

```
        for time_point, temperature_map in sorted_temperature_maps:
            data_per_slice = []
            for slice_index in range(len(temperature_map)):
                X, Y = np.meshgrid(np.arange(temperature_map[slice_index].shape[1]),
                                   np.arange(temperature_map[slice_index].shape[0]))
                Z = temperature_map[slice_index]
                data_per_slice.append((X, Y, Z))
            isoline_data[time_point] = data_per_slice
        current_slice = [initial_slice_index]
        slice_index_text = fig.text(0.5, 0.01, f'Slice␣Index:␣{initial_slice_index}', ha='
            center')
        def update_slice(event):
            if event.button == 'up' and current_slice[0] < max_slices - 1:
                current_slice[0] += 1
            elif event.button == 'down' and current_slice[0] > 0:
                current_slice[0] -= 1
            for i, (time_point, _) in enumerate(sorted_temperature_maps):
                ax = axs[i]
                ax.clear()
                slice_data = self.volume_t[time_point][current_slice[0]]
                ax.imshow(slice_data, cmap='gray', interpolation='nearest', vmin=lower_bound,
                     vmax=upper_bound)
                # Recreate isolines using stored data
                X, Y, Z = isoline_data[time_point][current_slice[0]]
                CS = ax.contour(X, Y, Z, levels=[40, 60, 80], colors=['blue', 'green', 'red'
                    ], linewidths=[3,3,3])
                ax.clabel(CS, inline=True, fontsize=20)
                ax.set_title(f'Slice␣of␣scan␣{time_point}␣-␣Slice␣{current_slice[0]}')
                ax.axis('off')
            slice_index_text.set_text(f'Slice␣Index:␣{current_slice[0]}')
            fig.canvas.draw_idle()
        # Initial plotting
        for i, (time_point, _) in enumerate(sorted_temperature_maps):
            ax = axs[i]
            slice_data = self.volume_t[time_point][initial_slice_index]
            ax.imshow(slice_data, cmap='gray', interpolation='nearest', vmin=lower_bound,
                vmax=upper_bound)
            # Recreate isolines using stored data
            X, Y, Z = isoline_data[time_point][initial_slice_index]
            CS = ax.contour(X, Y, Z, levels=[40, 60, 80], colors=['blue', 'green', 'red'],
                linewidths=[3,3,3])
            ax.clabel(CS, inline=True, fontsize=20)
            ax.axis('off')
        fig.canvas.mpl_connect('scroll_event', update_slice)
        plt.figlegend(['40°C', '60°C', '80°C'], loc='lower␣center', ncol=3, labelspacing=0.)
        plt.show()

    def plot_temp_overlay(self, initial_slice_index=65):
        # Function to extract the numerical part for sorting
        def extract_number(time_point):
            match = re.search(r'S(\d+)', time_point)
            return int(match.group(1)) if match else 0

        if C.thermometry_method == 'PD':
            self.volume_t = self.monoE
        #W/L settings for HU map and overlay
        window_width = 400
        window_level = 60
        lower_bound_hu = window_level - (window_width / 2)
        upper_bound_hu = window_level + (window_width / 2)
        window_width = 80
        window_level = 50
        lower_bound_T = window_level - (window_width / 2)
        upper_bound_T = window_level + (window_width / 2)

        rowcol = math.ceil(np.sqrt(len(self.temperature_maps)))
        fig, axs = plt.subplots(rowcol, rowcol, figsize=(20, 20))
        axs = axs.flatten()  # Flatten the 2D array of axes
        # Sort temperature maps for each time point
        sorted_temperature_maps = sorted(self.temperature_maps.items(), key=lambda x:
            extract_number(x[0]))
```

```
        ax_counter = 0
        # Iterate over the sorted temperature maps
        for i, (time_point, temperature_map) in enumerate(sorted_temperature_maps):
            ax = axs[ax_counter]
            slice_data = self.volume_t[time_point][initial_slice_index, :, :]
            im1 = ax.imshow(slice_data, cmap='gray', interpolation='nearest', vmin=
                lower_bound_hu, vmax=upper_bound_hu)
            windowed_temperature_map = np.clip(temperature_map[initial_slice_index, :, :],
                lower_bound_T, upper_bound_T)
            # Create an alpha mask for where the temperatuer exceeds 30 degrees
            alpha_mask = np.zeros_like(windowed_temperature_map)
            alpha_mask[windowed_temperature_map > 30] = 0.55  # Inner pixels with 75% opacity
            # Overlay the temperature map onto the volume_t slice with the alpha mask
            im2 = ax.imshow(windowed_temperature_map, cmap='OrRd', interpolation='nearest',
                alpha=alpha_mask)
            ax.axis('off')
            ax_counter += 1
        # Add one colorbar for the whole figure, referencing the last image plotted
        fig.subplots_adjust(right=0.85, wspace=0, hspace=0)
        cbar_ax = fig.add_axes([0.87, 0.15, 0.05, 0.7])
        norm = plt.Normalize(vmin=lower_bound_T, vmax=upper_bound_T)
        sm = plt.cm.ScalarMappable(cmap='OrRd', norm=norm)
        plt.tight_layout(rect=[0, 0, 0.85, 1])
        plt.show()


# declare all constants for CT phantom analysis
thermometry_method = 'HU'
monoE_level = 70
DLMAR = True
O_MAR = False
slice = 2
increment = 1 #always keep on 1

ref_scan_path = '/path/to/reference/scan'
root_path = '/path/to/repetition/folder'  # Path to the folder containing CT scans
temperature_sensor_path = '/path/to/temperature/sensor/data'
output_path = os.path.join(root_path, 'scan_summary')

# thresholds for segmenting temperature sensors and ablation needle
lower_thresh_1 = 200 #sessie 1: 700, sessie 2: 200
upper_thresh_1 = 600 #sessie 1: 1200, sessie 2: 600
lower_thresh_2 = 1100 #sessie 1: 1500, sessie 2: 1100
upper_thresh_2 = 4000 #sessie 1: 4000, sessie 2: 4000
# thresholds for liver tissue
lower_threshold_liver_HU = 10 #HU
upper_threshold_liver_HU = 80 #HU
lower_threshold_liver_PD = 0.7 #g/mL
upper_threshold_liver_PD = 1.2 #g/mL
lower_threshold_liver_mu = 0.16
upper_threshold_liver_mu = 0.24
# thresholds for temperature analyzer with ROIs
lower_temp_threshold = 0
upper_temp_threshold = 150

# Alpha and beta fitted on rep1 - rep3
alphaHU, alphaHUsd = -0.3814688, 0.008819
betaHU, betaHUsd = 0.306405, 0.46975
alphaPD, alphaPDsd = 0.000390252, 0.000026
betaPD, betaPDsd = 0.99986339, 0.000544375
```

B

Literature Review

Computed Tomography Thermometry for Ablation Zone Monitoring in Liver Tumor Ablation: Technical Principles and Challenges

Lennart R. Koetzier[a,b]

[a]*Department of Radiology and Nuclear Medicine, LUMC, Leiden, The Netherlands,*
[b]*Faculty of Mechanical, Maritime and Materials Engineering, TU Delft, Delft, The Netherlands,*

Abstract

Thermal ablation for liver tumors necessitates precise monitoring of the ablation zone to ensure treatment efficacy and minimize risks. Traditional monitoring methods like MRI and ultrasound face limitations in cost, accessibility, and precision, especially in deep-seated or complex tumors. Computed Tomography (CT) thermometry emerges as a promising alternative, offering real-time, non-invasive and accurate monitoring of tissue temperature changes during ablation. Utilizing the inverse relationship between photon attenuation and tissue temperature, CT thermometry can provide valuable feedback to visualize the ablation zone. Various approaches to CT thermometry, including conventional and spectral CT, are explored, where spectral CT showing particular promise due to its enhanced precision and reproducibility. However, challenges such as variability in thermal sensitivity across patients, motion artifacts, and artifacts from metal ablation needles persist. Addressing these issues may involve using metal artifact reduction techniques and using spectral CT capabilities. This review provides an overview of the current state and challenges of CT thermometry in thermal ablation, delving into various CT-based temperature monitoring methods, experimental protocols for assessing CT thermometry's sensitivity and accuracy, and strategies for mitigating metal artifacts induced by ablation needles.

Keywords: CT thermometry, thermal ablation, ablation zone monitoring, noninvasive thermometry

1. Introduction

Thermal ablation is a minimally invasive technique that employs thermal energy to treat hepatic lesions. This technique is regarded as a potential first-line therapy for patients with small hepatocellular carcinomas, or as an alternative option for patients who are ineligible for surgical resection or have not responded to chemotherapy (1). A typical ablation system consists of an energy generator and a needle-like electrode that delivers thermal energy percutaneously to the target tumor, causing coagulative tissue necrosis. For instance, radiofrequency ablation (RFA), microwave ablation (MWA), high-intensity focused ultrasound (HIFU), and laser induced thermal therapy (LITT) aim to heat the tissue to the cytotoxic threshold of at least 60°C. Alternatively, cryoablation cools the tissue to -40°C or lower to cause necrosis (2).

The interventional radiologist usually relies on image guidance, such as computed tomography (CT), magnetic resonance imaging (MRI) or ultrasound imaging to accurately position the electrode in the target tumor (3; 4; 5). To evaluate the success of tumor ablation in the liver, it is essential to monitor the ablation zone, which is the region that has reached a temperature of at least 60°C or -40°C. Besides electrode positioning, imaging assists the physician during and after the procedure to detect any residual tumor or collateral damage to healthy tissue (6; 7). The ablation zone is commonly monitored based on differences in perfusion that are caused by coagulative necrosis. First, a multi-phase pre-ablation scan with a contrast agent is made with CT or MRI to visualize the tumor. After ablation, another multiphase contrast enhanced scan is made to verify non-enhancement of the ablated tissue, suggesting a successful ablation. However, the postprocedure ablation zone can be poorly displayed; challenges in identifying local recurrences include identification of original tumor position and non-enhancement in the border region of ablation necrosis. Partly due to these challenges, tumor progression and local recurrence rates remain higher than acceptable (8). Alternatively, ultrasound can be used but has several disadvantages such as blind spots, gas bubble interference, and low spatial resolution, which make it impractical for ablation zone monitoring (9).

As an alternative to perfusion imaging, tissue temperature can be directly monitored. MRI-based thermometry, for example, is currently the most widely employed non-invasive method for this purpose (10). While effective, interventional MRI is rarely applied due to high costs and the necessity for metal-free instruments. CT presents an cost-effective alternative that is already integral to intervention planning and probe positioning. CT-thermometry utilizes the inverse relationship between CT attenuation and tissue temperature. In this method, heating or cooling causes a change in tissue density, measurable through changes in Hounsfield Unit (HU), thus providing thermal feedback to the physician (11). Furthermore, in-room CT imaging is especially suitable for thermal ablation due to its speed, high spatial resolution, and the capability to depict tumors using contrast enhancement.

The concept of CT-thermometry is not new; its potential for non-invasive temperature monitoring was already explored in the seventies and early eighties (12; 13). These studies demonstrated a temperature resolution of a fraction of degree Celsius with a spatial resolution of 1 cm. But, at that time, CT measurements were not reliable due to unstable CT values and this application was not further developed until 1997 (14). In that year, Jenne and colleagues proposed CT-thermometry as a method for monitoring tumor ablation with HIFU (15). However, the reproducibility of CT values was still insufficient and thermal ablation was not widespread. It wasn't until the introduction of large multi-row detectors that CT-thermometry began to gain renewed attention (16). Meanwhile, Frich *et al.* outlined essential criteria for making non-invasive thermometry clinically viable, as summarized in table 1.

In 2011, Pandeya *et al.* studied RF ablation on ex-vivo bovine livers using a 128-slice scanner. They found a clear inverse relationship between CT value and temperature with a spatial resolution of 1.2 mm (17). More recently, Pohlan's team examined CT-thermometry's diagnostic accuracy in MWA and CA procedures on ex-vivo porcine livers. They reported an 89.2% predictive temperature accuracy for MWA, which dropped to 65.3% for CA (18). A recent development in CT-thermometry is the use of spectral CT, showing potential to monitor temperature non-invasively with higher precision (19; 20; 21).

Despite meeting most established criteria from table 1, CT-thermometry sees limited clinical use (22). Its reproducibility cannot be guaranteed due to factors such as interscanner variability or patient-specific differences. Another main factor limiting the reproducibility of CT-thermometry is the presence of metal artifacts induced by the ablation needle (23). These artifacts affect CT values and result in dark and bright streaks around the metal object (24).

This review provides an overview of the current state and challenges of CT-thermometry for thermal ablation. The review covers the following topics:

- What are the different methods of temperature monitoring based on CT, such as with conventional or spectral CT, and their advantages and disadvantages?
- What protocols are used for designing and conducting experiments to evaluate the sensitivity, accuracy, and precision of CT-thermometry, including the choice of phantom materials, temperature sensors, and scanning parameters?
- What are possible solutions to mitigate the metal artifacts caused by ablation needles, such as applying artifact reduction algorithms or using spectral CT?

After reading, the reader should be equipped with the knowledge necessary to identify future research opportunities that aim to enhance patient outcomes, reduce costs associated with thermal ablation procedures, and alleviate the workload on physicians.

2. Methods

This systematic review and meta-analysis were performed according to the Preferred Reporting Items for Systematic Reviews and Meta-Analyses (PRISMA) guidelines (25).

Parameter	**Requirement**
Temperature precision	<1–2°C
Spatial resolution	<1–2 mm
Acquisition time	<10–30 seconds
Three-dimensional temperature mapping	
Measurements presented in real time	
Insensitive to motion artifacts	
Compatible with medical equipment	
Radiation exposure from repeated CT measurement needs to meet safety standards.	

Table 1: Essential criteria for effective CT thermometry in ablation procedures (6).

2.1. *Literature search*

PubMed was searched to find studies that describe (I) CT-thermometry methods, (II) ablation zone monitoring using phantoms, and (III) CT needle artifact reduction methods. For each topic a single search string was used and results were exported to a reference manager (Zotero 6.0, Corporation for Digital Scholarship, Fairfax, VA, US):

I ("Tomography, X-Ray Computed" OR "Computed Tomography" OR "CT") AND ("Thermography" OR "Thermometry" OR (("Thermal" OR "Temperature") AND ("Map" OR "Sensitivity" OR "Monitoring" OR "Assess*" OR "Measu*")) OR "Physical Density").

II ("Radiofrequency Ablation" OR "Ablation Techniques" OR "Microwave Ablation") AND ("Thermal" AND ("Phantoms, Imaging" OR "Tissue-mimicking" OR "Thermochromic")) AND ("Liver" OR "Hepat*").

III ("Tomography, X-Ray Computed" OR "Computed Tomography" OR "CT") AND ("Metal Artifact" OR "Needle Artifact") AND ("Needle" OR "Antenna" OR "Probe" OR "Ablation Techniques" OR "Interventio*").

The complete search strings are described in Appendix Appendix A. No beginning search date was set; the literature search was updated until September 23, 2023.

2.2. *Exclusion criteria*

The titles, abstracts, and full-text of all studies were screened by one researcher. Studies not in English were excluded.

2.2.1. *CT thermometry methods*

Studies were excluded if the title clearly indicated that CT thermometry or CT physical density measurement was not described. The exclusion criteria for abstract from search string

(I) were as follows: (1) no temperature or physical density measurement performed; (2) CT not used for temperature measurement; (3) CT not used for physical density measurement; and (4) no X-ray CT used. The exclusion criteria for full-text eligibility were as follows: (1) no CT values, SNR, or CNR described and (2) no DLR on abdominal organs described.

2.2.2. *Ablation zone monitoring using phantoms*

Studies were excluded if the title clearly indicated that thermal ablation with a liver or thermochromic phantom was not described. The exclusion criteria for abstract from search string (II) were as follows: (1) no temperature verification performed; (2) phantom not thermochromic; (3) no imaging performed; and (4) in-vivo experiments. The exclusion criteria for full-text eligibility were as follows: (1) no liver phantom described and (2) no thermochromic phantom described.

2.2.3. *CT needle artifact reduction methods*

Studies were excluded if the title clearly indicated that CT metal artifact reduction was not described. The exclusion criteria for abstract from search string (III) were as follows: (1) no metal artifact reduction performed; (2) no needle artifacts described; and (3) no CT used.

3. Results

The combination of three search strings resulted in 699 records. From these records, 62 records were included in this review.

3.1. *Principles of computed tomography attenuation*

Computed tomography uses X-ray photons to build cross-sectional slices of the body. These slices are reconstructed from the attenuation coefficient measured after the photons passed through the body. At photon energy levels used in CT imaging (40 - 140 keV), the mass attenuation coefficient (μ_m) of a compound is largely determined by Compton scattering, while to a lesser extent by the photoelectric effect and Rayleigh scattering. Compounds with higher atomic numbers (Z) have a greater probability of photon interaction, leading to higher mass attenuation coefficients. This is particularly notable at lower photon energies where the photoelectric effect dominates, and attenuation is highly dependent on the third to fourth power of the atomic number (Z^3 or Z^4). The photoelectric effect is the main source of image contrast in x-ray imaging, as it varies with the atomic number of the material. Different tissues in the body have different atomic numbers, and thus different absorption probabilities for x-rays.

The Compton effect is dominant above ~ 30 keV photons in human tissues. The μ_m for Compton scattering is independent of Z, decreases slowly with photon energy, and is directly proportional to the mass electron density (ρ_e). The Compton effect does not produce much contrast between tissues and degrades the image quality by causing noise and scatter. In CT imaging, we measure the linear attenuation coefficient μ, which is dependent on μ_m and physical density ρ (the mass m divided by the volume V):

$$\mu = \mu_m \times \rho \tag{1}$$

A CT scan produces a volume that consists of a matrix of voxels, each representing the average X-ray attenuation coefficient of the material within the corresponding voxel. To obtain the CT value of a voxel, expressed in HU, the linear attenuation coefficients of all voxels are scaled:

$$HU = 1000 \times \frac{\mu(x, y, z) - \mu_{water}}{\mu_{water}}, \tag{2}$$

where μ_{water} is the linear attenuation coefficient of water at room temperature, and $\mu(x, y, z)$ is the average linear attenuation coefficient of voxel (x,y,z).

The X-ray tube emits photons with a range of energies and the attenuation measurement is integrated, throwing away all the energy dependence of a specific material. This can cause two different materials to have the same CT value, making it

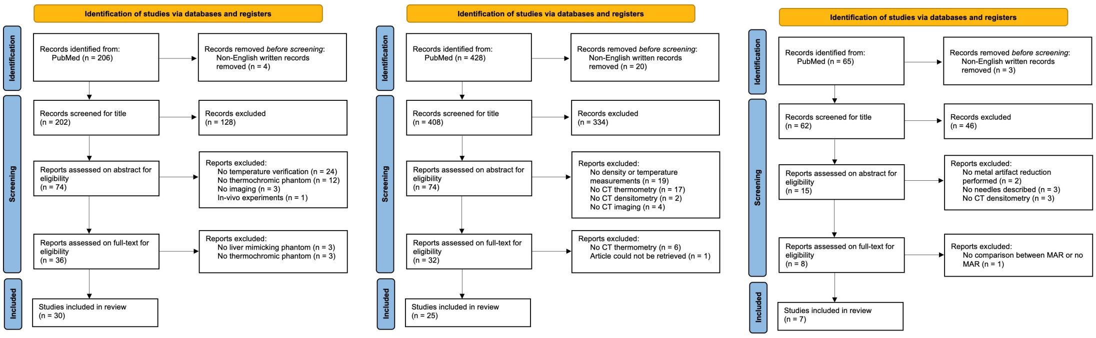

(a) Flow diagram for studies on methods for CT thermometry. Studies were found using search string (I).

(b) Flow diagram for studies on ablation zone monitoring using phantoms. Studies were found using search string (II).

(c) Flow diagram for studies on metal artifact reduction for needles. Studies were found using search string (III).

Figure 1: Flow diagrams for search string (I), (II), and (III).

difficult to distinguish them. Spectral CT, however, can improve the material discrimination and enable new clinical applications.

3.1.1. *Spectral CT*

The general idea of spectral CT was first described by Alvarez and Macovski (26). It uses a material's energy dependence, by differentiating between materials based on their weighting photoelectric effect and Compton scattering:

$$\mu(E) = \alpha_{PE} f_{PE}(E) + \alpha_{CS} f_{KN}(E), \tag{3}$$

where α_{PE} and α_{CS} are material specific coefficients that we would like to determine. $f_{PE}(E)$ is closely approximated by $1/E^{3.2}$ while $f_{KN}(E)$, defined as the Klein-Nishina function approximates the Compton effect and only depends on the photon energy. To determine the contribution of these effects to attenuation, in spectral CT, a second attenuation measurement is performed with photons of a different energy. The attenuation coefficients at low energy (E_L) and high energy (E_H) can be expressed as the attenuation contributions from a predefined combination of basis materials:

$$\mu(E_L) = \alpha_{PE} f_{PE}(E_L) + \alpha_{CS} f_{KN}(E_L) \tag{4}$$

$$\mu(E_H) = \alpha_{PE} f_{PE}(E_H) + \alpha_{CS} f_{KN}(E_H) \tag{5}$$

Because all photon energy dependent parameters are known, α_{PE} and α_{CS} can be accurately determined. Because these coefficients are the basis of attenuation, several mappings can be constructed from them. This includes virtual monochromatic images (VMI), where images represent attenuation at a single photon energy, effective atomic number (Z_{eff}), and material decomposition, where mappings of two basis materials can be constructed.

For monoenergetic x-ray sources, the energy spectra of different materials are known. However, in practice the x-ray tubes in CT scanners produce a polychromatic spectrum due to bremsstrahlung with k-edges at characteristic values. Alvarez and Macovski have shown that, despite the polychromatic spectrum of the x-ray tube, it is still possible to separate attenuation coefficients into their contributions from photoelectric and Compton effects. For a more in-depth review of approaches to obtain spectral data and clinical applications, we refer to an excellent review by McCollough *et al.* (27).

3.2. *CT thermometry methods*

The search resulted in 428 studies. After title screening, 354 articles were excluded. Then, abstracts were screened, and 42 more studies were excluded based on the predetermined exclusion criteria. There were several studies excluded based on more than one criterion. As a result, a total of 32 studies were full text reviewed. Among them, 7 studies were excluded because no CT thermometry was performed. Finally, 25 articles were included in the systematic review (Figure 1a). We also found 4 studies that reviewed non-invasive thermometry in general or specifically CT thermometry.

3.2.1. *Principle of thermal expansion*

The theory of thermal expansion is well understood; when a material is heated, its physical density is commonly reduced. This is expressed as:

$$\rho(T) = \frac{\rho(T_0)}{1 + \alpha\, \Delta T}, \tag{6}$$

where T_0 is the calibration temperature, $\Delta T = T - T_0$, and the thermal expansion coefficient is denoted by α. At an atomic level, this reduction in density can be attributed to the increased vibrational energy of atoms. As temperature rises, atoms vibrate more actively due to the increased thermal energy, causing them to occupy more space. This increase in the separation between atoms leads to a decrease in the material's density. These relationships, as visualized in figure 2, explain the phenomenon of a decreasing CT value with increasing temperature and are the basis of CT thermometry.

The influence of temperature on CT numbers was already investigated by Bydder and Kreel in 1979 to analyze the effects of temperature on the calibration process of CT scanners (13). Until the introduction of spectral CT, temperature measurements relied solely on changes in CT attenuation (11). Spectral CT, however, offers a new method to measure physical density with greater accuracy. The following sections will explain these two methods in detail.

3.2.2. *CT attenuation-based*

The temperature dependence of CT attenuation can be derived from the effect of thermal expansion on density. As shown

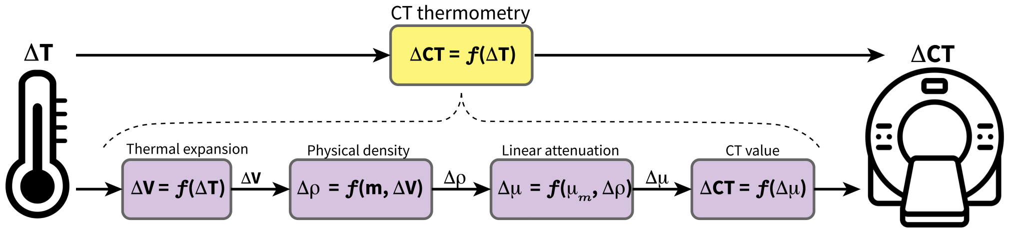

Figure 2: Schematic representation of the basic principles behind CT thermometry, illustrating the process from thermal expansion to CT value determination. The sequence involves transformations from temperature change (ΔT) to volume change (ΔV), physical density change ($\Delta\rho$), and linear attenuation change ($\Delta\mu$), finishing in the derivation of the CT value (ΔCT). Each transformation is influenced by specific parameters, indicating the relationship between the parameters.

in Figure 2, as temperature increases, density decreases, resulting in lower attenuation at higher temperatures. Thus, the following equation can be used to express the CT value at a given temperature relative to a reference temperature (T_0):

$$HU(T) \approx HU(T_0) - \frac{1000\,\mu(T_0)\,\alpha\,\Delta T}{\mu_{water}}. \tag{7}$$

By simplifying this equation and using a linear Taylor series expansion as proposed by Homolka *et al.* (28), the change in CT value due to temperature can be approximated as:

$$\Delta HU(T) \approx -[1000 + HU(T_0)]\,\alpha\,\Delta T. \tag{8}$$

This expression shows that temperature changes can be approximated by monitoring the CT values during an ablation. To examine how local temperatures affect the CT number, a regression analysis is conducted on the CT values and the corresponding temperature measurements. Multiple studies have investigated a linear relationship under varying circumstances, such as ablation method or imaging protocol and found temperature sensitivities ranging from -2.00 to -0.23 HU/°C for thermal heating (Figure 3). The slope of the fitted curve indicates the sensitivity of the attenuation-based CT thermometry and varies depending on the material/tissue that is studied: a larger slope reflects a higher thermal expansion coefficient α, which causes a greater change in CT numbers with temperature. However, some studies have reported that the temperature sensitivity is not constant with large temperature variations, implying that α is a function of temperature. These studies suggest that quadratic (29; 30), cubic (31) or exponential (32; 33) models fit the experimental data better than the linear model. These studies also suggest that tissue heating and cooling affect the CT numbers differently.

Although attenuation-based CT thermometry is based on a simple concept, it has a significant challenge: different tissues, patients, and scanning protocols have different thermal sensitivities. These sensitivities are difficult or impossible to measure in-vivo, and they are substantially different from the ex vivo measurements that are done under different physiological conditions. Also, the thermal properties of the target region may be altered by the intense heat during thermal ablation, which may introduce further errors (11). To address this issue, some studies have proposed to use VMI acquired with spectral CT (20; 21; 34). With VMI, new parameters are available to modulate the temperature sensitivity. Moreover, the linear correlations of CT attenuation with temperature are more pronounced at lower VMI energy levels, resulting in better separation between ablation zone and surrounding tissue (34). However, separate calibration curves, depending on the tissue and VMI energy level, are also required. Recently, Wang *et al.* used improved material decomposition capabilities of photon counting CT to develop a deep learning-based thermometry tool (35). Although the tool was tested on non-anthropomorphic materials, results showed a mean absolute error of 3.40°C. Further research is needed to determine if either photon counting CT or deep learning-based thermometry is promising for the future.

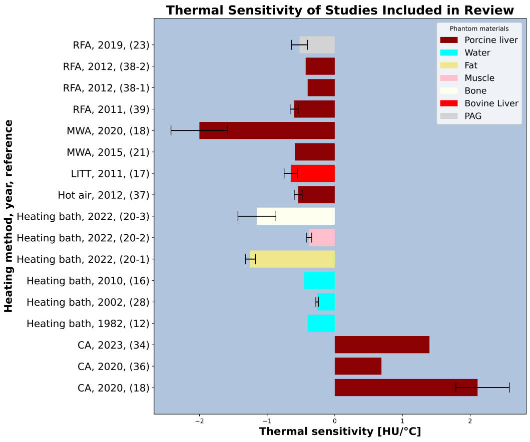

Figure 3: Variability in temperature sensitivity between several materials determined with attenuation-based thermometry. The included studies used different methods to heat or cool the material (34; 20; 18; 36; 23; 21; 37; 38; 39; 17; 16; 28; 12).

3.2.3. *Physical density-based*

As can be seen in figure 2, CT values not only reflect changes in temperature, but also changes in mass attenuation coefficient that result from changes in tissue composition. Moreover, the scanner model and tube voltage influence the conventional HU, along with the patient size. These factors result in considerable variations in the thermal sensitivity values reported in prior studies (Figure 3). While a linear relationship has been used to model the dependence of attenuation on temperature with conventional CT, spectral CT can be used to develop more reproducible quantitative models by extracting material specific coefficients, α_{PE} and α_{CS}. Spectral quantifications not only provide more consistent and quantitative measures for diagnosis, but combining spectral maps can also be used to estimate other quantities, such as physical density. This could also extend the application of spectral results to interventional procedures.

The Alvarez-Macovski model (26) has been used in various simplified forms for the development of density mappings, mainly for non-clinical purposes (40). One of these models is the Alvarez-Macovski physical density (AM-PD) model. It models the material specific coefficients α_{PE} and α_{CS} as follows:

$$\alpha_{PE} = K_1 \frac{\rho\,Z^n}{A} \tag{9}$$

$$\alpha_{CS} = K_2 \frac{\rho\,Z}{A}, \tag{10}$$

where K_1, K_2 and n are known constants. Combining with equation (3) results in the following relationship between attenuation coefficient and physical density:

$$\mu(E) = \frac{\rho}{A}\,[K_1 \frac{Z^n}{E^3} + K_2\,Z\,f_{KN}(E)], \tag{11}$$

where E is the photon energy in keV and f_{KN} is the dimensionless Klein-Nishina function. Furthermore, physical density of a single element can be related to electron density by the ED-PD model:

$$\rho_{ed} \sim \rho \, \frac{N_A}{A} \, Z, \tag{12}$$

where N_A is the Avogadro constant.

The research group of Noël has used these relationships to build four physical density models that rely on VMI, Z_{eff}, and ED maps, that are clinically available on spectral CT scanners (42). Z_{eff} is computed on the scanner by comparing the measured α_{PE} and α_{CS} with materials with known α_{PE}, α_{CS} and Z_{eff}. The effective atomic mass, A_{eff}, is not available on most clinical scanners and was obtained by fitting a third-order polynomial between the atomic mass and number of the first 30 elements (H, He, Li, etc.), which yielded a good approximation. By combining these variables, the following models for physical density were used:

$$\text{(AM-PD)}: \quad \rho = \frac{A_{eff} \, \mu(E)}{\frac{K_1 \, Z_{eff}^{n}}{E^3} + K_2 \, Z_{eff} \, f_{KN}(E)}, \tag{13}$$

$$\text{(ED-PD)}: \quad \rho = \frac{\rho_{ed} \, A_{eff}}{N_A \, Z_{eff}}. \tag{14}$$

Additionally, this group utilized parameterized versions of the AM-PD and ED-PD model to account for multi-elemental tissues and model assumptions, such as the exclusion of Rayleigh scattering influence. They proposed the following parameterized version of the AM-PD model using VMI of 70 keV:

$$\text{(p. AM-PD)}: \quad \rho = p_1 \frac{A_{eff} \, \mu^{p_2}(70keV)}{\frac{p_3 \, Z_{eff}^{p_4}}{70^{p_5}} + Z_{eff}^{p_6} \, f_{KN}^{p_7}(70keV)}. \tag{15}$$

The ED-PD model was parameterized as follows:

$$\text{(p. ED-PD)}: \quad \rho = p_8 \frac{\rho_{ed}^{p_9} \, A_{eff}^{p_{10}}}{N_A \, Z_{eff}^{p_{11}}}. \tag{16}$$

The parameters of both models (table 2) were fitted to 180 anthropomorphic tissues defined by the International Commission on Radiation Units and Measurements (ICRU) Report 44 with corresponding attenuation coefficients from the National Institute of Standard and Technology (NIST) XCOM (42). The authors validated the model using a phantom containing inserts with known density and found that the parametrized AM-PD model was the most accurate, with a root mean square error of 0.0007 g/mL. They decided to use this model for temperature monitoring in a follow-up study.

Parametrized AM-PD		Parametrized ED-PD	
p_1	3.48632	p_8	0.800168
p_2	1.0704	p_9	1.01325
p_3	46.8754	p_{10}	0.857102
p_4	4.1907	p_{11}	0.800386
p_5	2.94742		
p_6	1.01921		
p_7	0.995567		

Table 2: Parameters for parametrized AM-PD and ED-PD models (42).

Liu *et al.* evaluated the temperature sensitivity of the parameterized AM-PD model by heating ex-vivo bovine muscle in a warm water bath from 22 to 49.5°C (43). To establish the relationship between temperature and physical density variations, temperature verification was performed with invasive thermal sensors and equation (6) was applied. The authors demonstrated a high linear correlation (R = 0.98) between physical density and temperature with a thermal expansion coefficient 0.00042±0.00001 °C^{-1}. This means that a 10°C increase leads to a 0.42% decrease in physical density. The physical density dependence on temperature is visualized in figure 4.

In another follow-up study, this research group investigated how image noise influenced the temperature precision in 35 to 80°C conditions (19). They scanned a liver-mimicking phan-

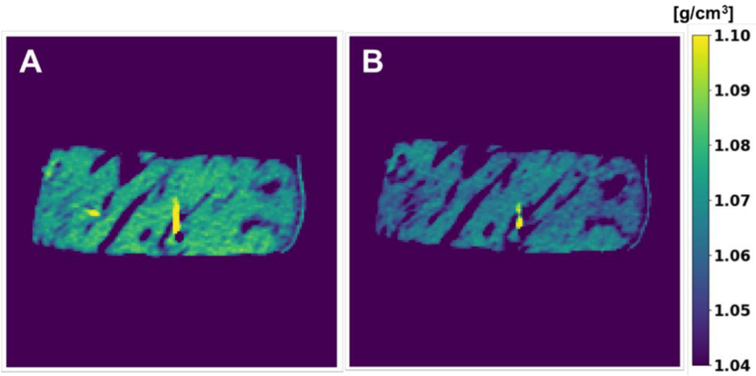

Figure 4: Physical density maps of ex-vivo bovine muscle in a water bath at 22 °C (A) and 45.5 °C (B). Physical density decreased with increased temperatures. The area of high physical density (yellow) corresponds to optical fiber temperature probes. These quantifications illustrate a strong relationship with change in temperature that corresponds to thermal volumetric expansion. Figure adapted from Liu *et al.* (41).

Phantom material	**Frequency**	**Temperature sensor**	**Frequency**
Ex-vivo tissue	12 (33; 44; 45; 46; 47; 48; 49; 50; 51; 52; 53; 54)	Thermocouple	9 (33; 45; 50; 54; 55; 56; 57; 58; 51)
Polyacrylamide gel	10 (23; 59; 45; 60; 55; 61; 62; 63; 64; 65)	Fiber optic	7 (59; 46; 48; 49; 53; 64; 66)
Agar	4 (47; 53; 56; 57)	Thermochromic ink	7 (23; 59; 45; 60; 61; 62; 64)
Silicone gel	3 (67; 50; 54)	Fiber Bragg grating	2 (68; 47)
Serum albumin	2 (33; 65)		

Table 3: Experimental setup materials, tissues, and temperature sensors for ablation zone monitoring with MWA, RFA, HIFU or LITT. The studies that used these materials are listed between brackets

tom with different radiation doses, slice thicknesses, reconstruction methods and denoising methods. Results show that without denoising but with a high level iterative reconstruction, they needed a CT dose index volume (CTDI$_{vol}$) of 30 mGy and a slice thickness of maximum 2 mm to achieve a precision of <3°C. However, with non-local means denoising, the radiation dose could be decreased to 2 mGy and still achieve this precision. Thus, they showed that additional denoising at low doses enhanced the temperature precision. Conversely, without denoising, a higher radiation dose was required to meet the clinical practice requirements of CT thermometry.

Although the parameterized AM-PD method has shown promise, its use during heating procedures with an ablation needle remains untested. This leaves open questions regarding the potential impact of gas bubbles or metal artifacts on physical density measurements. Addressing this knowledge gap may be possible by conducting a phantom experiment. Using metal artifact reduction software within this context could provide insights into the influence of the ablation needle.

3.3. Ablation zone monitoring using a phantom

The search resulted in 206 studies. After title screening, 128 articles were excluded. Then, abstracts were screened, and 40 more studies were excluded based on the predetermined exclusion criteria. As a result, a total of 36 studies were full text reviewed. Among them, 6 studies were excluded because no liver or thermochromic phantoms were used. Finally, 30 articles were included in the systematic review (Figure 1b). We also found 3 studies that reviewed chemical and thermal properties of materials that are commonly used for liver phantom fabrication. Table 3 provides an overview of the common phantom materials and temperature verification methods.

3.3.1. Liver phantom

Phantoms are used in research of medical imaging to replace real tissues and in studies where in-vivo models are inadequate. A phantom that mimics the temperature response of liver tissue to thermal ablation should be designed to match the liver's physical properties, which differ from those of other tissues such as bone, lung, and adipose. The physical properties that are relevant for the phantom include density, specific heat capacity, thermal conductivity, thermal diffusivity, specific absorption rate, electrical conductivity, and permittivity (69). In particular, when the phantom is used for CT imaging, density and photon attenuation properties should resemble real liver tissue. These properties influence the ablation zone's size and shape as well as its appearance after image acquisition. Additionally, practical considerations include that the phantom should be made from nontoxic materials, nondegradable over time, maintain its structure, and should be easy to handle (70).

Several materials have been used to fabricate liver phantoms, such as ex-vivo animal tissue polyacrylamide gel (PAG), agar(ose), and silicone gel. Each material has its advantages and disadvantages in terms of thermal similarity, repeatability, and puncture resistance, as well as cost, availability, and ease of preparation. Table 4 summarizes the main characteristics of these materials.

Ex-vivo tissue samples, obtained from freshly-excised animal organs, are commonly used to simulate human liver tissue in ablation procedures. Ex-vivo porcine or bovine liver tissue has similar thermal and dielectric properties to in-vivo human liver tissue, both in normal and tumor tissue (71; 72). However, these properties can change after multiple ablations as coagulation effects alter tissue structure and composition. It is therefore not recommended to perform repeated ablation procedures on the same tissue sample, as this reduces the reliability of the measurements. To prepare ex-vivo tissue samples, liver or muscle tissue from pigs, cows or swines are often readily available at local butchers and can be preserved in a cooled saline bath. Artificial tumors can also be added to the tissue to mimic different tumor sizes and shapes (44).

PAG is composed of acrylamide C_3H_5NO, which forms a gel when hydrated. PAG is a solid, optically transparent, and elastic material that can be easily shaped into the desired shape. This allows the creation of multilayered samples with different properties depending on the water concentration in each layer (73). Mikhail *et al.* evaluated PAG for ablation purposes and found that thermal properties (such as heat capacity and thermal diffusivity), electrical conductivity, and permittivity of the PAG-based phantom are similar to biological liver tissue (59). By sealing the phantoms to prevent water evaporation, the electrical and thermal characteristics of the PAG are stabilized. The phantoms should be stored in sealed glass tubes to maintain their integrity. PAG is suitable for phantom models because they are inexpensive, moldable, and insensitive to temperature variations (70). Furthermore, polyacrylamide has a high melting point, which is well-suited for RFA and MWA. The downsides of PAG are its neurotoxicity and limited shelf-life of about five months.

Material	**Density**	**Thermal similarity**	**Electrical similarity**	**Cost**	**Availability**	**Ease of preparation**
Ex-vivo tissue	++	+	+	+	+	+
Polyacrylamide	+-	+	+	+-	-	-
Agar	+-	+	+-	++	+	+
Silicone	+	-	–	+-	-	-

Table 4: Comparison of phantom material properties.

Agar and agarose gel are polysaccharide-based gels, often extracted from certain red seaweeds. Agarose is one of the two main components of agar, along with agaropectin, but it is less commonly used than agar. Thermal and dielectric properties of agar similar to those of liver tissue can be obtained with a concentration of 2.5% agar (74). Agar gel is easy to shape and manipulate by temperature control, and it can cool rapidly at room temperature, which enhances its reproducibility (70). However, agar is a hydrophilic, organic material that is prone to microbial growth, which can affect its thermal and dielectric properties over time. Another limitation of agar gels is their low stability at high temperatures, which restricts their applicability for high temperature ablations (> 80°C) (69).

Silicones are polymers with a silicon-oxygen backbone and various organic side groups. They have high mechanical strength, thermal stability, and are easy to fabricate. Therefore, they are suitable for making phantoms that can mimic the shape and hydration of blood vessels (70). Although one study recently introduced a silicone-based phantom mimicking thermal properties of soft tissue, this material remains underexplored for MWA or RFA (67).

3.3.2. *Temperature verification*

The aim of thermal ablation is to reach a temperature of at least 60°C or -40°C for cell death. There are two main methods to verify the temperature around the ablation center. The first method uses small thermometer probes to invasively measure the tissue's local temperature. Alternatively, a thermally sensitive phantom can be used to produce a visible and measurable ablation zone.

The invasive method uses small thermometer probes that are inserted into the tissue at different distances from the ablation center. These probes can measure the local temperature of the tissue with high accuracy and precision. However, they have some drawbacks, such as interfering with the thermal therapy and the imaging modality, and being affected by strains caused by thermal expansion or patient movement (10). There are three main types of invasive temperature sensors: thermocouples, optical fiber sensors, and fiber Bragg gratings.

Thermocouples are small devices that consist of two dissimilar metal wires joined at one end, forming a junction. The junction generates a voltage that is proportional to the temperature difference and is measured by a dedicated instrument that converts it into a temperature reading. Multiple thermocouples can be used to monitor the temperature near an ablation probe by inserting them at fixed distances from the probe. This allows the real-time observation of the thermal effects of ablation on the surrounding tissue with sub-degree precision (29; 45). Thermocouples are often made of a metallic material, and therefore may affect the current distribution of RFA in a way that does not occur during a real ablation procedure. Additionally, imaging metal artifacts can be induced, especially in CT imaging.

Optical fiber sensors are based on the principle of light reflection and refraction in a fiber optic core. Temperature measurement with these sensors is based on the fact that absorption and transmission properties of the fiber change with temperature. They offer significant advantages over thermocouples, such as smaller size, higher resistance to hysteresis, and lower self-heating. Moreover, fiber-optics enable high spatial resolution and thermal precision, reaching below 0.1 mm 1°C, respectively (75). Increasing application of optical fiber sensors is seen in the monitoring of ablation zones, although monitoring is progressing more towards non-invasive thermometry (46). More recently, fiber Bragg gratings, a subtype of fiber optical sensors, were introduced as an alternative to thermocouples (68; 47). Fiber Bragg gratings allow for multi-point measurements along the fiber, but they are sensitive to strain, which may cause measurement errors due to patient motion.

Another method to evaluate ablation zones is to add a thermally sensitive material to the phantom that changes visibly when it reaches a certain temperature. This approach allows measuring the size and shape of the ablation zone, which may vary due to internal or external factors such as tissue composition or ablation technique, instead of only measuring temperatures at specific points from the ablation probe. Moreover, it avoids using metallic thermocouples that can alter the ablation zone size and shape. Serum albumin is often used as a thermally sensitive additive, but it has a drawback of coagulating at a fixed temperature, which limits the information about the temperature gradient and the repeated use of the phantom (76). Alternatively, thermally sensitive ink can be added to create a color gradient that represents the temperature gradient in the phantom (60). A combination of methods may be optimal for monitoring ablation zones; first, the invasive method to understand the heat dynamics and gradient relative to the ablation zone, and second, the thermally sensitive phantom to examine the ablation zone details.

3.4. *Needle artifact reduction*

Metallic objects, such as dental fillings and orthopedic hardware, cause metal artifacts that appear as high and low attenuating streaks across reconstructed CT images. These artifacts degrade image quality by obscuring the metallic objects and the surrounding tissue, which may result in inaccurate diagnosis or missed findings (24). Metal artifacts also affect thermal ablation procedures, as they can impair the needle positioning and temperature monitoring as shown in figure 5. Metal artifacts are caused by several mechanisms, such as photon starvation and beam hardening, and are more pronounced when acquiring images with low tube current or voltage. To improve the image quality, several metal artifact reduction (MAR) algorithms have been proposed for different applications, such as dental fillings, surgical clips, coils or orthopedic hardware (77). However, few studies have specifically addressed MAR for ablation needles. Here, we review the general methods for MAR and then focus on MAR for needles.

3.4.1. Sinogram-based

Sinogram-based MAR algorithms aim to improve the quality of CT images with metallic objects by identifying and replacing the metal-corrupted regions in the sinogram with estimated values. The sinogram is an image that represents the raw data at multiple angles as measured by the detector and serves as input for image reconstruction. As Katsura *et al.* excellently reviewed sinogram-based MAR (77), we will provide a short recap. First, metal is identified either in the reconstructed image or the sinogram. Among commercially-available algorithms, the exact method may differ, yet the foundational approach remains similar, potentially extended by proprietary additional steps. Typically, the following steps are taken:

1. The metal object is segmented in the uncorrected CT image using a CT value threshold.
2. The segmented metal object is forwardprojected to find the artifacted-corrupted X-ray data in the sinogram.
3. The artifact-corrupted sinogram data is removed and replaced by interpolation based on the uncorrupted data.
4. The artifact-removed sinogram is backprojected to obtain the artifact-reduced image.

This process may be iterated until a point of convergence is reached. In general, this sinogram-based approach leads to an image that is consistent with the uncorrected image. However, the original image may contain severe artifacts, which makes segmentation difficult, and the interpolation may not restore the lost information completely. While initial artifacts are reduced, secondary interpolation artifacts may be introduced. Sinogram-based MAR is effective for correcting photon starvation, but it is less capable of correcting beam-hardening artifacts, which are better handled by spectral CT.

3.4.2. Spectral-based

Modern CT scanners have several options, such as beam filtration, calibration correction or dedicated beam hardening software, to reduce beam-hardening artifacts caused by high Z materials (24). The introduction of VMI with spectral CT has given physicians another method to reduce the effects of beam-hardening. As VMI should ideally imitate images that are acquired with photons of one energy level, the mean beam energy does not “harden” as it travels through tissue. Several studies have evaluated the capabilities of VMI for MAR at different energy levels and metallic implants (77; 79). VMI reconstructions at higher energy levels reduce beam-hardening artifacts as high-energy photons are far less susceptible to absorption in high Z materials (80). To reduce metal artifacts, VMI levels between 95 and 150 keV are effective. However, higher energy VMI also leads to less tissue contrast so there is a trade-off depending on the application (77). In another study, researchers combined sinogram-based iterative MAR with high-energy VMI and compared both methods with each other. They found that for severe artifacts caused by dental material, iterative MAR led to a much more pronounced artifact reduction than the use of VMI with higher keV levels (81).

3.4.3. Deep learning-based

More recently, deep learning-based MAR has been investigated. These algorithms predominantly fall into two categories: image-based algorithms and those that optimize in both the image and sinogram domains (82). Image-based algorithms remove primary metal artifacts or secondary interpolation artifacts, by feeding the artifact-corrupted image into a deep learning network (83). Alternatively, a deep learning network is used before image reconstruction to identify, remove, and replace sinogram data corrupted by metal. This network frequently introduces secondary artifacts in the image, different from interpolation artifacts, which are then removed by a subsequent network (84). The majority of MAR techniques are available as standalone frameworks for imaging metallic objects. Thus, dual domain MAR algorithms, which need sinogram input, are confined to CT scans where sinograms are available.

Several studies compared their deep learning MAR algorithm with various non-deep learning and other deep learning MAR algorithms, generally observing superior performance of deep learning MAR over sinogram-based MAR (82). For instance, Selles *et al.* developed a deep learning MAR algorithm for sacroiliac joint implants and compared it to a clinically available sinogram-based MAR algorithm (85). Their algorithm is trained on images of simulated metal artifacts and operates in the image domain. They found that both techniques significantly reduced metal artifacts, with deep learning MAR resulting in more reduction than sinogram-based MAR in most anatomical regions. Moreover, they propose the potential utility of their algorithm in combination with VMI to reduce beam-hardening artifacts in advance.

3.4.4. Metal artifact reduction for needles

The search resulted in 62 studies. After title screening, 46 articles were excluded. Then, abstracts were screened, and 8 more studies were excluded based on the predetermined exclusion criteria. There were several studies excluded based on more than one criterion. As a result, a total of 8 studies were full text reviewed. Among them, 1 study was excluded because MAR was applied but not compared to other MAR algorithms or no MAR. Finally, 7 articles were included in the systematic review (Figure 1c).

A limited number of studies have delved into the metal artifact effects of needles utilized in biopsy or ablation proce-

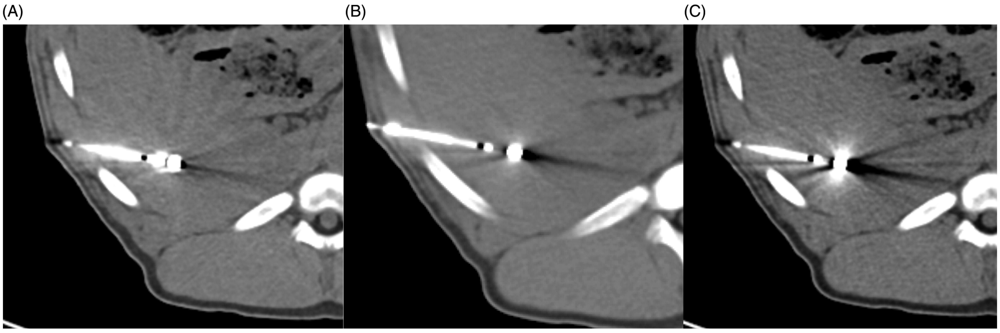

Figure 5: Metal artifacts in pig liver in proximity of a MWA probe. Artifacts leading to mild loss of visibility of liver tissue in proximity of the probe (A); Artifacts leading to moderate loss of visibility of liver tissue in proximity of the probe (B); Artifacts leading to complete loss of visibility of liver tissue in proximity of the probe (C) Figure adapted from Do *et al*. (78).

dures. The extent of needle artifacts in CT-guided procedures may be influenced by factors such as needle alloy, configuration, thickness or internal shape (86). Nevertheless, even with these factors taken into account, needle artifacts can still obscure surrounding tissue, thus hampering image interpretation (Figure 5). The research group of Do *et al*. explored the use of sinogram-based MAR, spectral MAR, and a hybrid approach in in-vivo pig models during biopsy and ablation procedures (87; 88; 78; 89; 90). We distilled their findings into several key conclusions:

I standalone sinogram-based MAR was more effective than spectral-based MAR (90);

II using their own artifact quantification method (89), the combination of 80 keV VMI and sinogram-based MAR was most effective (88);

III in a reader study, increasing keV energy level increased overall image quality and decreased artifact degree (88);

IV in a comparative study among MWA, RFA, and CA needles, sinogram-based MAR proved effective in MWA and CA, but not in RFA (87);

V sinogram-based MAR generated new artifacts such as blooming irregularities along the antenna edge and splay-like radiating stripes at the periphery, which were observed around the liver or abdomen's periphery, but not at the antenna tip or within the liver in the puncture direction (78).

The scope of these studies, however, was limited to a single type of sinogram-based MAR. It is possible that employing MAR algorithms from other vendors could yield varying results, highlighting the need for further comparative studies.

Wang *et al*. used a MAR algorithm which takes into account geometry of the scanner, noise, and anatomy, in a study involving 30 lung cancer patients undergoing MWA (91). Their findings showed that the MAR algorithm was capable of reducing MWA antenna-induced artifacts, both quantitatively and qualitatively. Despite this, a comparative analysis of different MAR algorithms was not conducted and additional research is needed to explore the potential of deep learning-based MAR in needle artifact reduction.

4. Discussion

4.1. Challenges

This review highlights several issues and challenges that need to be tackled before clinical implementation of CT-based thermometry, in particular for liver tumor ablation. A critical challenge lies in the variability of the thermal expansion coefficient (α) or temperature sensitivity across different tissues, tumor types, patients or scan parameters (38). Moreover, some studies found different temperature sensitivities for the same tissue under cooling and heating conditions (33). This variability complicates the generalization of findings and affects the accuracy of CT thermometry. Because of these issues, we might need custom settings for each patient. It would be difficult or impossible to obtain these highly personalized settings in-vivo, and there are substantial differences between in-vivo and ex-vivo measurements because of varying physiological conditions, such as perfusion. Although physical density-based thermometry reduces the influence of factors such as scanner model or tube voltage, large inconsistencies in thermal sensitivity values still exist between patients (92). It is therefore even more important to conduct studies investigating temperature sensitivities in a wide range of tissue and tumor types, patients, and temperatures.

In the time between consecutive CT scans, which may span several minutes during an interventional procedure, motion artifacts arising from breathing, organ movement, or patient positioning can misalign the scans. If the initial temperature reference scan becomes misaligned with later temperature scans, this can lead to significant errors in temperature measurement. To mitigate such artifacts, precise image registration of successive acquisitions is needed, although these often bring their own set of computational and time constraints (93). After registration, the interventional radiologist may find it useful to visualize the temperature map as an overlay on the pre-ablation contrast enhanced scan, as shown in figure 6. Alternatively, an automatic segmentation of the tumor can be used to determine what portion of the tumor has reached the critical 60°C temperature,

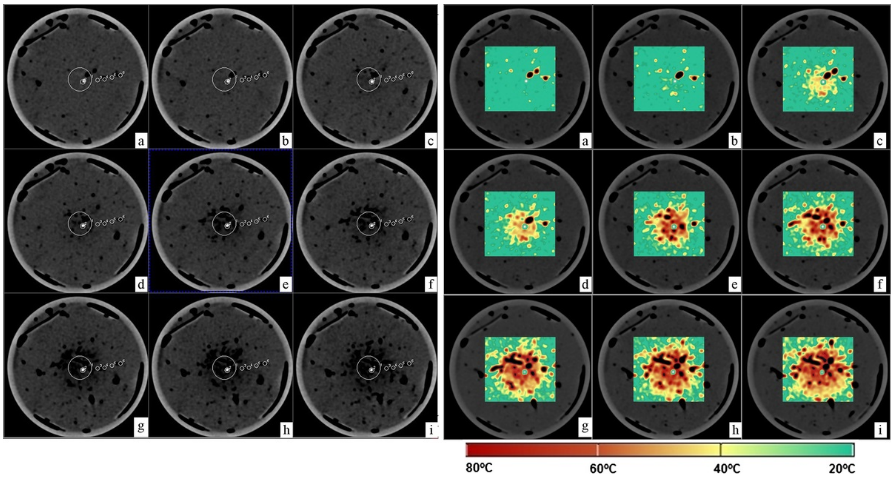

Figure 6: Example of CT scans (left) during RFA procedure in ex-vivo bovine liver tissue. The central circle shows the position of the ablation probe, and the other 5 circles show the location of thermal sensors. In subfigures (a) - (i) the temperature increases over time from 20°C to 98°C in the most proximal thermal sensor. The corresponding temperature maps are shown as overlay on CT scans (right). The temperature was visualized according to the temperature bar as indicated. Figure adapted from Pandeya *et al*. (17)

providing useful feedback for the physician. Real-time temperature maps lead us to an exciting area that could make CT-guidance during ablation much more useful in a clinical setting. Continued research and technological innovation in this domain are paramount for pushing the boundaries of what is currently achievable.

In clinical settings, the issue of radiation exposure from CT scans is always relevant. However, for liver cancer patients facing a poor prognosis (94), this concern may be less pressing. As Bruners *et al.* have pointed out, the priority often shifts towards achieving accurate and low-noise temperature measurements (38). Accurate measurements can help minimize the risk of incomplete ablation and reduce the likelihood of tumor recurrence, while the risk of radiation-induced tumors is small. Nonetheless, optimizing radiation dose remains a focus of ongoing research, particularly in the case of repeated scans. Ways to reduce the radiation dose are to optimize the acquisition, reconstruction, and post-processing parameters and limit the number of scans. However, sub-optimal parameters can result in image noise, which decreases the thermal-spatial resolution of temperature measurements. To this extent, efforts have been made to find the limits of these parameters (19; 20) but more prospective research is needed.

When it comes to metal artifact reduction, the scope of research appears limited to specific, often vendor-specific, algorithms. The effect of these algorithms is twofold: while they are able to reduce artifacts, they also risk altering the Hounsfield Units, potentially skewing temperature estimations. A comprehensive comparison among various MAR algorithms, therefore, stands as an unmet need in this field.

4.2. Comparative landscape and future directions

Within this web of challenges and considerations, CT thermometry finds itself competing with other temperature-monitoring techniques such as MRI and ultrasound-based thermometry (10; 95). MRI enables measurement of relative temperature changes in the body with a resolution of a few mm, temporal resolution of around 5 seconds, and a temperature precision of approximately 1°C and is currently regarded as the golden standard for non invasive thermometry. However, it comes with limitations in terms of cost, the need for MRI-compatible equipment, and sensitivity to changed tissue composition during coagulation (96). Ultrasound, though less expensive and real-time, suffers from operator dependency and may lack the necessary precision for deeper tumors. In this regard, CT thermometry emerges as a viable middle-ground option that balances cost, accessibility, and spatio-temporal resolution. However, direct comparative studies are vital for a more conclusive evaluation of its advantages and drawbacks.

Looking ahead, the spectral features of photon-counting CT (PCCT) hold promise for more accurate tissue characterization (97). The thermal expansion coefficient α is one of the main sources of inaccurate temperature measurements, and PCCT could offer a more precise determination of this variable. Alternatively, deep learning algorithms can be exploited during CT thermometry. The discovery of a nonlinear relationship between CT values and temperature in some studies indicates that data-driven modeling is suitable for CT thermometry. Deep learning algorithms can already detect pathologies from CT images (98), and in the future they might extract parameters, thermal expansion coefficient α or temperature, from a single dataset or even several multimodal datasets. Wang *et al.* already successfully utilized both PCCT and deep learning in CT thermometry (35). They demonstrated a data-driven thermometry algorithm that can accurately predict temperatures of unknown materials based on spectrally resolved linear attenuation coefficients from known materials at different temperatures. This has significant implications for ablation procedures, as it offers a method for determining tissue characteristics without the need for in-vivo calibration.

5. Conclusion

In summary, CT-based thermometry holds substantial promise for improving liver tumor ablation procedures, yet several challenges remain that limit its widespread clinical implementation. One critical concern revolves around the variability of the thermal expansion coefficient (α) across different tissues, tumor types, and patients. This variability complicates the standardization of CT thermometry and necessitates patient-specific settings that are challenging to obtain in-vivo. Equally, metal artifacts induced by the ablation needle can hamper accurate and precise temperature measurements as they introduce distortions in CT values.

While MRI and ultrasound-based thermometry present their own sets of advantages and limitations, CT thermometry positions itself as a balanced alternative. Future prospects include the incorporation of PCCT and deep learning algorithms. Both hold the potential to refine our understanding and application of thermal expansion coefficients as well as improving MAR algorithms. In conclusion, CT thermometry, despite its potential advantages and ongoing advancements, has its challenges. Solving these issues is paramount for the technology to move from the experimental phase into routine clinical practice.

6. Research plan spectral CT thermometry

Building upon the reviewed literature in this manuscript, our research plan is designed to address knowledge gaps in usage of spectral CT for thermometry during liver tumor ablation. We aim to refine the parametrized Alvarez-Macovski physical density (AM-PD) model to enhance the precision of temperature measurements during ablation procedures, especially considering the challenges posed by the presence of ablation needle-induced metal artifacts and the potential impact of gas bubbles.

Our methodology encompasses a series of phantom experiments, utilizing ex-vivo porcine liver to closely mimic liver tissue. These experiments are designed to simulate the thermal ablation process, using a microwave ablation needle to determine the influence of metal artifacts on temperature measurement accuracy. We will conduct these experiments using the Philips Spectral CT 7500, performing microwave ablations and acquiring CT scans at one-minute intervals under various settings. Temperature verification will be performed using invasive thermocouples.

A critical aspect of our approach is the use of higher energy levels of Virtual Monochromatic Images (VMI) as input in the AM-PD model to assess their efficacy in reducing metal artifacts and enhancing temperature measurement precision. As the initial parametrized AM-PD model was built on 70 keV VMI, we will reparametrize the model for other energy levels. Complementing this, we plan to explore the application of deep learning-based Metal Artifact Reduction (MAR).

The expected outcomes of our research are twofold: first, we aim to compare the precision and accuracy of the physical density based thermometry with attenuation-based thermometry in scenarios that involve an ablation needle. Second, we intend to demonstrate the effectiveness of high-energy VMI and deep learning-based MAR in mitigating metal artifacts, resulting in more reliable temperature data.

This research project spans over a 9-month period from September 2023 to May 2024. The literature review and research plan was covered in the first two months. Data collection, analysis, and development and evaluation of MAR software will be performed in the period November to April and is shown in figure 7.

References

[1] Crocetti, L., de Baére, T., Pereira, P. L., and Tarantino, F. P., "CIRSE Standards of Practice on Thermal Ablation of Liver Tumours," *Cardiovascular and Interventional Radiology*, vol. 43, no. 7, Jul. 2020.

[2] Nikfarjam, M., Muralidharan, V., and Christophi, C., "Mechanisms of Focal Heat Destruction of Liver Tumors," *Journal of Surgical Research*, vol. 127, no. 2, Aug. 2005.

[3] Knavel, E. M. and Brace, C. L., "Tumor Ablation: Common Modalities and General Practices," *Techniques in Vascular and Interventional Radiology*, vol. 16, no. 4, Dec. 2013.

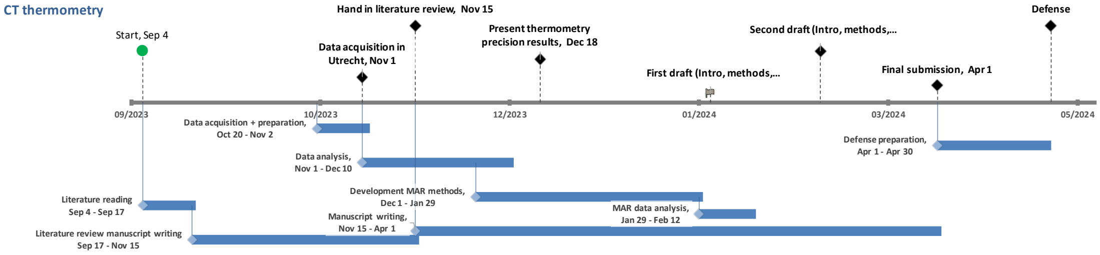

Figure 7: Timeline of the Spectral CT Thermometry project, detailing phases from literature review to final defense between September 2023 and May 2024. Key milestones include data acquisition, MAR methods development, and manuscript drafts, leading to the final submission and subsequent defense.

[4] Clasen, S., Rempp, H., Hoffmann, R., Graf, H., Pereira, P. L., and Claussen, C. D., "Image-guided radiofrequency ablation of hepatocellular carcinoma (HCC): Is MR guidance more effective than CT guidance?" *European Journal of Radiology*, vol. 83, no. 1, Jan. 2014.

[5] Crocetti, L., Della Pina, C., Cioni, D., and Lencioni, R., "Peri-intraprocedural imaging: US, CT, and MRI," *Abdominal Imaging*, vol. 36, no. 6, Dec. 2011.

[6] Frich, L., "Non-invasive thermometry for monitoring hepatic radiofrequency ablation," *Minimally Invasive Therapy & Allied Technologies*, vol. 15, no. 1, Jan. 2006.

[7] Goldberg, S. N., Grassi, C. J., Cardella, J. F., Charboneau, J. W., Dodd, G. D., Dupuy, D. E., Gervais, D., Gillams, A. R., Kane, R. A., Lee, F. T., Livraghi, T., McGahan, J., Phillips, D. A., Rhim, H., and Silverman, S. G., "Image-guided Tumor Ablation: Standardization of Terminology and Reporting Criteria," *Radiology*, vol. 235, no. 3, Jun. 2005.

[8] Violi, N. V., Duran, R., Guiu, B., Cercueil, J.-P., Aubé, C., Digklia, A., Pache, I., Deltenre, P., Knebel, J.-F., and Denys, A., "Efficacy of microwave ablation versus radiofrequency ablation for the treatment of hepatocellular carcinoma in patients with chronic liver disease: a randomised controlled phase 2 trial," *The Lancet Gastroenterology & Hepatology*, vol. 3, no. 5, May 2018.

[9] Zhou, Y., Yang, Y., Zhou, B., Wang, Z., Zhu, R., Chen, X., Ouyang, J., Li, Q., and Zhou, J., "Challenges Facing Percutaneous Ablation in the Treatment of Hepatocellular Carcinoma: Extension of Ablation Criteria," *Journal of Hepatocellular Carcinoma*, vol. 8, Jun. 2021.

[10] Saccomandi, P., Schena, E., and Silvestri, S., "Techniques for temperature monitoring during laser-induced thermotherapy: An overview," *International Journal of Hyperthermia*, vol. 29, no. 7, Nov. 2013.

[11] Fani, F., Schena, E., Saccomandi, P., and Silvestri, S., "CT-based thermometry: an overview." *International journal of hyperthermia : the official journal of European Society for Hyperthermic Oncology, North American Hyperthermia Group*, vol. 30, no. 4, Jun. 2014.

[12] Fallone, B. G., Moran, P. R., and Podgorsak, E. B., "Noninvasive thermometry with a clinical x-ray CT scanner." *Medical physics*, vol. 9, no. 5, Oct. 1982.

[13] Bydder, G. M. and Kreel, L., "The temperature dependence of computed tomography attenuation values," *Journal of computer assisted tomography*, vol. 3, no. 4, Aug. 1979.

[14] Mahnken, A. H. and Bruners, P., "CT thermometry: will it ever become ready for use?" *International journal of clinical practice. Supplement*, no. 171, Apr. 2011.

[15] Jenne, J., Bahner, M., Spoo, J., Huber, P., Rastert, R., Simiantonakis, I., Lorenz, W., and Debus, J., "CT on-line monitoring of HIFU therapy," in *1997 IEEE Ultrasonics Symposium Proceedings. An International Symposium (Cat. No.97CH36118)*, vol. 2, Oct. 1997, pp. 1377–1380 vol.2, iSSN: 1051-0117.

[16] Bruners, P., Levit, E., Penzkofer, T., Isfort, P., Ocklenburg, C., Schmidt, B., Schmitz-Rode, T., Günther, R. W., and Mahnken, A. H., "Multi-slice computed tomography: A tool for non-invasive temperature measurement?" *International journal of hyperthermia : the official journal of European Society for Hyperthermic Oncology, North American Hyperthermia Group*, vol. 26, no. 4, 2010.

[17] Pandeya, G. D., Klaessens, J. H. G. M., Greuter, M. J. W., Schmidt, B., Flohr, T., van Hillegersberg, R., and Oudkerk, M., "Feasibility of computed tomography based thermometry during interstitial laser heating in bovine liver." *European radiology*, vol. 21, no. 8, Aug. 2011.

[18] Pohlan, J., Kress, W., Hermann, K.-G., Mews, J., Kroes, M., Hamm, B., and Diekhoff, T., "Computed Tomography Thermography for Ablation Zone Prediction in Microwave Ablation and Cryoablation: Advantages and Challenges in an Ex Vivo Porcine Liver Model." *Journal of computer assisted tomography*, vol. 44, no. 5, Oct. 2020.

[19] Liu, L. P., Pua, R., Rosario-Berrios, D. N., Sandvold, O. F., Brown, K. M., Gang, G. J., Soulen, M. C., Shapira, N., and Noël, P. B., "Spectral CT thermometry with improved temperature sensitivity for image-guided thermal ablation," in *Medical Imaging 2023: Physics of Medical Imaging*, vol. 12463. SPIE, Apr. 2023, pp. 135–140.

[20] Heinrich, A., Schenkl, S., Buckreus, D., Güttler, F. V., and Teichgräber, U. K.-M., "CT-based thermometry with virtual monoenergetic images by dual-energy of fat, muscle and bone using FBP, iterative and deep learning-based reconstruction." *European radiology*, vol. 32, no. 1, Jan. 2022.

[21] Paul, J., Vogl, T. J., and Chacko, A., "Dual energy computed tomography thermometry during hepatic microwave ablation in an ex-vivo porcine model." *Physica medica : PM : an international journal devoted to the applications of physics to medicine and biology : official journal of the Italian Association of Biomedical Physics (AIFB)*, vol. 31, no. 7, Nov. 2015.

[22] Ruiter, S. J. S., Heerink, W. J., and de Jong, K. P., "Liver microwave ablation: a systematic review of various FDA-approved systems," *European Radiology*, vol. 29, no. 8, Aug. 2019.

[23] Tan, D., Mohamad, N. A., Wong, Y. H., Yeong, C. H., Cheah, P. L., Sulaiman, N., Abdullah, B. J. J., Fabell, M. K., and Lim, K. S., "Experimental assessment on feasibility of computed tomography-based thermometry for radiofrequency ablation on tissue equivalent polyacrylamide phantom." *International journal of hyperthermia : the official journal of European Society for Hyperthermic Oncology, North American Hyperthermia Group*, vol. 36, no. 1, 2019.

[24] Boas, F. E., Fleischmann, D., and others, "CT artifacts: causes and reduction techniques," *Imaging Med*, vol. 4, no. 2, 2012.

[25] Page, M. J., McKenzie, J. E., Bossuyt, P. M., Boutron, I., Hoffmann, T. C., Mulrow, C. D., Shamseer, L., Tetzlaff, J. M., Akl, E. A., Brennan, S. E., Chou, R., Glanville, J., Grimshaw, J. M., Hróbjartsson, A., Lalu, M. M., Li, T., Loder, E. W., Mayo-Wilson, E., McDonald, S., McGuinness, L. A., Stewart, L. A., Thomas, J., Tricco, A. C., Welch, V. A., Whiting, P., and Moher, D., "The PRISMA 2020 statement: an updated guideline for reporting systematic reviews," *BMJ*, vol. 372, Mar. 2021.

[26] Alvarez, R. E. and Macovski, A., "Energy-selective reconstructions in X-ray computerised tomography," *Physics in Medicine & Biology*, vol. 21, no. 5, Sep. 1976.

[27] McCollough, C. H., Leng, S., Yu, L., and Fletcher, J. G., "Dual- and Multi-Energy CT: Principles, Technical Approaches, and Clinical Applications," *Radiology*, vol. 276, no. 3, Sep. 2015.

[28] Homolka, P., Gahleitner, A., and Nowotny, R., "Temperature dependence of HU values for various water equivalent phantom materials," *Physics in Medicine & Biology*, vol. 47, no. 16, Aug. 2002.

[29] Weiss, N., Sosna, J., Goldberg, S. N., and Azhari, H., "Non-invasive temperature monitoring and hyperthermic injury onset detection using X-ray CT during HIFU thermal treatment in ex vivo fatty tissue." *International journal of hyperthermia : the official journal of European Society for Hyperthermic Oncology, North American Hyperthermia Group*, vol. 30, no. 2, Mar. 2014.

[30] Schena, E., Saccomandi, P., Giurazza, F., Caponero, M. A., Mortato, L., Di Matteo, F. M., Panzera, F., Del Vescovo, R., Beomonte Zobel, B., and Silvestri, S., "Experimental assessment of CT-based thermometry during laser ablation of porcine pancreas." *Physics in medicine and biology*, vol. 58, no. 16, Aug. 2013.

[31] Li, K.-W., Fujiwara, D., Haga, A., Liu, H., and Geng, L.-S., "Physical density estimations of single- and dual-energy CT using material-based forward projection algorithm: a simulation study." *The British journal of radiology*, vol. 94, no. 1128, Dec. 2021.

[32] Strigari, L., Minosse, S., D'Alessio, D., Farina, L., Cavagnaro, M., Cassano, B., Pinto, R., Vallati, G., and Lopresto, V., "Microwave thermal ablation using CT-scanner for predicting the variation of ablated region over time: advantages and limitations." *Physics in medicine and biology*, vol. 64, no. 11, May 2019.

[33] Weiss, N., Goldberg, S. N., Sosna, J., and Azhari, H., "Temperature-density hysteresis in X-ray CT during HIFU thermal ablation: heating and cooling phantom study." *International journal of hyperthermia : the official journal of European Society for Hyperthermic Oncology, North American Hyperthermia Group*, vol. 30, no. 1, Feb. 2014.

[34] Decker, J. A., Risch, F., Schwarz, F., Scheurig-Muenkler, C., and Kroencke, T. J., "Improved Thermal Sensitivity Using Virtual Monochromatic Imaging Derived from Photon Counting Detector CT Data Sets: Ex Vivo Results of CT-Guided Cryoablation in Porcine Liver." *Cardiovascular and interventional radiology*, Sep. 2023.

[35] Wang, N., Li, M., and Haverinen, P., "Photon-counting computed tomography thermometry via material decomposition and machine learning." *Visual computing for industry, biomedicine, and art*, vol. 6, no. 1, Jan. 2023.

[36] Hübner, F., Schreiner, R., Panahi, B., and Vogl, T. J., "Evaluation of the

thermal sensitivity of porcine liver in CT-guided cryoablation: an initial study." *Medical physics*, vol. 47, no. 10, Oct. 2020.

[37] Pandeya, G. D., Greuter, M. J. W., Schmidt, B., Flohr, T., and Oudkerk, M., "Assessment of thermal sensitivity of CT during heating of liver: an ex vivo study." *The British journal of radiology*, vol. 85, no. 1017, Sep. 2012.

[38] Bruners, P., Pandeya, G. D., Levit, E., Roesch, E., Penzkofer, T., Isfort, P., Schmidt, B., Greuter, M. J. W., Oudkerk, M., Schmitz-Rode, T., Kuhl, C. K., and Mahnken, A. H., "CT-based temperature monitoring during hepatic RF ablation: feasibility in an animal model." *International journal of hyperthermia : the official journal of European Society for Hyperthermic Oncology, North American Hyperthermia Group*, vol. 28, no. 1, 2012.

[39] Pandeya, G. D., Greuter, M. J. W., de Jong, K. P., Schmidt, B., Flohr, T., and Oudkerk, M., "Feasibility of noninvasive temperature assessment during radiofrequency liver ablation on computed tomography." *Journal of computer assisted tomography*, vol. 35, no. 3, Jun. 2011.

[40] Siddiqui, S. and Khamees, A. A., "Dual-Energy CT-Scanning Applications in Rock Characterization." OnePetro, Sep. 2004.

[41] Liu, L. P., Hung, M., Soulen, M. C., Noël, P. B., and Shapira, N., "Real-time spectral CT thermometry via physical density for image-guided tumor ablation," in *Medical Imaging 2022: Physics of Medical Imaging*, vol. 12031. SPIE, Apr. 2022, pp. 324–330.

[42] Hwang, M., Litt, H. I., Noël, P. B., and Shapira, N., "Accurate physical density assessments from clinical spectral results," in *Medical Imaging 2021: Physics of Medical Imaging*, vol. 11595. SPIE, Feb. 2021, pp. 353–359.

[43] Liu, L. P., Hwang, M., Hung, M., Soulen, M. C., Schaer, T. P., Shapira, N., and Noël, P. B., "Non-invasive mass and temperature quantifications with spectral CT." *Scientific reports*, vol. 13, no. 1, Apr. 2023.

[44] Pichardo, S., Kivinen, J., Melodelima, D., and Curiel, L., "Suitability of a tumour-mimicking material for the evaluation of high-intensity focused ultrasound ablation under magnetic resonance guidance." *Physics in medicine and biology*, vol. 58, no. 7, Apr. 2013.

[45] Varble, N. A., Bakhutashvili, I., Reed, S. L., Delgado, J., Tokoutsi, Z., Frackowiak, B., Baragona, M., Karanian, J. W., Wood, B. J., and Pritchard, W. F., "Morphometric characterization and temporal temperature measurements during hepatic microwave ablation in swine." *PloS one*, vol. 18, no. 8, 2023.

[46] Beisenova, A., Issatayeva, A., Ashikbayeva, Z., Jelbuldina, M., Aitkulov, A., Inglezakis, V., Blanc, W., Saccomandi, P., Molardi, C., and Tosi, D., "Distributed Sensing Network Enabled by High-Scattering MgO-Doped Optical Fibers for 3D Temperature Monitoring of Thermal Ablation in Liver Phantom." *Sensors (Basel, Switzerland)*, vol. 21, no. 3, Jan. 2021.

[47] Schulmann, N., Soltani-Sarvestani, M. A., De Landro, M., Korganbayev, S., Cotin, S., and Saccomandi, P., "Model-Based Thermometry for Laser Ablation Procedure Using Kalman Filters and Sparse Temperature Measurements." *IEEE transactions on bio-medical engineering*, vol. 69, no. 9, Sep. 2022.

[48] Ren, L., Woodrum, D. A., Gorny, K. R., Felmlee, J. P., Favazza, C. P., Thompson, S. M., and Lu, A., "Dual-Applicator MR Imaging-Guided Microwave Ablation with Real-Time MR Thermometry: Phantom and Porcine Tissue Model Experiments." *Journal of vascular and interventional radiology : JVIR*, vol. 34, no. 1, Jan. 2023.

[49] Chen, Y., Ge, M., Jiang, H., Wang, L., and Qiu, B., "An effective method for monitoring tissue temperature using low-field MRI system." *Technology and health care : official journal of the European Society for Engineering and Medicine*, vol. 26, no. 3, 2018.

[50] Zhai, F., Nan, Q., Ding, J., Xu, D., Zhang, H., Liu, Y., and Bai, F., "Comparative experiments on phantom and ex vivo liver tissue in microwave ablation." *Electromagnetic biology and medicine*, vol. 34, no. 1, Mar. 2015.

[51] Hoang, N. H., Murad, H. Y., Ratnayaka, S. H., Chen, C., and Khismatullin, D. B., "Synergistic ablation of liver tissue and liver cancer cells with high-intensity focused ultrasound and ethanol." *Ultrasound in medicine & biology*, vol. 40, no. 8, Aug. 2014.

[52] Schena, E., Saccomandi, P., Giurazza, F., Del Vescovo, R., Mortato, L., Martino, M., Panzera, F., Di Matteo, F. M., Beomonte Zobel, B., and Silvestri, S., "Monitoring of temperature increase and tissue vaporization during laser interstitial thermotherapy of ex vivo swine liver by computed tomography." *Annual International Conference of the IEEE Engineering in Medicine and Biology Society. IEEE Engineering in Medicine and Biology Society. Annual International Conference*, vol. 2013, 2013.

[53] Vogl, T. J., Huebner, F., Naguib, N. N. N., Bauer, R. W., Mack, M. G., Nour-Eldin, N.-E. A., and Meister, D., "MR-based thermometry of laser induced thermotherapy: temperature accuracy and temporal resolution in vitro at 0.2 and 1.5 T magnetic field strengths." *Lasers in surgery and medicine*, vol. 44, no. 3, Mar. 2012.

[54] Chen, C., Liu, Y., Maruvada, S., Myers, M., and Khismatullin, D., "Effect of ethanol injection on cavitation and heating of tissues exposed to high-intensity focused ultrasound." *Physics in medicine and biology*, vol. 57, no. 4, Feb. 2012.

[55] Huang, X.-W., Nie, F., Wa, Z.-C., Hu, H.-T., Huang, Q.-X., Guo, H.-L., Zheng, Q., Xie, X.-Y., Wang, W., and Lu, M.-D., "Thermal Field Distributions of Ablative Experiments Using Cyst-mimicking Phantoms: Comparison of Microwave and Radiofrequency Ablation." *Academic radiology*, vol. 25, no. 5, May 2018.

[56] Liu, Z., Ahmed, M., Weinstein, Y., Yi, M., Mahajan, R. L., and Goldberg, S. N., "Characterization of the RF ablation-induced 'oven effect': the importance of background tissue thermal conductivity on tissue heating." *International journal of hyperthermia : the official journal of European Society for Hyperthermic Oncology, North American Hyperthermia Group*, vol. 22, no. 4, Jun. 2006.

[57] Lobo, S. M., Afzal, K. S., Ahmed, M., Kruskal, J. B., Lenkinski, R. E., and Goldberg, S. N., "Radiofrequency ablation: modeling the enhanced temperature response to adjuvant NaCl pretreatment." *Radiology*, vol. 230, no. 1, Jan. 2004.

[58] Sandison, G. A., Loye, M. P., Rewcastle, J. C., Hahn, L. J., Saliken, J. C., McKinnon, J. G., and Donnelly, B. J., "X-ray CT monitoring of iceball growth and thermal distribution during cryosurgery." *Physics in medicine and biology*, vol. 43, no. 11, Nov. 1998.

[59] Mikhail, A. S., Negussie, A. H., Graham, C., Mathew, M., Wood, B. J., and Partanen, A., "Evaluation of a tissue-mimicking thermochromic phantom for radiofrequency ablation." *Medical physics*, vol. 43, no. 7, Jul. 2016.

[60] Negussie, A. H., Partanen, A., Mikhail, A. S., Xu, S., Abi-Jaoudeh, N., Maruvada, S., and Wood, B. J., "Thermochromic tissue-mimicking phantom for optimisation of thermal tumour ablation." *International journal of hyperthermia : the official journal of European Society for Hyperthermic Oncology, North American Hyperthermia Group*, vol. 32, no. 3, May 2016.

[61] Zhong, X., Zhou, P., Zhao, Y., Liu, W., and Zhang, X., "A novel tissue-mimicking phantom for US/CT/MR-guided tumor puncture and thermal ablation." *International journal of hyperthermia : the official journal of European Society for Hyperthermic Oncology, North American Hyperthermia Group*, vol. 39, no. 1, 2022.

[62] Zhou, Y., Zhao, L., Zhong, X., Ding, J., Zhou, H., Wang, F., and Jing, X., "A thermochromic tissue-mimicking phantom model for verification of ablation plans in thermal ablation." *Annals of translational medicine*, vol. 9, no. 4, Feb. 2021.

[63] Guntur, S. R. and Choi, M. J., "Temperature Dependence of Tissue Thermal Parameters Should Be Considered in the Thermal Lesion Prediction in High-Intensity Focused Ultrasound Surgery." *Ultrasound in medicine & biology*, vol. 46, no. 4, Apr. 2020.

[64] Eranki, A., Mikhail, A. S., Negussie, A. H., Katti, P. S., Wood, B. J., and Partanen, A., "Tissue-mimicking thermochromic phantom for characterization of HIFU devices and applications." *International journal of hyperthermia : the official journal of European Society for Hyperthermic Oncology, North American Hyperthermia Group*, vol. 36, no. 1, 2019.

[65] Choi, M. J., Guntur, S. R., Lee, K. I., Paeng, D. G., and Coleman, A., "A tissue mimicking polyacrylamide hydrogel phantom for visualizing thermal lesions generated by high intensity focused ultrasound." *Ultrasound in medicine & biology*, vol. 39, no. 3, Mar. 2013.

[66] Prakash, P., Converse, M. C., Mahvi, D. M., and Webster, J. G., "Measurement of the specific heat capacity of liver phantom." *Physiological measurement*, vol. 27, no. 10, Oct. 2006.

[67] Morchi, L., Gini, M., Mariani, A., Pagliarani, N., Cafarelli, A., Tognarelli, S., and Menciassi, A., "A Reusable Thermochromic Phantom for Testing High Intensity Focused Ultrasound Technologies." *Annual International Conference of the IEEE Engineering in Medicine and Biology Society. IEEE Engineering in Medicine and Biology Society. Annual In-*

ternational Conference, vol. 2021, Nov. 2021.

[68] Jelbuldina, M., Korganbayev, S., Korobeinyk, A. V., Inglezakis, V. J., and Tosi, D., "Temperature Profiling of ex-vivo Organs during Ferromagnetic Nanoparticles-Enhanced Radiofrequency Ablation by Fiber Bragg Grating Arrays." *Annual International Conference of the IEEE Engineering in Medicine and Biology Society. IEEE Engineering in Medicine and Biology Society. Annual International Conference*, vol. 2018, Jul. 2018.

[69] Dabbagh, A., Abdullah, B. J. J., Ramasindarum, C., and Abu Kasim, N. H., "Tissue-Mimicking Gel Phantoms for Thermal Therapy Studies," *Ultrasonic Imaging*, vol. 36, no. 4, Oct. 2014.

[70] Ahmad, M. S., Suardi, N., Shukri, A., Mohammad, H., Oglat, A. A., Alarab, A., and Makhamrah, O., "Chemical Characteristics, Motivation and Strategies in choice of Materials used as Liver Phantom: A Literature Review." *Journal of medical ultrasound*, vol. 28, no. 1, Mar. 2020.

[71] Stauffer, P. R., Rossetto, F., Prakash, M., Neuman, D. G., and Lee, T., "Phantom and animal tissues for modelling the electrical properties of human liver," *International Journal of Hyperthermia: The Official Journal of European Society for Hyperthermic Oncology, North American Hyperthermia Group*, vol. 19, no. 1, 2003.

[72] Choi, J., Morrissey, M., and Bischof, J. C., "Thermal Processing of Biological Tissue at High Temperatures: Impact of Protein Denaturation and Water Loss on the Thermal Properties of Human and Porcine Liver in the Range 25–80°C," *Journal of Heat Transfer*, vol. 135, no. 061302, May 2013.

[73] Bini, M. G., Ignesti, A., Millanta, L., Olmi, R., Rubino, N., and Vanni, R., "The Polyacrylamide as a Phantom Material for Electromagnetic Hyperthermia Studies," *IEEE Transactions on Biomedical Engineering*, vol. BME-31, no. 3, Mar. 1984.

[74] Bianchi, L., Asadi, S., De Landro, M., Korganbayev, S., and Saccomandi, P., "Measurement of thermal properties of biological tissues and tissue-mimicking phantom with a dual-needle sensor," in *2022 IEEE International Symposium on Medical Measurements and Applications (MeMeA)*, Jun. 2022, pp. 1–6.

[75] Tosi, D., Macchi, E. G., and Cigada, A., "Fiber-Optic Temperature and Pressure Sensors Applied to Radiofrequency Thermal Ablation in Liver Phantom: Methodology and Experimental Measurements," *Journal of Sensors*, vol. 2015, Jan. 2015.

[76] Chen, W. J., Wang, Q., and Kim, C. Y., "Gel Phantom Models for Radiofrequency and Microwave Ablation of the Liver." *Digestive disease interventions*, vol. 4, no. 3, 2020.

[77] Katsura, M., Sato, J., Akahane, M., Kunimatsu, A., and Abe, O., "Current and Novel Techniques for Metal Artifact Reduction at CT: Practical Guide for Radiologists," *RadioGraphics*, vol. 38, no. 2, Mar. 2018.

[78] Do, T. D., Melzig, C., Vollherbst, D. F., Pereira, P. L., Kauczor, H.-U., Kachelrieß, M., and Sommer, C. M., "The value of iterative metal artifact reduction algorithms during antenna positioning for CT-guided microwave ablation." *International journal of hyperthermia : the official journal of European Society for Hyperthermic Oncology, North American Hyperthermia Group*, vol. 36, no. 1, 2019.

[79] Van Hedent, S., Kessner, R., Große Hokamp, N., Baran, T. Z., Kosmas, C., and Gupta, A., "Metal Artifact Reduction in Routine Chest and Abdominal Examinations Using Virtual Monoenergetic Images From Spectral Detector Computed Tomography," *Journal of Computer Assisted Tomography*, vol. 43, no. 5, 2019.

[80] D'Angelo, T., Cicero, G., Mazziotti, S., Ascenti, G., Albrecht, M. H., Martin, S. S., Othman, A. E., Vogl, T. J., and Wichmann, J. L., "Dual energy computed tomography virtual monoenergetic imaging: technique and clinical applications," *The British Journal of Radiology*, vol. 92, no. 1098, Jun. 2019.

[81] Risch, F., Decker, J. A., Popp, D., Sinzinger, A., Braun, F., Bette, S., Jehs, B., Haerting, M., Wollny, C., Scheurig-Muenkler, C., Kroencke, T. J., and Schwarz, F., "Artifact Reduction From Dental Material in Photon-Counting Detector Computed Tomography Data Sets Based on High-keV Monoenergetic Imaging and Iterative Metal Artifact Reduction Reconstructions—Can We Combine the Best of Two Worlds?" *Investigative Radiology*, vol. 58, no. 9, Sep. 2023.

[82] Koetzier, L. R., Mastrodicasa, D., Szczykutowicz, T. P., Werf, N. R. v. d., Wang, A. S., Sandfort, V., Molen, A. J. v. d., Fleischmann, D., and Willemink, M. J., "Deep Learning Image Reconstruction for CT: Technical Principles and Clinical Prospects," *Radiology*, Jan. 2023.

[83] Liang, K., Zhang, L., Yang, H., Yang, Y., Chen, Z., and Xing, Y., "Metal artifact reduction for practical dental computed tomography by improving interpolation-based reconstruction with deep learning." *Medical physics*, vol. 46, no. 12, Dec. 2019.

[84] Wang, T., Xia, W., Huang, Y., Sun, H., Liu, Y., Chen, H., Zhou, J., and Zhang, Y., "DAN-Net: Dual-domain adaptive-scaling non-local network for CT metal artifact reduction." *Physics in medicine and biology*, vol. 66, no. 15, Jul. 2021.

[85] Selles, M., Slotman, D. J., van Osch, J. A. C., Nijholt, I. M., Wellenberg, R. H. H., Maas, M., and Boomsma, M. F., "Is AI the way forward for reducing metal artifacts in CT? Development of a generic deep learning-based method and initial evaluation in patients with sacroiliac joint implants," *European Journal of Radiology*, vol. 163, Jun. 2023.

[86] McWilliams, S. R., Murphy, K. P., Golestaneh, S., O'Regan, K. N., Arellano, R. S., Maher, M. M., and O'Connor, O. J., "Reduction of guide needle streak artifact in CT-guided biopsy," *Journal of vascular and interventional radiology: JVIR*, vol. 25, no. 12, Dec. 2014.

[87] Do, T. D., Haas, A., Vollherbst, D. F., Pan, F., Melzig, C., Jesser, J., Pereira, P. L., Kauczor, H. U., Skornitzke, S., and Sommer, C. M., "Semi-automatic artifact quantification in thermal ablation probe and algorithms for the evaluation of metal artifact reduction." *International journal of hyperthermia : the official journal of European Society for Hyperthermic Oncology, North American Hyperthermia Group*, vol. 40, no. 1, 2023.

[88] Do, T. D., Heim, J., Melzig, C., Vollherbst, D. F., Kauczor, H. U., Skornitzke, S., and Sommer, C. M., "Virtual monochromatic spectral imaging versus linearly blended dual-energy and single-energy imaging during CT-guided biopsy needle positioning: Optimization of keV settings and impact on image quality." *PloS one*, vol. 15, no. 2, 2020.

[89] Do, T. D., Sommer, C. M., Melzig, C., Nattenmüller, J., Vollherbst, D., Kauczor, H.-U., Stiller, W., and Skornitzke, S., "A Novel Method for Segmentation-Based Semiautomatic Quantitative Evaluation of Metal Artifact Reduction Algorithms." *Investigative radiology*, vol. 54, no. 6, Jun. 2019.

[90] Do, T. D., Heim, J., Skornitzke, S., Melzig, C., Vollherbst, D. F., Faerber, M., Pereira, P. L., Kauczor, H.-U., and Sommer, C. M., "Single-energy versus dual-energy imaging during CT-guided biopsy using dedicated metal artifact reduction algorithm in an in vivo pig model." *PloS one*, vol. 16, no. 4, 2021.

[91] Wang, G., Wang, Z., and Jin, Z., "A Novel Metallic Artifact Reduction Technique When Using a Computed Tomography-Guided Percutaneous Metallic Antenna to Ablate Malignant Pulmonary Nodules: A Qualitative and Quantitative Assessment." *Medical science monitor : international medical journal of experimental and clinical research*, vol. 26, Jun. 2020.

[92] Shapira, N., Liu, L. P., Pua, R., Rosario, D., Kim, J., Cormode, D. P., Nadolski, G. J., Hung, M., Soulen, M. C., and Noël, P. B., "Non-invasive real-time thermometry via spectral CT physical density quantifications," in *7th International Conference on Image Formation in X-Ray Computed Tomography*, vol. 12304. SPIE, Oct. 2022, pp. 14–21.

[93] Kostyrko, B., Rubarth, K., Althoff, C., Zibell, M., Neizert, C. A., Poch, F., Torsello, G. F., Gebauer, B., Lehmann, K., Niehues, S. M., Mews, J., Diekhoff, T., and Pohlan, J., "Evaluation of Different Registration Algorithms to Reduce Motion Artifacts in CT-Thermography (CTT)." *Diagnostics (Basel, Switzerland)*, vol. 13, no. 12, Jun. 2023.

[94] Zhou, Y., Zhao, Y., Li, B., Xu, D., Yin, Z., Xie, F., and Yang, J., "Meta-analysis of radiofrequency ablation versus hepatic resection for small hepatocellular carcinoma," *BMC Gastroenterology*, vol. 10, no. 1, Jul. 2010.

[95] Lewis, M. A., Staruch, R. M., and Chopra, R., "Thermometry and Ablation Monitoring with Ultrasound," *International journal of hyperthermia : the official journal of European Society for Hyperthermic Oncology, North American Hyperthermia Group*, vol. 31, no. 2, Mar. 2015.

[96] Rieke, V. and Butts Pauly, K., "MR thermometry," *Journal of Magnetic Resonance Imaging*, vol. 27, no. 2, 2008.

[97] Willemink, M. J., Persson, M., Pourmorteza, A., Pelc, N. J., and Fleischmann, D., "Photon-counting CT: Technical Principles and Clinical Prospects," *Radiology*, vol. 289, no. 2, Nov. 2018.

[98] Choy, G., Khalilzadeh, O., Michalski, M., Do, S., Samir, A. E., Pianykh, O. S., Geis, J. R., Pandharipande, P. V., Brink, J. A., and Dreyer, K. J., "Current Applications and Future Impact of Machine Learning in Radiology," *Radiology*, vol. 288, no. 2, Aug. 2018.

Appendix A. Full search strings

Search strings used in PubMed to find results for (I) CT thermometry methods, (II) experimental setup for CT thermometry, and (III) needle artifact reduction methods.

I (((”Tomography, X-Ray Computed”[majr] OR ”computer tomographic”[ti] OR ”computed tomographic”[ti] OR ”computed tomography”[ti] OR ”computer tomography”[ti] OR ”computer assisted tomographic”[ti] OR ”computed assisted tomography”[ti] OR ”computer assisted tomography”[ti] OR ”CT”[ti]) AND (”thermography”[ti] OR ”thermometry”[ti] OR ”Thermometry”[majr] OR ”Thermography”[majr] OR ((”thermal”[ti] OR ”temperature”[ti] OR ”temperature”[majr]) AND (”map”[ti] OR ”sensitivity”[ti] OR ”monitoring”[ti] OR ”assess*”[ti] OR ”measu*”[ti])) OR ”physical density”[tw] OR ”physical density”[title/abstract: 3])) OR ((”Tomography, X-Ray Computed”[mesh] OR ”computer tomographic”[tw] OR ”computed tomographic”[tw] OR ”computed tomography”[tw] OR ”computer tomography”[tw] OR ”computer assisted tomographic”[tw] OR ”computed assisted tomography”[tw] OR ”computer assisted tomography”[tw]) AND (”map temperature”[title/abstract: 3] OR ”mapped temperature”[title/abstract: 3] OR ”mapping temperature”[title/abstract: 3] OR ”sensitivity temperature”[title/abstract: 3] OR ”monitoring temperature”[title/abstract: 3] OR ”monitor temperature”[title/abstract: 3] OR ”monitored temperature”[title/abstract: 3] OR ”assessment temperature”[title/abstract: 3] OR ”assessed temperature”[title/abstract: 3] OR ”assessing temperature”[title/abstract: 3] OR ”assessments temperature”[title/abstract: 3] OR ”measurement temperature”[title/abstract: 3] OR ”measurements temperature”[title/abstract: 3] OR ”measured temperature”[title/abstract: 3] OR ”measuring temperature”[title/abstract: 3] OR ”map thermal”[title/abstract: 3] OR ”mapped thermal”[title/abstract: 3] OR ”mapping thermal”[title/abstract: 3] OR ”sensitivity thermal”[title/abstract: 3] OR ”monitoring thermal”[title/abstract: 3] OR ”monitor thermal”[title/abstract: 3] OR ”monitored thermal”[title/abstract: 3] OR ”assessment thermal”[title/abstract: 3] OR ”assessed thermal”[title/abstract: 3] OR ”assessing thermal”[title/abstract: 3] OR ”assessments thermal”[title/abstract: 3] OR ”measurement thermal”[title/abstract: 3] OR ”measurements thermal”[title/abstract: 3] OR ”measured thermal”[title/abstract: 3] OR ”measuring thermal”[title/abstract: 3])))

II (((”Radiofrequency Ablation”[Mesh] OR ”Ablation Techniques”[Mesh] OR ”ablat*”[tiab]) AND (”thermal”[tiab] OR ”therm*”[tiab]) AND (”Phantoms, Imaging”[Mesh] OR ”tissue-mimicking”[tiab] OR ”phantom”[tiab] OR ”phantom*”[tiab] OR ”thermochromic”[tiab]) AND (”Liver”[Mesh] OR ”liver”[tiab] OR ”hepat*”[tiab])) OR ((”Radiofrequency Ablation”[majr] OR ”Ablation Techniques”[majr] OR ”ablat*”[ti]) AND (”thermal”[ti] OR ”therm*”[ti]) AND (”Phantoms, Imaging”[majr] OR ”tissue-mimicking”[ti] OR ”phantom”[ti] OR ”phantom*”[ti] OR ”thermochromic”[ti])))

III (((”Needle Artifact”[tw] OR ”Needle Artifact”[tw] OR ”Needle Artifact”[title/abstract: 3] OR ”Needle Artifact”[title/abstract: 3] OR ((”Needles”[Mesh] OR ”Biopsy, Needle”[Mesh]) AND ”Artifacts”[Mesh])) AND (”Tomography, X-Ray Computed”[mesh] OR ”computer tomographic”[tw] OR ”computed tomographic”[tw] OR ”computed tomography”[tw] OR ”computer tomography”[tw] OR ”computer assisted tomographic”[tw] OR ”computed assisted tomography”[tw] OR ”computer assisted tomography”[tw])) OR ((”Metal Artifact”[tw] OR ”Metal Artifact”[tw] OR ”Metal Artifact”[title/abstract: 3] OR ”Metal Artifact”[title/abstract: 3] OR ”Metals Artifact”[title/abstract: 3] OR ”Metals Artifact”[title/abstract: 3]) AND (”Tomography, X-Ray Computed”[majr] OR ”computer tomographic”[ti] OR ”computed tomographic”[ti] OR ”computed tomography”[ti] OR ”computer tomography”[ti] OR ”computer assisted tomographic”[ti] OR ”computed assisted tomography”[ti] OR ”computer assisted tomography”[ti] OR ”CT”[ti])))